Validation of Surface Elevation from TanDEM-X Digital Elevation Models of Devon Island Ice Cap, Canadian High Arctic

Claire Bernard-Grand'Maison

A thesis submitted in partial fulfillment of the requirements for the
Master of Science degree in Physical Geography

Department of Geography, Environment and Geomatics
Faculty of Arts
University of Ottawa

Supervisors
Dr. Luke Copland
Dr. David Burgess

Thesis Committee
Dr. Laurence Gray
Dr. Anders Knudby

Table of Contents

List of Tables

Chapter 5: Discussion and Conclusion

Appendix

List of Figures

Chapter 4: Results

Acknowledgements

I would first like to express my sincere appreciation to both my supervisors: Dr. Luke Copland (University of Ottawa) and Dr. David Burgess (Natural Resources Canada) for their support and guidance throughout this project. To Luke, you have been for me and will continue to be an outstanding mentor. I am very grateful for all the opportunities you have provided me to get immersed in the world of glaciology and academia. To Dave, thank you for welcoming me in your field program and for your generosity in sharing your knowledge of Devon Ice Cap and of the Arctic. These two years have been an unforgettable experience and I am very grateful for all the valuable lessons I have learned from you both.

I would like to acknowledge my thesis committee Drs. Anders Knudby and Laurence Gray for providing helpful feedback. I thank particularly Dr. Gray for his advice and comments regarding the analysis of synthetic aperture radar data on snow and ice.

I am very thankful to the DLR German Remote Sensing Data Center team, especially to Dr. Birgit Wessel, Achim Roth and Dr. Sahra Abdullahi, for welcoming me twice in Oberpfaffenhofen, for providing crucial support to access and analyze TerraSAR-X/TanDEM-X data and for their constructive comments on my work. I extend my appreciation to others who have provided data and technical support for this project: Dr. Anja Rutishauser and colleagues at the University of Texas Geophysics Institute for providing access to the processed SEARCH data; and Drs. Robert McNabb and Christopher Nuth for assistance with the co-registration code during my visit at the Department of Geosciences at the University of Oslo.

A warm thank you to Dr. Ashley Dubnick (Alpine and Arctic Research Group, University of Alberta) and Dr. Brad Danielson for sharing their love of the field and expertise with me. You have contributed to the many great memories I have from two spring field seasons on the ice cap. A special thank you to Jimmy Qaapik for his inspiring stories and Inuktut lessons, and for sharing his contagious affection for the land surrounding Grise Fiord.

I am also very grateful for the friendships I have found within the Laboratory for Cryospheric Research. I thank my fellow members for their support and advice, and for the countless laughter's which enlightened my journey.

The completion of this project would not have been possible without the love and support from family and close friends. To Louise, thank you for always making me believe in my capacities and for your wise words whenever times where challenging. To Sylvain and Monique, thank you for your genuine interest in my project, your constant words of encouragement and for sharing your fascination of the North with me. To Odin, I am forever grateful for your moral support and kindness which helped me to keep my head up until the defence. *Merci!*

Finally, I would like to acknowledge the generous support from the following organizations and agencies: the Association of Canadian Universities for Northern Studies; the W. Garfield Weston Foundation; the Natural Sciences and Engineering Research Council of Canada Canadian Graduate Scholarship; the *Fonds de recherche du Québec Nature et technologies* Graduate Scholarship; the Remote-Ex Norwegian/Canadian/American Partnership Program; the University Centre in Svalbard; the Department of Geosciences (University of Oslo); ArcticNet; the Polar Continental Shelf Program; the Northern Scientific Training Program; the Geological Survey of Canada (Natural Resources Canada); Climate Change Geoscience Program Land and Minerals Sector (Natural Resources Canada); Canada Foundation for Innovation; the Hamlet of Grise Fiord; the Ontario Research Fund; the Natural Sciences and Engineering Research Council of Canada Discovery Grant and Northern Supplement; the Faculty of Graduate and Post-Doctoral Studies (University of Ottawa); the Department of Geography, Environment and Geomatics (University of Ottawa); and the University of Ottawa.

Legend

AAR	Accumulation Area Ratio
AMP	Amplitude
ATM	Airborne Topographic Mapper
AWS	Automatic Weather Station
CAA	Canadian Arctic Archipelago
CDEM	Canadian Digital Elevation Model
COH	Coherence
DEM	Digital Elevation Model
dGPS	Differential Global Positioning System
DIC	Devon Island Ice Cap
DLR	German Aerospace Center
DN	Digital Number
EEC	Enhanced Ellipsoid Corrected
ELA	Equilibrium Line Altitude
ENL	Equivalent Number of Looks
GCP	Ground Control Point
GIM	Geocoded Incidence Map
GPR	Ground Penetrating Radar
GPS	Global Positioning System
GSC	Geological Survey of Canada
HEM	Height Error Map
HoA	Height of Ambiguity
InSAR	Interferometric Synthetic Aperture Radar
ITP	Integrated TanDEM-X Processor
LIA	Little Ice Age
LST	Land Surface Temperature
MCP	Mosaicking and Calibration Processor
MODIS	Moderate Resolution Imaging Spectroradiometer
NOW	North Open Water Polynya
PPP	Precise Point Positioning Service
QEI	Queen Elizabeth Islands
RMSE	Root Mean Square Error
RR	Radiometric Resolution
SAR	Synthetic Aperture Radar
SEARCH	Subglacial Extraterrestrial Analogue Research in the Canadian High Arctic
SMB	Surface Mass Balance
SRTM	Shuttle Radar Topography Mission
SWE	Snow Water Equivalent
UTIG	University of Texas Institute of Geophysics

Abstract

Digital elevation models (DEMs) generated by the TanDEM-X mission from synthetic aperture radar interferometry (InSAR) provide an excellent potential resource to study the geodetic mass balance of glaciers. However, they typically suffer from a negative bias in surface elevations on glacierized terrain due to penetration of radar waves into the snowpack and firn. In this thesis, TanDEM-X DEMs from 2010 to 2018 over Devon Island Ice Cap (DIC), Canadian High Arctic, are validated using independent surface elevation datasets from ArcticDEM, IceBridge laser altimetry and ground GPS transects. In agreement with previous studies using TanDEM-X DEMs, the bias is most significant in the percolation and saturation zones (i.e., accumulation area), where volume scattering and loss of interferometric coherence is greatest compared to the bare ice zone. The average elevation bias on DIC is -2.74 ±0.25 m, which should be accounted for in error budgets for geodetic mass balance estimates to be reliable.

Chapter 1: Introduction

Climate warming, associated with increases in anthropogenic greenhouse gases, is currently greatest at high latitudes due to the polar amplification feedback (AMAP, 2017). Responding to this warming, Arctic land ice has been losing mass at an increasing rate, contributing 0.10 m to global sea level rise over the period 1850-2010 (AMAP, 2017). In the long-term (centuries to millennia), mass loss from the ice sheets is predicted to have the greatest impact on sea level, but on a shorter time scale (decades to centuries) melting glaciers and ice caps will provide the largest contributions to sea level rise (Stocker et al., 2013). Since 1990, glaciers and ice caps have lost more mass than both Greenland and Antarctica combined (Stocker et al., 2013), and over the past two decades the Canadian Arctic has emerged as the second region outside the Greenland Ice Sheet in the Arctic with a significant contribution to eustatic sea level rise, just behind Alaska (Box et al., 2018).

Sea level rise projections depend on an accurate assessment of land ice mass changes and require continuous long-term records (Wouters et al., 2013). A major uncertainty in these projections is how glacier dynamics are changing under a warming climate, and whether glaciers are speeding up (resulting in enhanced thinning) or slowing down (resulting in reduced thinning or even thickening) (Abdalati et al., 2004; AMAP, 2017). Traditionally, regional estimates of ice mass change have been based on local glaciological (in-situ) mass balance measurements, not taking into account dynamic processes. Such measurements are field intensive and only a few long-term mass balance series are available for the Canadian Arctic, notably collected by the Geological Survey of Canada Mass Balance Program (Burgess, 2017). The representativeness of thickness change derived from these in-situ measurements over broad spatial scales can have significant uncertainties and lead to biases in estimating contributions to sea level rise (Gardner et al., 2013). Nevertheless, they have been instrumental for providing first order estimates at the synoptic scale before reliable satellite records became available (Cogley & Adams, 1998; Dowdeswell et al., 1997). In-situ measurements are a robust indicator of climate change and more recently have been successfully used to calibrate and validate remote sensing observations (e.g., Gray et al., 2015; Box et al., 2018) and glacier mass balance models (e.g., Huss & Hock, 2015). However, geodetic mass balance measurements can better account for the effects of changing glacier motion by capturing thickness change of whole glacier systems (Zemp et al., 2013). Glacier

change studies using this method have helped to constrain global glacier losses and their contribution to sea level in previously unstudied remote areas (e.g., Cogley, 2009).

The geodetic mass balance method consists of calculating changes in volume of glaciers and ice caps and converting them to water equivalent changes in mass using the density of the removed material, i.e., firn or ice (Benn and Evans, 2010).Volume changes over a defined time period can be obtained from differencing remotely sensed elevation datasets over a specific area. Two types of remotely sensed elevation datasets are used to study glacier elevation change and calculate geodetic mass balance: (1) surface elevation point data obtained from laser or radar altimetry sensors on satellite and airborne platforms, and (2) digital elevation models (DEMs), referring to continuous surface elevation datasets created from pairs of satellite images, air photos or from the extrapolation of point elevation datasets over a specific area.

The two most widely used point satellite altimetry datasets for thickness changes and geodetic mass balance studies are ICESat (laser altimetry, NASA, 2003-2009) and Cryosat-2 (radar altimetry, ESA, 2010-present). Both these satellites were developed with the specific purpose of studying changes in the cryosphere, with a focus on the Polar Regions. For example, ICESat data has been used to study glacier thickness changes in Svalbard (Moholdt et al., 2010). Cryosat-2 data has been used to produce maps of thickness changes at sub-kilometer scale enabling the calculation of geodetic mass balance for the Icelandic ice caps (Foresta et al., 2016) and for the Patagonian icefields (Foresta et al., 2018), and to derive monthly surface elevation changes from Canadian Arctic ice caps (Gray et al., 2015). Recent DEMs used for elevation change calculations can be created from pairs of optical satellite images processed with stereoscopic matching (e.g., from ASTER, SPOT5, Worldview and Sentinel-2 satellites), and synthetic aperture radar (SAR) images processed with interferometry (e.g., Shuttle Radar Topography Mission (SRTM), C- and X-band SAR flown in 2000 (Rabus et al., 2003)). The choice of a remotely sensed elevation product for elevation change calculation depends on a combination of resolution and coverage both temporally and spatially. Point datasets have a much sparser coverage than DEMs and are therefore used more often in large scale studies (e.g., Gardner et al., 2013; Bolch et al., 2013). DEMs offer continuous coverage and are favoured to calculate geodetic mass balance estimates over smaller regions (e.g., Berthier et al, 2010; Brun et al., 2017).

Developed from a collaboration between the German Aerospace Center (DLR) and Airbus Defense and Space, the TanDEM-X satellite mission is the first bi-static SAR system in space, offering the possibility of creating DEMs of unprecedented accuracy since 2010. The satellite constellation contains two quasi-identical satellites TerraSAR-X and TanDEM-X flying in close orbit at an altitude of approximately 500 km, both operating a SAR instrument at X-band (Rizzoli et al., 2017a). Their configuration permits the creation of accurate interferograms which have been processed to create a global DEM at 12 m resolution. Radar sensors have a great advantage over optical sensors for the study of the Polar Regions as they can generate data independently of solar illumination or cloud cover. With the potential of high temporal resolution and increased spatial resolution, TanDEM-X DEMs are a very promising resource for glaciological applications. However, for the calculation of elevation change and geodetic mass balance, this sensor type has a specific bias on glacierized terrain: an elevation bias due to the penetration of the radar signal into snow and ice. It has been shown that radar signal penetrates the subsurface and creates an elevation bias up to 10 meters in cold and dry snow and firn of the Greenland Ice Sheet (e.g., Rignot et al., 2001; Wessel et al., 2016). This elevation bias depends on surface and subsurface properties which can be highly variable in time and space on glacierized terrain depending on the occurrence of melt and evolution of snow facies.

Previous studies using TanDEM-X DEMs and SRTM DEMs have acknowledged this bias and many have provided estimates by comparing the DEMs with higher accuracy elevation datasets (e.g., Gardelle et al., 2012a; Groh et al., 2014). However, very few studies have quantified the impact of this bias in their measurements of elevation change and geodetic mass balance. Although multiple studies and convincing arguments have been put forward to assume that it is not significant (e.g., Rankl & Braun, 2016), there is still a need to assess the magnitude of this elevation bias in order to calculate accurate elevation change on glacierized terrain from TanDEM-X DEMs (Dehecq et al., 2016). This is especially true for locations where field measurements are very sparse, where rates of surface elevation change are small and where firn dominates the subsurface, such as on large ice caps in the Canadian Arctic.

A model is currently being developed at the German Remote Sensing Data Center (DLR) to incorporate a correction for elevation bias due to penetration in their TanDEM-X DEM products over all snow- and ice-covered regions solely based on SAR scene information. Validation of TanDEM-X DEM products with higher accuracy elevation datasets has been undertaken on the

Greenland Ice Sheet for the first stage of model development by Abdullahi et al. (2018). To develop a model applicable to other regions and on different terrain conditions, this thesis expands validation to a smaller ice cap in the Canadian Arctic, Devon Island Ice Cap (DIC). With yearly fieldwork expeditions starting in the 1960s, DIC is one of the most intensively studied large ice mass in the circumpolar Arctic (Boon et al., 2010) and there exists a large number of baseline datasets to complement the validation of TanDEM-X surface elevation.

1.1 Thesis Objectives

The aim of this thesis is to use data from DIC to validate surface elevations of TanDEM-X DEMs. There are three specific components to this validation:

(1) quantify the elevation bias in TanDEM-X DEMs over DIC by calculating elevation differences with other independent elevation datasets of known accuracy;
(2) assess the spatial and temporal variability in elevation bias and relate it to near surface density conditions, notably to glacier facies;
(3) investigate the relationship between elevation differences and SAR parameters that have been proposed to model the elevation bias.

Our study period spans five *frozen seasons*, referring to periods from November to May inclusively, from November 2010 - May 2011 (frozen season 2010-11) to November 2017- May 2018 (frozen season 2017-18). We use the term frozen season to refer to a period when the vast majority of the ice cap rarely experiences melt. By including numerous validation elevation datasets and relating our observations to published literature, the validation of surface elevation of the TanDEM-X DEMs on DIC presented in this thesis provides a comprehensive assessment of their accuracy for calculation of thickness change and geodetic mass balance on glacierized terrain outside of the ice sheets.

1.2 Thesis Format

This thesis follows a traditional format. This Introduction is followed by a Background in Chapter 2 that provides a brief overview of SAR and interferometry, of the interaction of SAR signals with snow and ice (specifically with different glacier facies), of previous studies using

TanDEM-X DEMs for glaciological applications and elevation change, and an overview of current knowledge of DIC. Datasets and Methodology used to undertake this study are presented in Chapter 3. Results are described in Chapter 4, and Chapter 5 presents a Discussion and Conclusion. To conform with the scientific writing style this thesis is written in the first-person using the plural forms “we” and “our”, even though the work was performed primarily by the sole author.

Chapter 2: Background

2.1 Synthetic Aperture Radar and Interferometry

A Synthetic Aperture Radar is an imaging radar mounted on a moving platform, most commonly on a satellite (spaceborne SAR). It is an active imaging sensor technology, where microwave electromagnetic pulses are sent through an antenna in the direction of the ground surface (Fig. 2.1a). The pulses interact with the ground surface and only a portion of the signal is backscattered towards the receiving antenna and recorded. The combination of received backscattered signal as the platform moves allows the construction of a scene with a much larger aperture than the antenna length, hence the origin of its name "synthetic aperture" (Moreira et al., 2013). The received raw echo signals, forming a complex image, contain information about the amplitude and the phase which depends on physical and electrical properties of the different surface scatterers. The frequency of the emitted pulse of the sensor affects its interaction with the ground surface, with longer electromagnetic wavelengths penetrating deeper into the subsurface and interacting more with subsurface scatterers. The TanDEM-X satellite operates at a relatively high-frequency in the X-band at 9.56 GHz (wavelength of ~ 3.1 cm) (Fritz & Eineder, 2013). After processing of the raw echo signal, a radar image can be formed where each pixel indicates the intensity of the backscattered signal. The images are then calibrated for pixels to represent the backscatter intensity in the ground range (in sigma zero, σ_0) and geocoded, i.e., projected from the slant to the ground range (Fig. 2.1a). Due to the side-looking nature of most SAR systems, distortions can occur in the final scene as stretch and compression on sloped terrain (foreshortening and layover), and shadows from areas hidden from the radar pulses. Multiple imaging modes are possible with current SAR satellite systems, producing larger swath images than in its simplest continuous strip acquisition (Stripmap mode). The antenna can be steered at different elevations and its radiation pattern altered to produce images of larger swath (ScanSAR modes) at the expense of azimuth resolution, or at smaller swath (Spotlight modes) with highest azimuth resolution (Moreira et al., 2013).

DEMs can be created from SAR scenes using the process of interferometry. The basic idea behind SAR interferometry (InSAR) is to compare the phase of two complex radar images acquired from a slightly different angle or from a different time (Moreira et al., 2013). When

complex radar images are acquired from the same flight track, the interferometric processing is referred to as *across-track interferometry* which allows the measurement of surface topography (e.g., glacier surface elevation). When complex radar images are acquired in the same geometry but at different times, the interferometric processing is referred to as *along-track interferometry* or *differential interferometry*, from which surface displacement can be measured (e.g., glacier surface velocity). As seen in Figure 2.1b, in across-track interferometry the antenna displacement (by the length of the perpendicular baseline), causes a difference in range in the backscatter of each pixel that can be evaluated to surface height. An *interferogram* is produced from the difference in phase of two complex SAR images. The accuracy of the interferogram, and of the later derived surface height, is expressed by the *coherence*. This measure of correlation represents the degree of similarity between the two complex images. When a pair of complex radar images are coherent, the phase difference is mostly dependant on the difference in range and the surface height can be determined more accurately (Hanssen, 2001). Loss of coherence, termed *decorrelation*, is affected by the signal to noise ratios of the complex images and other factors such as temporal differences, baseline length, volume scattering and atmospheric interactions. In the case of the TanDEM-X constellation, the TerraSAR-X and TanDEM-X satellites are in a bi-static configuration whereby one satellite transmits radar pulses and both satellites record the backscattered signal. The satellites act as a single-pass SAR interferometer, where two radar scenes are acquired quasi-simultaneously (Rizzoli et al., 2017a). This configuration allows no loss of coherence due to temporal and atmospheric decorrelation.

The conversion of the phase to height value from the interferogram is undertaken by a process called *phase unwrapping*. This process converts the interferogram values, which are ambiguous by integer multiples of 2π, using the height of ambiguity (HoA) to "unwrap" the values to the continuous phase. The HoA corresponds to the height difference that causes an interferometric phase change of 2π. For the TanDEM-X configuration, the HoA is defined as:

$$HoA = \frac{\lambda \cdot r \cdot \sin(\theta_i)}{B_\perp} \tag{2.1}$$

where λ is the wavelength of the transmitted signal, r is the slant range distance, θ_i is the incidence angle and $B_\perp$ is the perpendicular baseline of the line of sight (Rizzoli et al., 2017a). The remaining uncertainty in the unwrapped phase is solved using radargrammetric techniques to obtain absolute

height values in the case of TanDEM-X (Rizzoli et al., 2017a). The position of each pixel relative to the sensor can then be determined by trigonometry from the interferometric range and imaging geometry (Fig 2.1b). In the last step, the data is transformed from the radar geometry to coordinates of a reference geodetic system producing a geocoded DEM, where each pixel is generally in units of meters above sea level (Moreira et al., 2013).

2.2 Scattering Mechanisms in Snow and Ice

To understand how an elevation bias is produced in InSAR DEMs on glacierized terrain, including in TanDEM-X DEMs, we first briefly review the scattering mechanisms of radar signal in snow and ice and the general backscatter properties of different glacier facies.

The intensity recorded from each pixel in a radar image is an integration of multiple scattering signals from its interaction with the ground surface. Two main scattering mechanisms can be defined: surface and volume scattering (Fig. 2.2). Surface scattering occurs at the boundary between air and snow or ice, and represents diffuse scattering in all directions including in the specular direction (forward scatter) (Fig. 2.2a). It is proportional to the amplitude of the radar signal, influenced by the local incidence angle, which is affected by surface roughness (Snehmani et al, 2015).

Volume scattering occurs within the subsurface at the boundary between different and inhomogeneous media as the radar signal penetrates the snowpack (Fig. 2.2b). Penetration depth of the radar signal depends on the wavelength, incidence angle, and by scattering and absorption losses in a medium (Zhao and Floricioiu, 2017). If the structures in a medium are of much smaller size than the wavelength, the radar signal can penetrate the medium without any backscattering reflection occurring (Tsai et al., 2019). Volume scattering is proportional to transmissivity, the fraction of the signal transmitted by the surface, which is affected by the dielectric properties of the medium (Snehmani et al., 2015).

The snowpack (and the glacier surface) can be considered as an inhomogeneous mixture of ice, water and air, which all have different dielectric properties. In dry snow, volume scattering occurs at the discontinuities of dielectric properties of the medium, between air and ice (as snow grains or larger features). In this case, backscatter is the sum of volume scattering and surface scattering and is independent from surface roughness (Tsai et al., 2019). As absorption of the

transmitted signal is low, radar waves are able to penetrate deeper. In wet snow, the presence of liquid water increases absorption and reduces volume scattering and penetration depth. For wetness ≥3% volume, surface scattering becomes dominant and is controlled by surface roughness (Snehmani et al., 2015). As the proportion of ice, air and water changes in the snowpack, the cumulative dielectric properties of the medium changes, impacting the dominant scattering mechanisms and the backscatter intensity (Tsai et al., 2019). At the pixel scale of a radar image, the summation of scattering information occurring within a pixel can lead to high or low backscatter as constructive and destructive interference occurs. This is translated as speckle in the data and increases the complexity of interpreting SAR images (Tsai et al., 2019).

In practical terms, backscatter intensity of a snowpack as seen in a radar image for a specific wavelength is affected by temperature, grain size, density, depth, stratigraphy, surface roughness and presence of liquid water (Tsai et al., 2019). The interplay of these parameters is quite complex, and their evolution is environment specific. Therefore, studies reporting modelled and measured backscattering properties of snow generally focus on a certain radar band or satellite and environment (e.g., snow on sea ice, snow in forested areas, snow on glaciers).

2.2.1 General Backscatter Patterns in Glacier Facies

The sensitivity of microwaves to the physical properties of the surface and subsurface explains the success of using radar technologies to study evolution of glacier *facies* (e.g., Partington et al., 1998; Nolin & Payne, 2007; König et al., 2002; Hall et al., 2000; Rizzoli et al., 2017b). Five different glacier *facies* or *zones* can typically be discriminated on a glacier surface depending on the main processes of accumulation, snow metamorphism and ablation (Fig. 2.3) (Benn & Evans, 2010). Below we describe the main facies zones and their general backscatter properties as seen in SAR data mainly during the winter season, as this is when most of the TanDEM-X data we used was acquired.

As its name indicates, no melt occurs in the *dry snow zone* which is located at the highest elevations of glacierized terrain where yearly snow accumulation is compacted under its own weight, is metamorphosed by wind action, and depth hoar development occurs (Partington, 1998). Low backscatter dominates in this region due to the penetration of the radar wave in a low-density snowpack with relatively small grain size and lack of internal scatterers (Rizzoli et al., 2017b; Casey & Kelly, 2010).

Below the dry snow zone is the *percolation zone* where a minimal amount of melt occurs during the summer. During the melt season, water percolates through the snowpack and refreezes at depth in the form of ice lenses, layers, and pipes (Partington, 1998). During the winter, this zone is characterized by a much stronger backscatter signal than the dry snow zone due to larger grain size and presence of melt features acting as scatterers in the subsurface (Casey & Kelly, 2010). The size of melt features can be comparable to the radar wavelength, increasing the number of scatterers in the subsurface and volume scattering (Partington, 1998).

Lower in elevation is the *wet snow zone* or *saturation zone,* where an increasing amount of melt occurs. The meltwater percolates the full thickness of the snowpack in this region, increasing the number and thickness of melt features (Benn and Evans, 2010). In this zone, the snowpack reaches the melting point during the summer due to latent heat released by the refreezing of meltwater, increasing grain size (Partington, 1998). During the winter season, this zone is hardly distinguishable from the percolation zone in SAR imagery as the scattering mechanisms are similar (Rizzoli et al., 2017b; Casey & Kelly, 2010). Previous work on the Greenland Ice Sheet suggests that higher variability in backscatter is expected in this zone compared to the percolation zone due to presence of slush or melt ponds and larger melt features (Jezek, 1994; Partington et al., 1998).

During the melt season, refreezing of meltwater at the base of the snowpack creates the *superimposed ice zone*, which is exposed below the snow or firn line (Ben and Evans, 2010). Firn can be defined as densified snow which has survived at least one melt season (Nolin & Payne, 2007). The superimposed ice zone might not be present every year on a glacier depending on the intensity of melt (Partington, 1998). It is generally difficult to distinguish from the lower bare ice zone in SAR data due to their similarities, but the backscatter signal should be lower than the saturation zone and higher than the bare ice zone (Casey and Kelly, 2010). The few studies which have detected this zone in SAR imagery have relied on its different surface roughness and air bubble content compared to bare glacier ice (Nolin & Payne, 2007).

The equilibrium line is located below the superimposed ice zone and separates the accumulation area above from the ablation area below, which is referred to as the *bare ice zone* (Fig. 2.3). In this zone, the total accumulation from the winter snowpack, surface refreezing and more can be lost to melting (Partington, 1998). The glacier surface is generally much rougher in this zone due to the presence of crevasses, meltwater channels, moraines and debris. A dry bare

ice surface can have a relatively strong backscatter signal due to its roughness, but during the frozen season the presence of a deep and dry snowpack will attenuate this signal (Partington, 1998) (Fig. 2.2c).

2.3 Occurrence of an Elevation Bias in InSAR Surface Elevations on Glacierized Terrain and Relationship to Interferometric Coherence

Background knowledge of scattering mechanisms in snow and ice, and how this is reflected by backscatter patterns across a glacier surface, is necessary to understand how and why an elevation bias can be detected on glacierized terrain in InSAR DEMs. This potential elevation bias occurs due to the combination of scattering mechanisms in a medium composed of air, water and ice which results in the identification of the *mean phase center* of the backscattered signal as being located below the true surface (Rizzoli et al., 2017a). The location of the mean phase center is the focal position of the apparent surface reflection from a target, derived from the combination of backscattered signal from all the scatterers within the radar beam (Müller et al., 2011). These signals are further averaged and combined for the construction of a DEM. When volume scattering occurs, the scattering signal comes from different depths and the mean phase center is then located within the volume, below the surface. Hence, in glacier facies where strong volume scattering can occur (e.g., dry snow zone, percolation and saturation zone) the calculated surface elevation in InSAR DEMs can be lower than the physical surface (Rizzoli et al., 2017a). As the scattering mechanisms and intensity are strongly dependant on the snowpack properties and wavelengths, a range of elevation biases have been calculated for different radar bands. A few studies providing values of this bias at C-band and X-band SAR are reviewed in the next section.

Some studies refer to this bias as the *penetration bias* or the *penetration depth bias* (e.g., Zhao & Floricioiu, 2017; Abdullahi et al., 2018) because it describes the capacity of the radar signal to penetrate the snowpack that allows for volume scattering and location of the mean phase center below the surface. The strict definition of penetration depth refers to a measure of how far an electromagnetic wave travels into a medium (either as the power, one-way or two-way penetration depth) and depends on scattering and absorption losses (Müller et al., 2011). Such a value is not necessarily equal to the difference between the true surface elevation and the location of the mean phase center averaged for an InSAR DEM pixel (Dall et al., 2001; Dall, 2007). Hence,

in this study we use the term *elevation bias* instead of penetration depth bias, to refer directly to the height difference measured between the true surface and the surface elevation of the InSAR DEM.

As mentioned above, the elevation bias is strongly dependant on the occurrence of volume scattering, which causes decorrelation in interferograms and affects the quality of the DEMs. When multiple scatterers located below the surface contribute to the backscatter within a single pixel, the acquisition of SAR images from two slightly different angles in across-track interferometry increases the uncertainty of the interferometric phase (Martone et al., 2016). Hence, the coherence of an interferogram contains information that can be used to differentiate glacier facies as it provides a good indication of snowpack characteristics (Rizzoli et al., 2017b). The contribution of volume decorrelation to coherence can be isolated by quantifying the other decorrelation factors (e.g., from baseline length, temporal difference and signal to noise ratio). This technique was used in Rizzoli et al. (2017b) to isolate volume decorrelation and successfully classify different snow facies in Greenland. They further used a model relating volume decorrelation to penetration depth based on work by Hoen and Zebker (2000) to estimate the elevation bias in TanDEM-X DEMs. Volume decorrelation is strongly linked to HoA as this parameter is used to convert the location of the mean phase center to height information in the DEM. Loss of coherence due to volume scattering decreases with larger HoA (Martone et al., 2016). The HoA is inversely dependent on baseline length (Eq. 2.1) and on terrain where strong volume scattering occurs, the critical baseline (i.e., the baseline at which the correlation is too low for interferogram phase information to be useable), is reduced (Hoen & Zebker, 2000).

A preliminary linear model was developed in Abdullahi et al. (2018) to estimate the elevation bias from TanDEM-X DEMs in Greenland. The model is based on two parameters: coherence and backscatter intensity, as they both influence the location of the mean phase center. The goal of developing such a model is for it to be applicable on all glacierized terrain without preliminary assumptions of the imaged medium, notably of its dielectric properties governing the penetration depth of the radar signal in snow and ice. Modelled elevation biases (-8 m to +3 m) in Abdullahi et al. (2018) were validated against surface elevations from ICESat points, and gave a correlation coefficient of 73 % with a RMSE of 0.7 m. In light of the discussion above and as suggested by Abdullahi et al. (2018), isolated volume decorrelation from the coherence, as well as HoA and baseline, could explain the remaining variability that is not captured by the preliminary linear

model. In accordance with the thesis objectives (Section 1.1), we will investigate the influence of these parameters on calculated elevation bias during our validation of TanDEM-X surface elevation on DIC, and compare the observed relationship with that presented in Abdullahi et al. (2018).

2.4 Previous Quantitative Assessments of Elevation Bias in TanDEM-X and Other InSAR DEMs in the Context of Glaciological Applications

In this section a review is provided of some studies which have quantified the elevation bias in surface elevations derived from InSAR DEMs at C-band (7.5 -3.75 GHz, 4-8 cm) and X-band (12-7.5 GHz, 2.5-4 cm) frequencies (Moreira et al., 2013). Early studies which investigated elevation bias on glacierized terrain used airborne SAR systems and focused on the Greenland and Antarctic ice sheets, where large elevation biases were detected in the dry snow zone. For example, Rignot et al. (2001) reported an elevation bias of up to 10 m in dry cold firn in central Greenland, but around 1-2 m on exposed ice, based on a comparison of IceBridge ATM laser altimetry data with elevations derived from an airborne C-band SAR. A similar study was carried out by Dall et al. (2001), on an ice cap in East Greenland. For the percolation zone an elevation bias of up to 13 ±1.5 m was calculated, but in the saturation zone it averaged zero due to high water liquid content (acquisitions were in August), but with much higher standard deviation of 3 to 7 m. They attributed the larger variability in the saturation zone to lower backscatter and lower signal to noise ratio.

Most recent studies which quantified the elevation bias at X-band using TanDEM-X data have processed their own high-resolution DEMs from Co-registered Single-Look Complex files, a co-registered pair of raw radar images, from TanDEM-X and/or TerraSAR-X (e.g., Rankl & Braun, 2016; Seehaus et al., 2015). These studies reduce elevation bias over stable terrain by co-registering their DEM with contemporary higher resolution point elevation datasets such as IceBridge ATM and field GPS measurements. A few studies using the DEMs processed by DLR, such as those used in this study, have been undertaken (e.g., Groh et al., 2014; Rizzoli et al., 2017b; Milillo et al., 2019).

Elevation change over Thwaites Glacier in Antarctica was calculated with TanDEM-X DEMs by Groh et al. (2014). Comparison with IceBridge ATM laser altimetry revealed an average elevation bias of 3.7 m and 5.7 m along two parallel transects over dry snow. A fixed offset based

on these average values was then applied to the DEMs to continue their analysis. In the northern Antarctic Peninsula, a seasonal variation in the depth of the signal phase center in TanDEM-X DEMs on the order of 2-3 m was observed by Seehaus et al. (2015). To minimize this bias in calculations of elevation change, they prioritized the use of summer scenes acquired during melt when almost zero penetration (and therefore no elevation bias) is assumed. In Greenland, comparison of TanDEM-X DEMs with ICESat points from 2003 to 2009 revealed a mean bias of 5.38 ±1.90 m in the dry snow zone, 4.30 ±1.74 m in the percolation zone and 3.74 ±2.32 m in the saturation zone (Rizzoli et al., 2017b). Temporal differences between the DEMs and the ICESat points and TanDEM-X calibration procedures were listed as two other parameters that might contribute to these elevation biases.

In a study calculating geodetic mass balance for glaciers in the central Karakoram region in Asia, Rankl and Braun (2016) assumed that the elevation bias at high elevation (>5,000 m) where dry snow conditions prevail, was equal in a SRTM X-band DEM from 2000 and a TanDEM-X DEM from 2012. They argued that no elevation bias would then affect absolute detected thickness change using these datasets, and their geodetic mass balance estimates. A similar technique was used by Jaber et al. (2013), when TanDEM-X and SRTM C-band DEMs were used to compute elevation change in the Southern Patagonian Icefield. They only used acquisitions from the summer, when the surface was wet at all elevations, to neglect the effect of penetration as surface scattering dominates in these conditions. Another study by Pandey et al. (2016) compared the accuracy of TanDEM-X DEMs on very steep and rough glacierized Himalayan terrain with ASTER DEMs, SRTM C-band DEMs, and GPS and ICESat points. All three types of DEM showed large discrepancies with validation elevation datasets due to the complexity of the terrain. They still concluded that TanDEM-X provided the best elevation information on glacierized terrain (RMSE of ~12 m for GPS points) and represented most accurately the rugged topography, showing the potential of using TanDEM-X DEMs for improving estimates of glacier thickness changes in such regions.

One method put forward by Rott et al. (2014) to estimate the elevation bias in TanDEM-X DEMs is to use a radiative transfer model to model the volume scattering and absorption of radar signal in a fixed subsurface. They modelled the depth of the phase center for conditions in the northern Antarctic Peninsula as being ~1 m below the surface in the percolation zone, and ~6 m

below the surface in the dry snow zone, and suggested that the elevation change they detected in the percolation zone refers to the elevation change of the last summer refrozen firn layer below the snowpack.

The relationship between elevation bias and backscatter intensity was investigated by Zhao & Floricioiu (2017) at two sites in Antarctica using GPS and IceBridge ATM data. Reported elevation bias ranged from -3.5 to -7.0 m in dry snow with an average standard deviation of 2.96 m, compared to 0.3 to -1.5 m on blue ice areas with an average standard deviation of 2.03 m. Over blue ice, the elevation bias is non-significant as it is lower than the TanDEM-X accuracy of ±2 m. Zhao and Floricioiu (2017) reported only a mild correlation (0.23 to 0.54) between backscatter and elevation bias in the dry snow zone.

Studies that calculated the error term induced in their geodetic mass balance estimates when using InSAR DEMs have revealed that it can be quite significant. In a study by Gardelle et al. (2012a), the elevation bias in SRTM C-band DEMs was corrected using the elevation of SRTM X-band DEMs as it was assumed to be smaller due to a smaller wavelength. The difference in these biases in the Karakoram region was on average 3 m and reached up to 5 m at elevations > 5500 m. The effect of this correction was significant (-0.29 m w.e. a^{-1}) in their later published estimate of mass balance in the region from 1999 to 2008 (+0.11 ±0.22 m w.e. a^{-1}) (Gardelle et al., 2012b). A similar elevation bias of 4-6 m was detected in the Mont Blanc area, France, by Dehecq et al. (2016) at higher elevations, where dry snow is present, from the comparison of TanDEM-X DEM and optically stereo-derived DEMs from Pléiades. They compared geodetic mass balance calculations from both DEM datasets and estimated that the systematic bias from using TanDEM-X DEMs for two specific glaciers was -0.23 m w.e. and -1.66 m w.e. for one year studied.

This brief overview of previous studies assessing the magnitude of the elevation bias in snow and ice in InSAR DEMs reveals that elevation bias is on average smaller at X-band than C-band, especially in the dry snow zone. Elevation bias on glaciers as detected in X-band SAR is on the order of a few meters (~3 to 7 m), is larger in the dry snow zone than in the percolation zone, and might display more variability in the saturation zone. Elevation bias can be measured in the bare ice zone when conditions are dry, but is potentially non-significant depending on the accuracy of the DEM used. Impact of seasonality and steep local slopes are two parameters also affecting the detection of an elevation bias. Lastly, errors in geodetic mass balance calculations using

uncorrected TanDEM-X data can be significant where dry snow conditions prevail and further research should be carried out to determine their effect on large scale estimates of geodetic mass balance (Gardelle et al., 2012b).

2.5 TanDEM-X Validation Site: Devon Ice Cap

2.5.1 Ice Cap Geometry

Devon Ice Cap (74°30' to 75°50'N; 80°00' to 86°00' W) covers most of the eastern part of Devon Island in the Queen Elizabeth Islands (QEI), the northern part of the Canadian Arctic Archipelago (CAA) (Fig. 2.4). Based on satellite imagery from 1999-2000, the ice cap had an area of ~14,000 km^2 (Burgess & Sharp, 2004), making it one of the largest ice masses in the Canadian Arctic. The main active ice cap portion, when excluding the SW arm, covered 12,794 km^2 in 2000 (Abdalati et al., 2004).

The DIC has a simple dome-like shape with ice divides running in the four cardinal directions from the summit at 1921 m a.s.l. (Boon et al., 2010). The western side of the ice cap is land terminating with a gentle slope. Mountain ranges appear at the north and south of the main east-west ice divide, with major outlet glaciers draining the eastern half of the ice cap where they flow in steep valleys and mostly terminate in tidewater. There is a large piedmont area (approximately 400 km^2) in the southeastern part of the ice cap where ice is not well constrained by the topography and surface slopes are gentle. The southwestern arm of the ice cap consists primarily of near stagnant, ablating ice (Burgess & Sharp, 2004), and for this reason is often not considered as part of the active ice cap area and is excluded from mass balance studies.

Extensive ice thickness measurements of DIC were obtained from airborne ice-penetrating radar (radio-echo sounding) in 2000 (Dowdeswell et al., 2004). The ice cap is thickest (700-800 m, max. 880 m) in the SW region. The large piedmont area and the western margin has ice thinner than 350 m and the inactive southwestern arm of the ice cap has an ice thickness of 100 m or less (Dowdeswell et al., 2004). Extracted bed topography revealed a central upland plateau and steep valleys that control the location of the major outlet glaciers, with a total of 8% of the bed below sea level. From these radar measurements the volume of the main ice cap has been calculated to be 3,980 km^3 (with another 130 km^3 comprising the SW arm), corresponding to ~10 mm of global

sea level equivalent (Dowdeswell et al., 2004). Recently, two hypersaline subglacial lakes have been discovered from radio-echo sounding measurements near the NW and SW ice divide of the ice cap (Rutishauser et al., 2018). This is the first evidence of such lakes in the Canadian Arctic and might represent significant microbial habitats, which could be analogues for potential ice-covered brine lakes on other planetary bodies.

Changes in ice cap area and their and relationship to basin hypsometry were investigated in a study by Burgess and Sharp (2004) using air photographs from 1959-1960, Landsat 7 ETM+ satellite images from 1999-2000, and surface elevation data from the Canadian Digital Elevation Model (CDEM). Over the 40-year period the ice cap area decreased by 2.4%, equivalent to 332 ±40 km^2. This loss primarily occurred on the eastern side of the ice cap from the retreat of tidewater glaciers and increase of exposed bedrock areas, denoting general thinning of the ice cap surface. Retreat of the SW arm was also significant over this period, reflecting the loss of the accumulation area in this basin. Slight advance of the ice cap was found in the NW margin with advances of the terminus of some western outlet glaciers, Sverdrup (+250 m) and Croker Bay glaciers (+100-400 m), potentially still responding to cooler climates of the Little Ice Age (LIA, ~1850).

Burgess and Sharp (2004) also estimated the response time of the ice cap, which can be defined as the timescale over which a glacier responds to climate forcing to reach a new equilibrium state (Benn & Evans, 2010). For these calculations the mass balance flux at the different glacier termini was interpolated from the in-situ mass balance measurements on the NW basin for the period 1961-1998, with ice thickness data from Dowdeswell et al. (2004). Small basins at the periphery of the ice cap with low accumulation areas not extending to the main ice divides, and lower mean elevation, were found to have shorter response times (100-400 years) and are mostly located at the southern and eastern margins. In contrast, basins terminating at higher elevations, with low terminus ablation rates and accumulation areas extending far into the ice cap interior have the longest response time (>700 years), and are mostly located in the western region. As basins with short response times are most sensitive to climate forcing, statistical analysis suggests that their decrease in area over the 1960-2000 period is likely a response to warming trends post-LIA. This highlights the contrast in response between the eastern and western sectors of the ice cap to climate forcing over the 40 year study period, with LIA cooling yielding advance or lower area loss and post-LIA warming yielding large area loss (Burgess & Sharp, 2004).

2.5.2 Ablation and Accumulation Patterns: Influence of Regional Climate

Devon Island is in a polar desert climatic region, receiving <200 mm of precipitation on average per year, with minimal interannual variability (Gardner & Sharp, 2007). Mean monthly temperatures on DIC are below 0°C in every month with maximums in July. Air temperature inversions and katabatic winds are also significant features of the regional climate, influencing ablation and accumulation patterns (Boon et al., 2010). Early research by Koerner (1970a) estimated that the long-term equilibrium line altitude (ELA) was 950 m for the NW sector, 800 m for the SE and 875 m a.s.l. for the SW and NE (Koerner, 1970a; Mair et al., 2005; Burgess & Sharp, 2008), although the ELA has recently been reported as high as ~1500 m a.s.l. in the NW basin in 2015 (Burgess, 2017).

Most accumulation on DIC occurs in the summer and early fall (July-October). It is much greater on average in the SE sector of the ice cap (~50 cm w.e. a^{-1}) and decreases gradually towards the NW sector (~10 cm w.e. a^{-1}) (Koerner, 1970a). This difference is caused by the proximity of the SE region to the North Open Water (NOW) polynya at the head of Baffin Bay, which provides the dominant moisture supply for the ice cap (Koerner, 1977). Frequent cyclonic systems in the NOW bring large snowfall to the ice cap in both winter and summer (Boon et al., 2010). Winter snow redistribution from katabatic winds at the summit creates an increase in accumulation from the summit towards the margins of the ice cap. Studies by Koerner (1966) and Mair et al. (2005) report that strong katabatic winds can scour the surface in the ~1600 to 1800 m a.s.l. elevation range (but not directly at the summit), exposing the previous summer surface. The snow accumulation gets redistributed to elevations lower than ~1600 m a.s.l., creating a gradient of increased accumulation from the summit towards the margin (Koerner, 1966). A detailed study of accumulation patterns in the Belcher Glacier catchment (NE basin) by Sylvestre et al. (2013) estimated snow water equivalent (SWE) accumulation rates from ground penetrating radar (GPR) transects. Along with elevation, their analysis suggested that slope and aspect are also significant factors explaining variability in SWE. They linked the effect of aspect to the dominance of northwest winds on the ice cap as increased snow deposition occurs on lee-side locations (generally east-facing slopes).

At high elevations summer balance on DIC can be positive, suggesting that variability in snow accumulation is important in the variability of annual net balance (Colgan & Sharp, 2008).

Analysis of shallow firn cores suggested that interannual variability in accumulation primarily occurs due to changes in sea ice extent and concentration in the surrounding QEI, and the strength of low-pressure systems in Baffin Bay that influences the trajectory of air masses onto the ice cap (Colgan & Sharp, 2008). From the results of 11 studies over the past 40+ years, net accumulation (difference between summer melt and sum of annual snowfall, superimposed ice and internal accumulation) on DIC ranges between 0.13 to 0.27 m w.e. a^{-1} (Boon et al., 2010). Early work related to snow facies on DIC was completed by Koerner (1970b) who analyzed the elevation and layer formation of superimposed ice, and used field measurements to locate the equilibrium line. Although difficult to measure over large areas, his work suggested that superimposed ice is an important contributor to net accumulation on DIC (Koerner, 1970b).

The ablation season on DIC typically begins between early June and early July, and ends between late August and early September (Wang et al., 2005). The main form of ablation is through surface mass loss, which is primarily controlled by the intensity and duration of summer melt (Koerner, 2005). It is negatively correlated with surface elevation above sea level and proximity to Baffin Bay (Boon et al., 2010). Eastern margin basins have larger mass balance gradients overall, experiencing large accumulation and the largest ablation rates on the ice cap (Burgess et al., 2005). DIC also loses some mass through iceberg calving, which could account for up to 30% of the total mass loss (Burgess et al., 2005). Dynamic ice discharge (i.e., iceberg calving) from DIC has been estimated to average 0.46 Gt a^{-1} over 1991-2015 (Millan et al., 2017) and 0.41 ±0.11 Gt a^{-1} in 2009 and 2011-15 (Van Wychen et al., 2017).

Interannual variability and recent trends in the mass balance of Canadian High Arctic glaciers have been linked to the evolution of synoptic-scale climate and circulation patterns in the Arctic. Gardner and Sharp (2007) studied the variability in mass balance of four long-term series in the Canadian Arctic for the 1963-2003 period, including DIC, and analyzed their correlation with summer air temperatures and the location of July 500 mb Arctic circumpolar vortex. Their findings show that increasingly negative mass balances since 1986-87 are due to the movement of the vortex eastward and its weakening, increasing high pressure ridging over the QEI and warmer summer air surface temperatures, enabling extreme melt years.

Sharp et al. (2011) continued the analysis to investigate the increasing trend of negative mass balance on QEI ice caps since the 2000s. Summer air temperature records at Eureka and Resolute,

Nunavut, show that the warmest summers since the 1950s occurred after 2005, with recorded temperatures correlating well with the ones recorded in the summit regions of DIC and Agassiz Ice Cap (northern Ellesmere Island). Land surface temperature (LST) data on glacierized surfaces derived from MODIS (Moderate Resolution Imaging Spectroradiometer) imagery revealed an increase over the whole of the QEI since the 2000s (Sharp et al., 2011). For DIC, mean LST in the 2005-2009 period exceeded the records from 2000-2004 by 0.8°C. Interannual variability is then controlled by the occurrence of very warm summers, which can eliminate the positive mass balance of several years caused by cold summers (Boon et al., 2010). Hence, changes in summer temperatures can explain the recent warming trend observed on CAA ice caps and on DIC, where 58% of the mass loss between 1963 and 2009 occurred in the 2000-2009 period (Sharp et al., 2011). The study of Mortimer et al. (2016) improved the methodology and extended the study of the duration and intensity of summer melt on glaciers and ice caps of the QEI from MODIS-derived LST to 2015. Mean summer glacier surface temperatures were anomalously high in the 2005-2012 period, which is probably the warmest in the region since 1948. On DIC the SE region had an apparent decrease in LST over the 2000-2015 period, indicating a trend towards shorter and/or less intense melt seasons. Mortimer et al. (2016) suggest that this phenomenon, also observed on the SE coast of Ellesmere Island, is due to the proximity to open water sources, where the NOW polynya extent is large in warm summers and more frequent storm systems bring snowfall to the SE basins, decreasing the surface albedo and reducing melt.

In the last decade, the availability of higher resolution scatterometer (active radar sensor) data has enabled the study of melt duration and snow facies patterns in the QEI. These parameters are expected to correlate well with surface mass balance data and provide crucial information to estimate mass balance on a larger scale from remotely sensed data. Wang et al. (2005) developed a methodology to identify melting areas from backscatter values of the ice cap surface and estimated melt season duration for the 2000-2004 period for all ice caps in the Canadian Arctic. The average annual melt season for DIC during this period was 42.1 days. Wolken et al. (2009) developed the analysis further by classifying snow facies area and determining melt duration for all Canadian Arctic ice caps for the period 1995-2005. They observed large spatial variability in the facies boundaries, mostly for the glacier ice facies. Overall, their results indicated that increased air temperature and melt duration correlates with an increase in glacier ice facies, a

decrease in the percolation and saturation facies, and a general increase in the elevation of inter-facies boundaries.

The results of Wolken et al. (2009) correlate well with the reconstructed net accumulation record of DIC from shallow firn cores at high elevation, which have suggested that a shift of all glacier facies towards higher elevation occurred in the 1989-2003 period (Colgan & Sharp, 2008). The lower limit of the dry snow zone was modelled at 2025 m a.s.l. for 1989-2003, which is higher than the ice cap summit elevation of 1921 m a.s.l., suggesting the loss of this facies, or its intermittent nature, over this period. Indeed, melt over the entire elevation range of DIC was reported for the period 2000-2015 from LST analysis (Mortimer et al., 2016). However, a pseudo-dry snow zone was detected by De Jong (2013) from 2004 to 2006 by analysing post-freeze up backscatter patterns in Envisat ASAR imagery from 2004 to 2011. Combined with the analysis of near-surface temperature data, it was argued that cool summer temperatures were responsible for the lack of formation of large melt features at the highest elevations (~ >1700 m a.s.l.), creating a zone with significantly lower backscatter compared to the percolation zone.

The most recent analysis of facies boundaries on DIC has been described by Gascon et al. (2013) from GPR profiles conducted on the southwestern region of the ice cap. Since spring 2007, the upper limit of the superimposed ice zone migrated 14.5 km upglacier to 1520 m a.s.l., and the upper limit of the wet snow zone migrated 4.5 km upglacier to 1640 m a.s.l. due to increased meltwater production and its percolation and refreezing in the firn column (Gascon et al., 2013). An increase in firn densification was also reported in Bezeau et al. (2013) who compared firn properties in multiple shallow firn cores on DIC between 1400-1900 m a.s.l. collected between 2004 and 2012. They observed increased densities from 13 to 80% in the upper ~2.5 m of cores and the development of thick ice layers (Bezeau et al., 2013). A very good correlation between ice layer thickness and glaciological mass balance was found at high elevation over the ice cap (1600-1800 m a.s.l.), where larger negative mass balance correlated with thicker ice layers (Gascon et al., 2013).

2.5.2.1 Velocity Patterns and Ice Dynamics

Changes in velocity on a glacier surface are typically associated with surface elevation changes (thinning or thickening) due to the dynamic redistribution of ice at different elevations. Understanding patterns in ice dynamics is therefore necessary to accurately interpret mass balance

measurements, whether derived from in-situ or remote sensing data. The velocity fields of DIC have been well studied (e.g., Van Wychen et al., 2014, 2017; Burgess & Sharp 2008; Dowdeswell et al., 2004) following recent improvements in satellite image availability and methods to process them, including along-track InSAR and speckle-tracking. These studies have enabled the determination of clear basin divides (Dowdeswell et al., 2004), classification of distinct flow regimes (Burgess et al., 2005), and estimation of mass balance fluxes, such as calving and dynamic discharge of DIC (Van Wychen et al., 2012) and its temporal variability (Van Wychen et al., 2017).

Topography provides the main control on ice velocities on DIC. The eastern side is primarily drained by multiple large and fast flowing outlet glaciers, which extend far inland from the ice cap margin. The slow-moving western sector is drained primarily by broad sheet flow, with few outlet glaciers close to the ice cap margin (Burgess et al., 2005). Low surface velocities ($\leq$20 m a^{-1}) are characteristic of high-elevation interior regions of the ice cap with a cold or frozen bed, while higher surface velocities ($\geq$20 m a^{-1}) are found over valleys leading to major outlet glaciers which are likely warm-based (Mair et al., 2005; Boon et al., 2010).

Dowdeswell et al. (2004) provided the first complete snapshot of the velocity fields of DIC from ERS 1/2 data from 1992 and 1996, identifying the extent and distribution of fast flowing ice. Burgess et al. (2005) assessed the velocity field of the ice cap from ERS 1/2 and Radarsat-1 data acquired in the mid-1990s and 2000s, which enabled estimation of iceberg discharge from the ice cap for the first time. They characterized four main flow regimes on the basis of patterns in the ratio of surface velocity to ice thickness and local driving stresses (ice motion by deformation only or inclusion of basal motion). The map of these flow types was recently updated by Van Wychen et al. (2017), who analyzed Landsat 7 ETM+ and Radarsat 2 imagery over the period 1999-2015 to quantify the variability in ice motion over the entire ice cap and its implications for ice discharge. Flow regime 1 is the most extensive (84.45% of the ice cap area) and indicates ice frozen to its bed and movement by internal deformation only. Flow regime 2 (14.27% of the ice cap area) indicates basal ice approaching pressure-melting point and is found along the upper portions of the valleys of main outlet glaciers. In flow regime 3, the contribution in basal sliding is increased and indicates a reduction in ice viscosity; this flow regime applies to the lower sections of some of the major outlet glaciers only (1% of the ice cap area). Flow regime 4 (0.28% of the ice cap area) indicates high basal motion and deformation of basal sediments, and is found at the lowermost terminus region of Belcher, South Croker, Fitzroy, East-7 and Southeast-2 glaciers.

From the analysis of velocity patterns over 16 years, Van Wychen et al. (2017) classified the observed variability into categories of surging, pulsing and constant acceleration. As was previously suggested by Burgess and Sharp (2008), Southeast 1 and 2 glaciers have a surging behaviour that is also supported by visible surge-type geomorphic features. Fitzroy, East-5 and East-7 glaciers have been classified as pulsing, which describes multi-year velocity variability initiated near the calving front, rather than in the upper regions that is typical of surging. Belcher Glacier has undergone constant acceleration over its lower reaches that is likely driven by terminus thinning (Van Wychen et al., 2017). Their results suggest that bed morphology, and possible transition from bedrock to marine sediments, is significant in regulating the flow of DIC, where greatest variability in velocities between years occurs in locations where the bed is below sea level.

A thorough study of the relative contributions of ice dynamics versus surface mass balance (SMB) in controlling thickness change on the ice cap was conducted by Burgess and Sharp (2008) over the 1960-1999 period. They used the method of flux divergence to calculate volume change and equivalent contribution to sea level rise for 1960-1999. Basin-wide rates of ice thickness change were estimated by the subtraction of a modelled ice flux in a balanced state from the measured ice mass flux. The former was derived from modelled ice cap velocities in a balanced state by incorporating long-term (1963-2000) reconstructed mass balance from ice core data, while the latter was derived from depth-averaged ice velocities from interferometric SAR surface velocities (Burgess et al., 2005). Both velocity estimations (modelled and measured) were multiplied by the average ice thickness (Dowdeswell, 2004) at the ELA to estimate modelled and measured flux. The study reports significant variability in the rates of thickness change in both sign and magnitude in the different basins of the ice cap. For the accumulation zone, slight thinning (on the order of ~0.2 m w.e. a^{-1}) was observed for the southern and eastern regions and no detectable change was observed for the northern region. For the ablation zone, a thickening was observed in the SW region (0.55 ± 0.22 m w.e. a^{-1}) but was not detectable for the southeast region. On the opposite side of the ice cap, the ablation zones of the northern region were slightly thinning. This study yielded some insights into changes in ice flow dynamics that are not easily accounted for by changes in surface mass balance alone, especially on outlet glaciers where ice dynamics have a significant impact on patterns of thickness changes. They therefore concluded that ice dynamics must be included in any model aimed at assessing the net mass balance of large ice caps as a whole.

2.5.3 Mass Balance: Glaciological Time Series and Other Estimates

The in-situ SMB network on DIC started in 1961 under the direction of Dr. Roy Koerner and is now run by the Geological Survey of Canada (GSC). Calculating mass balance from in-situ measurements refers to the glaciological method (Cogley et al., 2011). Located on the NW basin of the ice cap (~1810 km²), including Sverdrup Glacier, the mass balance transect today contains 43 stakes and 5 automatic weather stations (AWS) which measure air temperature and relative changes in the snow/ice surface height (Fig. 2.4). The long-term average mass balance for the NW basin is -0.14 m w.e. a^{-1} (1961-2015) (Burgess, 2017). On average, total thinning has been ~7 m across the NW basin since 1960, with an estimated 50% of this thinning occurring since 2005 (Burgess, 2017).

Glaciological measurements only reflect the mass balance at the surface of a glacier and do not take into account dynamic changes, iceberg calving, or internal balances (Benn & Evans, 2010). Uncertainties in surface mass balance from glaciological measurements arise mostly from the representativeness of a particular stake network of the entire elevation range and associated mass balance conditions. Based on research at White Glacier, Axel Heiberg Island, Nunavut, this random error has been previously assumed to be ~200 mm w.e. a^{-1} at any given stake (Cogley and Adams, 1998). Another source of error in these measurements, which also affects geodetic mass balance calculation using DEM differencing, is the determination of the actual thickness change observed in the accumulation zone that corresponds to a mass loss through runoff. Accumulation can be partly transferred to layers beneath the surface through percolation and refreezing, densifying the firn layers below, meaning that lowering of the surface in the accumulation zone is not necessarily equivalent to a mass loss from the ice cap (Koerner, 1970a; Bezeau et al., 2013).

The glaciological time series provides precious information about the evolution of the mass balance of DIC in the NW basin, but cannot be easily extrapolated to the entire ice cap. It is likely that mass balance evolution in this basin is not representative of the ice cap as a whole due to significant spatial variations in hypsometry, variations in prevalent weather patterns influencing accumulation and ablation patterns, and evolution of ice velocities and associated dynamic responses as discussed in the previous sections. The mass balance (or some components of mass balance) of the entire DIC have previously been estimated using various methodologies and datasets, sometimes including the glaciological time series.

Mass loss rates ranged from -0.038 m w.e. a^{-1} (firn-based calculation, Abdalati et al., 2004) to -0.17 m w.e. a^{-1} (from combination of Mair et al. (2005) and Burgess et al. (2005)) over the 1960-2015 period. Volume area scaling methods, surface mass balance and flux divergence methods yielded similar results (-0.089 to -0.17 m w.e. a^{-1}) using the density of ice (Burgess & Sharp, 2004; Burgess & Sharp, 2008). Only one study reports clear numbers for the SW arm (Burgess & Sharp, 2004), with their change in volume equivalent to a lowering of the surface of 3 m over the main ice cap region and of 8 m over the SW arm only, which had the largest proportional area change over the 1960-1999 period. Extrapolating thickness change from IceBridge ATM data from 1995 and 2000 over all ice cap basins as done by Abdalati et al. (2004) induced a significant bias in their mass balance calculation because observed thickening at high elevations was related to dynamic processes and not from increased accumulation as was shown by Colgan et al. (2008). Some studies have looked at calving or dynamic flux in major basins only (Burgess et al., 2005; Van Wychen et al., 2012, 2014, 2017). They reveal that dynamic discharge is an important term in mass balance estimates, and is dominated by a few outlet glaciers, notably by the Belcher Glacier (Burgess et al., 2005; Van Wychen et al., 2017).

The most recent mass balance estimate of DIC from Millan et al. (2017) was calculated from the average of tidewater and non-tidewater terminating glaciers. The land terminating glaciers were assumed to have a constant rate of mass loss estimated to be 0.8 ±0.8 Gt a^{-1}, while the mass balance of tidewater glaciers over the period 1991-2015 was interpolated from data available for 10 years over this period. The Millan et al. (2017) study also used modelling to generate SMB data and to incorporate an ice discharge component. They reported that ice discharge accounted for 52% of mass loss over the northern QEI in 1991-2005, but after 2005 it shifted to contribute only 10% of the total mass loss due to the dominance of mass loss from enhanced runoff (i.e., surface melt). These findings agree with the most recent mass balance study in the CAA by Noël et al. (2018), who modelled surface mass balance at a 1 km resolution for the 1958-2015 period. Their results indicate that increased mass loss since 1996 in the QEI has occurred due to a combination of increased runoff and reduced precipitation. Increased runoff was also reported as the primary driver of the acceleration of tidewater glacier retreat in the CAA in the period 1958-2015 in a recent study by Cook et al. (2019). However, the refreezing of meltwater at high elevation in available firn pore space has partly compensated for the increased runoff and buffers mass loss for the northern CAA ice caps such as DIC (Noël et al., 2018). These findings correlate well with the

reported densification of firn layers since 2005 from ice core data on DIC (Bezeau et al., 2013) and upward migration of glacier facies (Gascon et al., 2013). Bezeau et al. (2013) reported that measured rates of firn compaction from 2004 to 2011 on DIC were significant when compared with the magnitude of thickness change derived from repeat airborne laser altimetry. They argued that estimating mass loss from altimetry measurement of surface elevation change can only be accurately undertaken if the temporal and spatial distribution, production, infiltration and refreezing of meltwater can be modelled reliably.

It can be difficult to directly compare the mass balance estimates of DIC derived from different methodologies, but one can conclude that they are mostly within uncertainty for the pre-2000 and post-2000 periods. The geodetic mass balance method has only been used by Abdalati et al. (2004) based on extrapolation of limited point data that yielded biased results. Use of DEMs for geodetic mass balance on DIC has not been carried out because of the lack of high-resolution DEMs covering the entire ice cap. TanDEM-X DEMs corrected for elevation bias would therefore be a very useful dataset for this purpose.

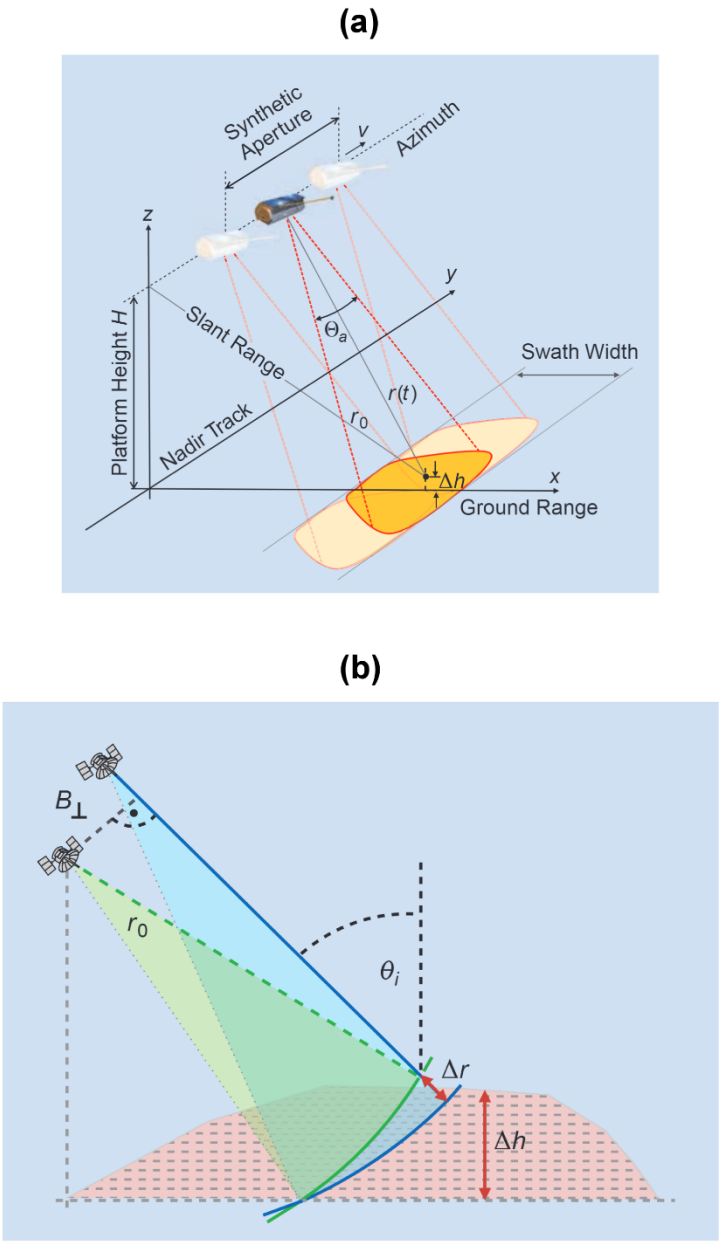

Figure 2.1 Illustration of: (a) Synthetic Aperture Radar (SAR) imaging geometry, (b) across-track SAR interferometry (from Moreira et al., 2013). In (a) the platform moves in the azimuth (or along-track) direction with a velocity $\boldsymbol{v}$. The swath width corresponds to the extent of the scene in the ground-range and depends on how long the radar is turned on for an acquisition. The synthetic aperture is represented by the combination of the highlighted areas from the beam width in the azimuth direction, $\boldsymbol{\Theta_a}$. $\boldsymbol{r_0}$ is the shortest approach distance in the slant range. In (b) azimuth direction is across the page. Incidence angle is $\boldsymbol{\theta_i}$ and effective perpendicular baseline is $\boldsymbol{B}_\perp$. A change in the surface height $\boldsymbol{\Delta h}$ causes a change in the range of a difference $\boldsymbol{\Delta r}$.

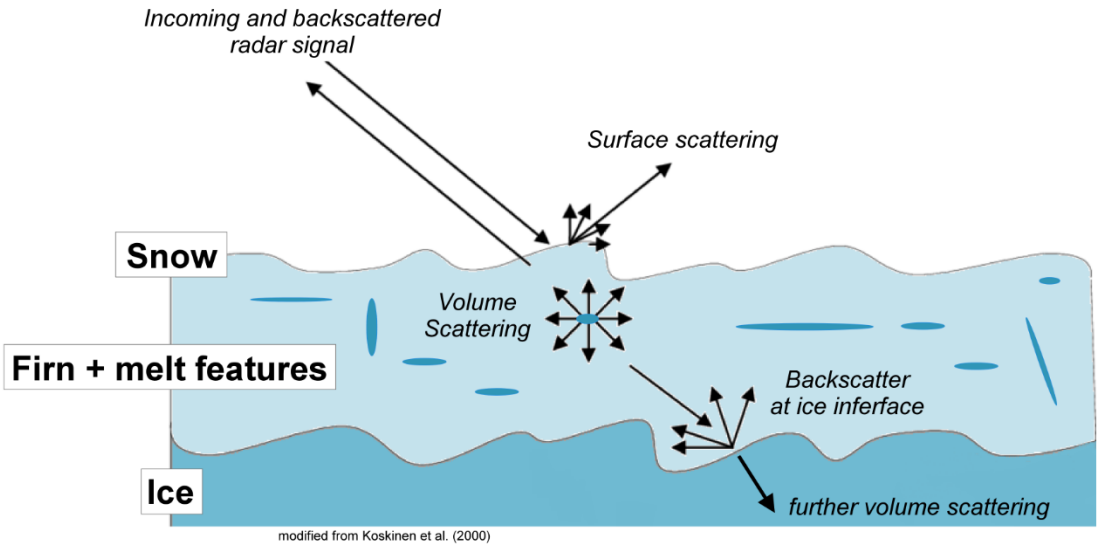

Figure 2.2 Scattering mechanisms of radar signals occurring on a glacier surface and subsurface. Figure modified from Koskinen et al. (2000).

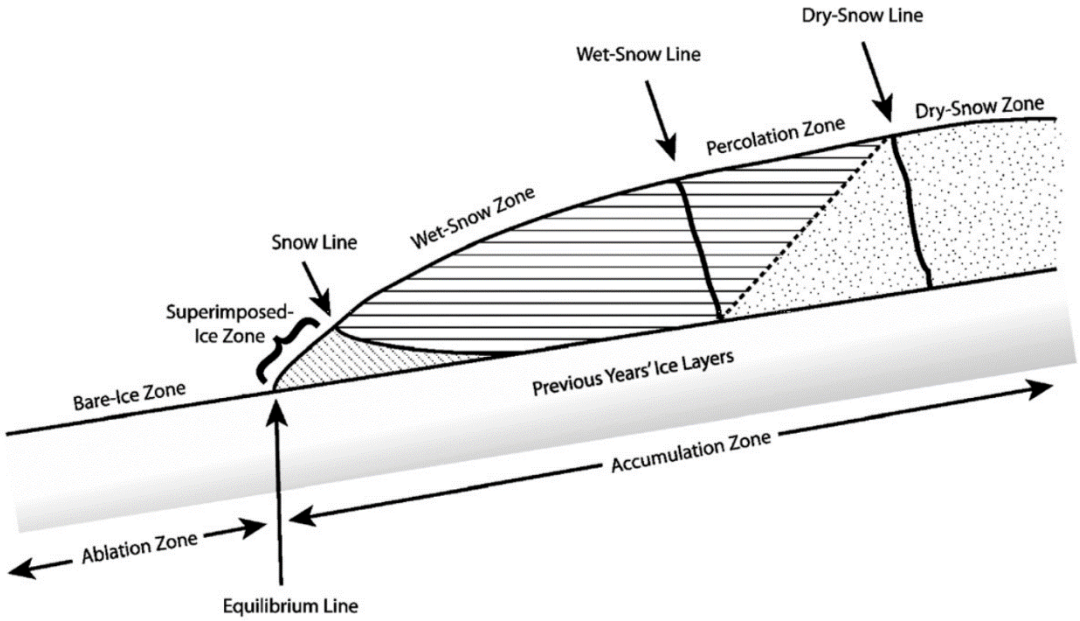

Figure 2.3 Glacier facies from Nolin and Payne (2007), based on previous work by Benson (1962) and Paterson (1994).

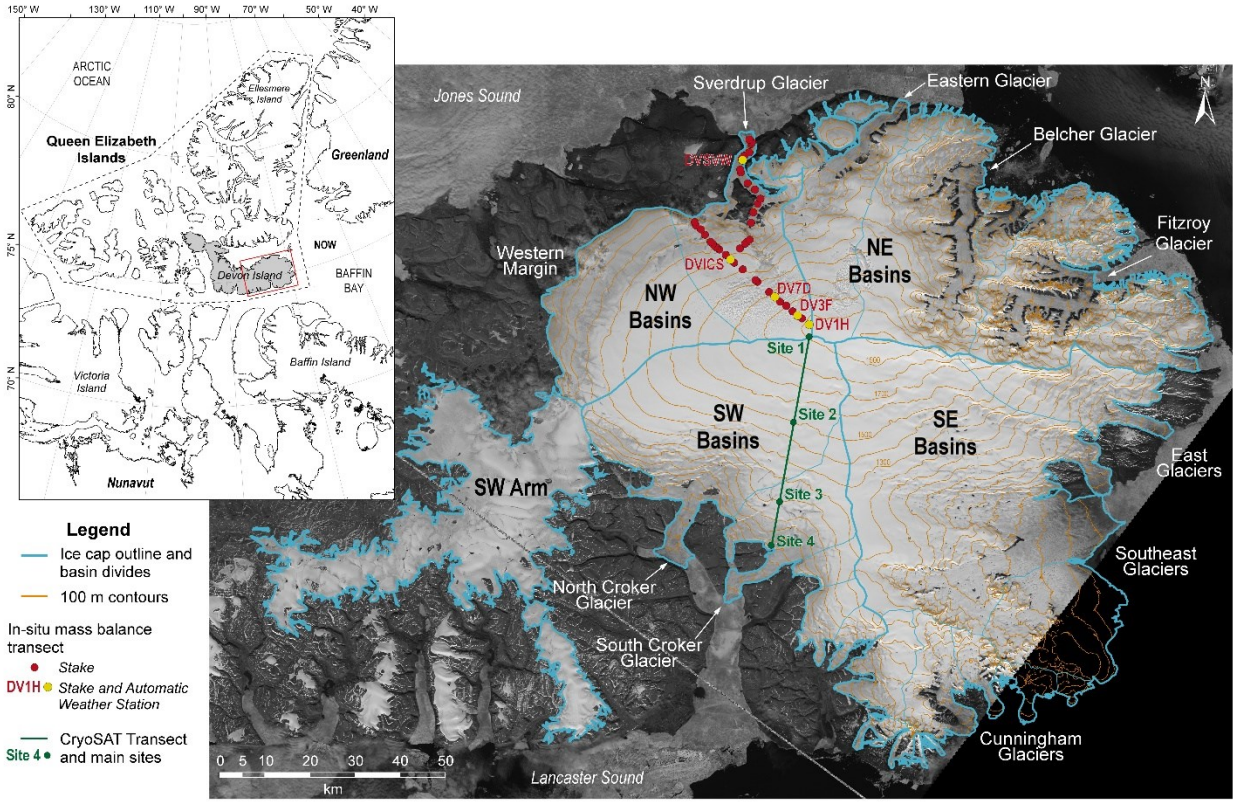

Figure 2.4 Map of Devon Ice Cap with basin outlines derived from Burgess and Sharp (2004) (see Table 3.6 for details), main outlet glaciers, location of the mass balance transect with automatic weather stations, the bedrock GPS stations and the CryoSat transect. Contours are extracted from the TanDEM-X 2010-14 mosaic. The North Open Water polynya is indicated in the inset as NOW. Background is a Landsat 7 ETM+ orthomosaic from summer 1999.

Chapter 3: Datasets and Methodology

In this chapter we start by providing a description of the TanDEM-X DEMs and auxiliary datasets used in this study, followed by a description of the elevation datasets used to validate the TanDEM-X DEMs. After this, the methodology to calculate the elevation bias of the TanDEM-X DEMs compared to the validation elevation datasets and its associated errors is presented. Finally, non-elevation datasets used to estimate the variability in interferometrically derived elevation from fall to spring, and subsurface datasets used to complement the analysis of the calculated elevation bias, are presented.

3.1 TanDEM-X DEMs and Auxiliary Data

The TanDEM-X satellite constellation contains two quasi-identical satellites TerraSAR-X and TanDEM-X flying in close orbit at approximately 500 km above the ground surface, both operating a SAR instrument at X-band (9.6 GHz, ~3.1 cm). Their bistatic configuration (one transmitter and two receiving antennas) permits the simultaneous acquisition of backscattered signal and the construction of highly accurate interferograms without temporal and atmospheric decorrelation (Rizzoli et al., 2017a). Scenes used to produce TanDEM-X DEMs were acquired using the stripmap mode in single horizontal polarization with a resolution between 2.4 to 4 m (Wessel, 2016; Fritz & Eineder, 2013). The TanDEM-X DEMs and auxiliary data used in this study were supplied by Dr. Birgit Wessel (German Remote Sensing Data Center, DLR) through the TanDEM-X proposals XTI_GLAC6627 and XTI_GLAC7335.

For our analysis, we used raw TanDEM-X DEMs (hereafter referred to as *rawDEMs*) which consist of the input DEMs used to produce the global TanDEM-X DEM mosaic. We used this product because each rawDEM has a specific acquisition date and accessible metadata concerning acquisition parameters, whereas such information is not available for the global DEM after the mosaicking process. We analyzed all 30 rawDEMs acquired over DIC during the frozen season from November 2010 to May 2018 (Table 3.1). This included the acquisition of two rawDEMs over DIC's NW basin during field data collection in May 2018.

3.1.1 Height Accuracy and Block Adjustment Procedure

All interferometric processing and calibration to produce the rawDEMs was done by DLR using their Integrated TanDEM-X Processor (ITP) and Mosaicking and Calibration Processor (MCP) (Wessel, 2016). The ITP processes the individual scenes to interferograms, then proceeds to phase unwrapping and geocoding (Fritz et al., 2011; Rossi et al., 2012; Lachaise et al. 2017). The MCP was only used for calibration (Gruber et al., 2012) and no mosaicking was performed on the rawDEMs, hence their suffix *raw*-. In this section, we detail the *block adjustment procedure* implemented in the MCP for DEM calibration as it was applied to the DIC rawDEMs because it impacts the vertical accuracy of the data product we used.

The block adjustment procedure consists of adjusting multiple overlapping rawDEMs over a large area to reduce remaining systematic height biases due to random phase errors, remaining instrument phase drifts and inaccuracies in baseline calculation (Gruber et al., 2012). Height offsets, tilts in the slant range dimension and slopes in the azimuth direction are calculated from height differences at tie-points within overlapping areas of rawDEMs and from differences to ground control points (GCPs). An error function for each rawDEM is solved using a weighted least-square adjustment technique to derive correction parameters independent from terrain parameters. Laser altimetry data from ICESat (2003-2009, NASA, L2 product, GLA14 Version 34, available through National Snow and Ice Data Center) is used for GCPs. Only the most reliable ICESat points are used based on an evaluation of the reflected signal, to choose the points closest to a signal representing open un-vegetated areas and flat terrain. Points overlapping higher coherence areas of the rawDEMs are also given more importance in the error function. Only the 10 best ICESat points per 50 km along the rawDEMs are selected and points with height differences above 100 m are rejected (Gruber et al., 2012). For rawDEMs of DIC, block adjustment was performed with other rawDEMs of the same acquisition date in the Canadian Arctic (Fig. 3.1). The area of these adjustment blocks expands from Devon Island, up northwest to Axel Heiberg Island and on part of Ellesmere Island, including many points over stable terrain (Fig. 3.1).

The absolute vertical height accuracy of the global TanDEM-X DEM mosaic (i.e., the uncertainty with respect to the WGS84 ellipsoid caused by random and systematic errors), is reported as ≤10 m at the 90% confidence interval (Rizzoli et al., 2017a). The relative vertical height accuracy, the uncertainty between two height estimates caused by random errors, is reported as ≤2

m for terrain with a local slope <20% and of ≤4 m for terrain with local slopes >20% at the 90% confidence interval (Rizzoli et al., 2017a). However, these values may not be valid for the individual rawDEM products over DIC following the block adjustment procedure as it is unknown if the height error introduced by using ICESat points over terrain with temporally-variable surface elevation (i.e., glacier- or snow-covered terrain) is less than the systematic height errors that are corrected for in all cases. A comparison of higher accuracy GCPs over stable terrain should therefore be undertaken as an absolute verification.

3.1.2 RawDEMs Auxiliary Data

To relate our calculated elevation differences between TanDEM-X DEMs and validation elevation datasets with SAR acquisition parameters, and to discuss the implication of the block adjustment procedure on height accuracy, we extracted three parameters from the rawDEM metadata: (1) vertical displacement applied following the block adjustment procedure, (2) HoA, and (3) perpendicular baseline (Table 3.1).

Three auxiliary rasters are also supplied with each rawDEM as supplementary information on the interaction of the radar signal with the surface and subsurface:

(1) Height Error Map (HEM): the value of each pixel represents the error (in m) of the elevation value of the DEM and is considered to be a random error (Wessel, 2016). It is in the form of a standard deviation which is calculated using the HoA as follows:

$$\sigma_{HEM} = HoA \cdot \frac{\sigma_\phi}{2\pi} \tag{3.1}$$

where σ_ϕ is the standard deviation of the phase, derived partly from coherence (Gruber et al., 2016). In the rawDEMs over DIC, we observe the smallest height errors (<0.5 m) in relatively flat bedrock areas where coherence is high. Observation of our data revealed that with lower coherence, snow- and ice-covered areas tend to have higher height errors (0.5 to 5 m). Areas with steeper slopes, such as sides of glacier valleys, have the largest height error (≥ 5m) due to the high probability of foreshortening, layover and/or shadow in the SAR data (Wessel et al., 2018). The HEM does not include any error contribution from the offsets applied during the block adjustment procedure.

(2) Amplitude (AMP): the value of each pixel is provided as the mean amplitude of both input SAR scenes. The amplitude reflects the backscatter intensity which has been calibrated to the ground range using the incidence angle. Amplitude has units in Digital Numbers (DN) (Wessel, 2016).

(3) Coherence (COH): each pixel represents the coherence as a unitless factor ranging from 0 to 1 and is a direct output from the interferometric processing (Wessel, 2016).

In addition to the individual rawDEMs described in Table 3.1, we also used two special DEMs over DIC that were mosaicked by the TanDEM-X team at DLR using their MCP (Wessel, 2016). One mosaic was created with all rawDEMs from frozen seasons 2010-11 to 2013-14, and one only with rawDEMs from frozen season 2010-11, in which elevation values consist of a weighted average at each pixel computed from all contributing input rawDEMs. They will be referred to in this document as *TanDEM-X 2010-14 mosaic* and *TanDEM-X 2010-11 mosaic,* respectively. These mosaics are used only to provide approximate heights for separation of data in elevation bands and approximate slope calculations.

3.1.3 Data Processing

RawDEMs from the same acquisition date were mosaicked with average elevation values calculated in overlapping pixels. The rawDEM pairs or triplets from the same date were first differenced to verify internal consistency of the product and check for apparent residual height offsets and tilt from the block adjustment procedure. All differences revealed a random distribution of values centered around zero except for one acquisition. The rawDEM 1073326_3 was flagged as inconsistent with the other two rawDEMs from the same acquisition date and was rejected. A miscalculation in the HoA and subsequent error in phase unwrapping is probably the cause of this inconsistency, with Rizzoli et al. (2017a) indicating that this error occurs in 10% of the processed rawDEMs. Another rawDEM was rejected as it was completely overlapped by a larger DEM within the same frozen season (1011088_2 and 3).

The mosaicked rawDEMs from the same date, from now on referred to as *rawDEM mosaics*, were projected to coordinate system WGS84 UTM 17N and bilinearly resampled to 6 m pixel spacing, roughly corresponding to the 0.2 x 0.6 arc second pixels equivalent to the un-projected pixel size at DIC latitudes. The pixels were then aggregated with their averages to a 12 m pixel spacing, the same scale used for the TanDEM-X global DEM mosaic product. The same *snap*

raster was used in this step for all rawDEM mosaics to ensure alignment of all raster dataset in a coherent grid for the rest of the analysis. The same mosaicking and aggregating process was applied to all HEM, AMP and COH auxiliary rasters (Fig. 3.2 a and b).

3.2 Validation Elevation Datasets

Two types of data were used to validate the rawDEM elevations: (1) point elevation datasets and (2) raster optically stereo-derived DEMs, as described further in the sections below. Figure 3.3 shows the footprint of all these validation elevation datasets and their overlap with rawDEMs of DIC over the study period.

3.2.1 Point Datasets

Four point datasets were used to validate rawDEM elevations on- and off-ice: ground kinematic differential GPS surveys (dGPS), airborne IceBridge ATM laser altimetry, and airborne laser altimetry from the Subglacial Extraterrestrial Analogue Research in the Canadian High Arctic (SEARCH) project (Table 3.2).

3.2.1.1 Ground dGPS Data

Part of the ground dGPS dataset was collected specifically for this project as part of the annual Geological Survey of Canada (GSC) Mass Balance Monitoring Program on DIC in spring 2018. Five small scale dGPS transects (100 x 100 m, 5 lines at 20 m interval) were measured at the location of the five AWS on the NW basin transect (Fig. 2.4). The data was collected using an AshTech dual frequency GPS in kinematic mode mounted on a komatik sled towed by a snowmobile at approximately 7 km/h. A base station also acquired data during each transect for at least 24 hours to provide a precise static point for processing the kinematic station data. Both stations recorded every second. Data was processed using NRCAN's Precise Point Positioning service (https://webapp.geod.nrcan.gc.ca/geod/tools-outils/ppp.php?locale=en) and in the GNSS Solutions software by AshTech. The final vertical accuracy of this dataset, mainly <0.5 cm, is comparable to the vertical accuracy of the data used from other dGPS transects.

3.2.1.2 IceBridge ATM Data

IceBridge ATM data is collected by NASA Operation IceBridge to measure changes in Arctic and Antarctic ice caps, glaciers and sea ice, and is flown annually in the Arctic in the spring, typically from March through April. The 2011, 2012 and 2014 campaigns on DIC used the Airborne Topographic Mapper (ATM) scanning Lidar system mounted on the NASA P-3B aircraft at a typical altitude of 500 m above the surface and with a laser pulse rate of 5 kHz (Studinger, 2010; 2013). The IceBridge ATM data is freely available through the National Snow and Ice Data Center (https://doi.org/10.5067/19SIM5TXKPGT). We used the L1B product, which gives the geolocated surface elevation processed with the aircraft dGPS data and corrected for biases including pitch and roll. For this product, the typical point density is 1 point per 10 m^2 within a ~500 m swath. To obtain maximum data coverage, the L1B product was chosen instead of the L2B product in which returned laser pulses are re-sampled and averaged in the cross- and along-track direction giving a much smaller point density (Studinger, 2014). Point coordinates and their elevation value were extracted from the original L1B dataset format (.qi files in Version 1 for data before 2012 and .hdf5 files for Version 2) and converted to a text file format.

3.2.1.3 SEARCH Data

The SEARCH data was acquired at the end of May and beginning of June 2018 as part as of a larger airborne geophysical campaign involving the University of Texas Institute of Geophysics (UTIG) and University of Alberta to map a hypersaline subglacial lake system under DIC (Rutishauser et al., 2018). The laser altimeter is the same as that used in previous surveys in locations such as Thwaites Glacier in west Antarctica and is described in detail in Young et al. (2008). It was mounted on a Kenn Borek DC-3T aircraft flying at a typical speed of ~85 m/s and altitude above ground of ~715 m. The laser was operated at a frequency of 2000 Hz with a range resolution of 2 mm. The typical ground spot size was 1 m and the combination of pulse blocks resulted in an along-track resolution of ~20 m (Fig. 3.3).

The SEARCH data on DIC was processed to ground range elevation by Dr. Duncan Young at UTIG to correct for the laser pointing bias using the aircraft pitch and roll information. However, the accuracy of this dataset is unknown as it has not been compared to any ground-based data or higher resolution datasets. To estimate its vertical accuracy, we therefore analyzed elevation differences at cross-over points and compared elevation over stable terrain with TanDEM-X

rawDEMs. We defined cross-over points in the SEARCH data as being ≤5 m and ≤10 m apart and calculated elevation differences and statistics, reported in Table 3.3. We repeated the calculation for points on "flat terrain" only by applying a slope threshold of ≤3°. Slope was calculated from the TanDEM-X 2010-14 mosaic provided by DLR.

As variability in snow cover between years can bias the TanDEM-X elevations even over stable terrain (off-ice cap) we used only the rawDEM acquired on May 7th 2018, closest in time to the SEARCH acquisition in late May/early June 2018, for our comparison. To further reduce errors due to snow cover variability, we analyzed the evolution in snow cover on stable terrain in four Sentinel-2 images (Level-1C, 10 m resolution in true color) from May 11th, May 22nd, June 4th and June 7th 2018, covering the period between both TanDEM-X and SEARCH acquisitions (Table A.1, in appendix). We isolated the SEARCH points in areas where a mix of snow and rock was visible, indicating a thinner snow cover and/or presence of larger boulders, and excluded points in areas where only snow was visible. We retained only the points that fell within TanDEM-X pixels with a HEM ≤1 m, which removed all SEARCH points on large slopes and assured the selection of the best pixels for our comparison. With these criteria, the average difference between 190 SEARCH points and rawDEM May 7th 2018 was -3.95 m, with a standard deviation of 0.85 m (Table 3.3). The SEARCH data follows quite well the topography of the rawDEM over stable terrain but is consistently higher in elevation. A corresponding offset of -3.95 m was therefore applied to the SEARCH dataset resulting in an RMSE over the stable terrain points of 0.85 m. As this residual error is approximately three times larger than for the cross-over point analysis (0.24 to 0.30 m) it was chosen as the conservative vertical accuracy value of this dataset.

3.2.2 Raster Optically Stereo-Derived Digital Elevation Models: ArcticDEM

The ArcticDEM provides the highest resolution (2 m) DEM data available over DIC for our study period. The data and metadata are freely available through the Polar Geospatial Center (University of Minnesota; https://www.pgc.umn.edu/data/arcticdem/), who created individual DEMs using photogrammetric techniques on overlapping stereo pairs of high-resolution optical satellite images from Digital Globe's WorldView-1, 2 and 3 satellites. To preserve temporal resolution, we used individual "strip" files or DEMs, referenced to specific stereo pair acquisition times, and not the more common mosaicked product in which multiple strip files are blended. Most strip DEMs cover an area of 16-18 km by 100-120 km, which corresponds to the overlapping area

of input stereo pairs (Fig. 3.3). Data voids are often present in the strip DEMs as presence of clouds, fog and shadow can prevent the creation of terrain data. The strips are geocoded based on satellite orbital parameters from the raw images, so are created without GCPs. The absolute accuracy is stated as approximately 4 m in the horizontal and vertical directions (Porter et al., 2018). We selected all strip DEMs covering DIC during the frozen season up until the end of May, just before melt starts, in the current ArcticDEM release (Release 7, Version 3). Data was available from images acquired between 2011 and 2017.

3.3 Calculation of Elevation Bias in Raw TanDEM-X DEMs and Associated Errors

All point and raster validation elevation datasets were converted to raster format with 12 m pixel spacing (Fig. 3.2a and b). Elevation difference (dH) rasters were created for each spatial and temporal overlap of rawDEM mosaics and validation elevation dataset (Fig. 3.2d). We used the convention that the validation elevation dataset is always subtracted *from* the rawDEM mosaic. Therefore, in this document a negative elevation difference represents a TanDEM-X surface elevation that is below the "true" surface given by the validation elevation dataset. We then use the term *elevation bias* to refer to the calculated elevation differences in an absolute term. In the same fashion as the supplementary rasters of the rawDEMs, a HEM was created for each validation elevation dataset in raster format. The height error of each point dataset corresponds to the vertical accuracy reported in Table 3.2. For the ArcticDEM strips the root mean square error (RMSE) of elevation differences after co-registration (Fig. 3.2c, described in the next section) was chosen as the height error. The error term of the elevation bias (e_{dH_HEM}) was calculated with error propagation from the corresponding rawDEM mosaic HEM (e_{HEM_TX}) and the created HEM for each validation dataset (e_{HEM_val}) (Fig .3.2 d) as follows:

$$e_{dH\_HEM} = \sqrt{e_{HEM_{val}}^2 + e_{HEM_{TX}}^2} \tag{3.2}$$

This enabled us to isolate pixels where dH is significantly different from 0, where an elevation bias is present in the TanDEM-X rawDEMs. When the elevation bias is greater than its error ($|dH| > e_{dH\_HEM}$) a significant elevation difference is detected, and when the elevation bias is smaller than its error ($|dH| < e_{dH\_HEM}$) the elevation difference is considered to be not significant. Significant dH rasters were created by masking out all non-significant pixels (Fig. 3.2e).

3.3.1 ArcticDEM Strip DEM Co-registration

To compute unbiased elevation differences from DEMs they need to be co-registered, i.e., properly aligned in the horizontal and vertical dimensions. A universal co-registration methodology was developed by Nuth and Kääb (2011) for studying glacier elevation changes and is now a standard procedure to perform geodetic mass balance calculations (Zemp et al., 2013). We applied this methodology to co-register the ArcticDEM strip DEMs with the rawDEM mosaics before calculating elevation differences (Fig. 3.2e).

The co-registration methodology is a statistical framework to model errors associated with DEM differencing and is based on elevation difference over stable terrain (off-glacier). The methodology addresses three potential biases (Nuth & Kääb, 2011): (1) shifts between DEMs in the x and y directions, (2) elevation dependent bias (z direction), and (3) biases related to acquisition geometry of datasets (sensor specific).

The shifts in the x and y directions between two DEMs are solved using the relationship of elevation differences with terrain slope and aspect. The DEMs to co-register are first resampled to the same resolution and projected in the same coordinate system. A consistent mask of terrain not covered by glacier ice is also required for determination of stable terrain location in the scenes. The xy shift vector is solved iteratively over stable terrain until the improvement of the standard deviation is <2%, or if the magnitude of the shift vector is <0.5 m. The shift vector is then applied to the central coordinates of the pixels in the un-registered DEM (slave DEM). We assume that our ground control points used to resolve the xy shift were evenly distributed in the z plane, so no elevation dependent correction was further applied. The final error for elevation values in each co-registered DEM can be calculated from the residuals of elevation differences over stable terrain.

A stable terrain mask was first created from the overlap of a 500 m internal buffer to the Devon Island shoreline (from Topographic Data of Canada, CanVec, Geogratis, Natural Resources Canada, https://open.canada.ca/data/en/dataset/8ba2aa2a-7bb9-4448-b4d7-f164409fe056) and a 500 m external buffer to the 1999 ice cap margins (Burgess and Sharp, 2004). The buffers have been used to remove the effect of changing shoreline and ice cap margin location that might have occurred since the creation of these datasets. The mask was manually edited to remove all stable terrain polygons smaller than 0.5 km^2, which would include a very small number of pixels to co-register. A mosaic of Landsat 7 ETM+ images from summer 1999 (Burgess and Sharp, 2004) was

used to delineate perennial snow patches and proglacial lakes bordering the ice cap. These features were removed from the stable terrain mask after the 500 m external buffer had been applied. This coarsely created stable terrain mask is adequate for co-registration as plenty of stable terrain is identified bordering the ice cap (Fig. 3.3).

All strip ArcticDEMs that did not overlap a rawDEM mosaic from the same mass balance year over the stable terrain mask were rejected. Strip ArcticDEMs covering small areas and with lots of voids were also rejected. A Python code following the Nuth and Kääb (2011) methodology was generously provided by Dr. Robert McNabb and Dr. Chris Nuth (University of Oslo) to automate the co-registration process. Each strip ArcticDEM (slave DEM) was co-registered to each rawDEM mosaic (master DEM) that it overlapped in the same frozen season; this meant that some strip ArcticDEMs were co-registered more than once as they overlapped multiple rawDEM mosaics. Co-registration was performed only on pixels where the HEM of the rawDEM was ≤1 m and the slope of the rawDEM was >3° to remove flat terrain. A total of 17 co-registrations were performed (summary in Table 3.4, details in Table A.3 in appendix) with mean shifts of -2.62 ±2.25 m for *dx*, -0.94 ±2.47 m for *dy* and +1.52 ±1.81 m for *dz* over slopes of 3-48° and for a maximum of two iterations. The co-registration process improved the RMSE over stable terrain to an average of 0.86 ±0.29 m. Only two ArcticDEM strip-rawDEM matches had a RMSE >1 m and these were rejected from the analysis as this error is larger than that of the pixels selected for co-registration (rawDEM HEM ≤1 m). The co-registration RMSE values were taken as the height accuracy of each ArcticDEM strip–rawDEM pairs (Fig. 3.2d).

Verification of the values of the dH rasters with ArcticDEMs revealed extreme values at pixels next to void areas. Pixels are masked in the ArcticDEM strip DEMs where clouds or too low contrast to derive elevation value have been detected over the ice cap (Porter et al., 2018). It seems that this masking process is conservative, and a boundary effect occurs in the derived elevation values near voided areas. To remove the erroneous values, we determined the appropriate range of dH values by analysing the relative frequency of all dH values for pixels on ice only on all strip DEM dH rasters.

An ice mask was created from the 1999 ice cap margin shapefile (Burgess & Sharp, 2004) with a 200 m inwards buffer and areas occurring between nunataks removed as it is more likely that they have de-glaciated since 1999. We binned all the dH values into 1 m intervals and excluded

bins containing <0.5 % of the total number of pixels. This resulted by the exclusion of all values <-7 m and >1 m. Pixels with dH values outside this interval, corresponding to 0.675% of all dH pixels ($N = 7.34 \times 10^7$), were marked as erroneous and set to no data in the dH rasters.

3.4 Potential Variability in TanDEM-X Derived Elevation During the Frozen Season

The SAR scenes used to create the TanDEM-X rawDEMs over DIC were acquired throughout the fall and winter, when we can assume that no melt is occurring on the ice cap surface (Mortimer et al, 2016). All validation elevation datasets described in Section 3.2 are from early spring, just before the start of the ablation season. Therefore, an underlying assumption in comparing these datasets is that no significant change occurs on the ice cap surface from fall to spring that could generate variations in interferometrically derived elevation values in the TanDEM-X DEMs. We use two specific datasets to verify this assumption: (1) SAR scenes acquired during the frozen season to investigate the temporal stability of backscatter on DIC, and (2) relative surface height from AWS stations on DIC to investigate variability in snow depth. Processing of both these datasets is described below.

3.4.1 Wide ScanSAR TerraSAR-X and TanDEM-X Scenes

A variation in backscatter during the frozen season would influence the determination of the depth of the surface return and therefore the derived elevations in TanDEM-X rawDEMs over the ice cap surface during the same period. Evolution of backscatter on glaciers is often used to study snow facies and duration of the melt season (e.g., Wolken et al., 2009; Casey & Kelly, 2010; De Jong, 2013; Rizzoli et al., 2017b), but evolution of backscatter during the frozen season has rarely been reported as it is typically assumed to vary insignificantly (e.g., Gray et al., 2017). However, as our study is concerned with validation of the TanDEM-X DEMs, we judged it important to investigate whether this assumption is valid for X-band SAR data.

We used 14 Wide ScanSAR TerraSAR-X and TanDEM-X scenes (6 beams) acquired with the same orbital parameters (Table 3.5). The scenes were provided by Achim Roth (German Remote Sensing Data Center, DLR) through the proposal COA1736. Each scene covered almost the entire ice cap, measuring 200 km along-track and 240 km across-track. We obtained one image approximately every month from October to May, covering two consecutive frozen seasons (2017-

18 and 2018-19), as well as one image during the melt season in June 2018. We used the Enhanced Ellipsoid Corrected (EEC) product, which is already geocoded, resampled and projected to the WGS84 reference ellipsoid using a reference DEM to correct for terrain distortions (Fritz & Eineder, 2013). The reference DEM used for the EEC product over DIC to project our scenes is the GLOBE (Global Land One-km Base Elevation) DEM (Hastings & Dunbar, 1998), which has variable vertical accuracy of 10-100 m and a 30 arc seconds grid size (Fritz & Eineder, 2013). This is not the best available DEM for this region due to the low vertical accuracy and resolution but was judged to be appropriate to correct for terrain distortions as most of the scene is dominated by the ice cap which has a gently sloping surface. The EEC product is complemented by a Geocoded Incidence Map (GIM) containing information about the local incidence angle for each pixel of a scene derived from the DEM projection.

3.4.1.1 Radiometric Calibration and Filtering

We first performed a radiometric calibration of each scene from radar brightness β^0 values (relating to unit areas in slant range) to normalized backscatter σ^0 (relating to units area on the surface) to account for variations in backscatter due to the incidence angle and to reduce topographic effects (Fritz & Eineder, 2013). The radar brightness values β^0 (in dB) can be calculated from the EEC raw product pixel values in DN using the calibration factor k_s using:

$$\beta^0_{dB} = 10 \log_{10}(k_s \cdot |DN^2|) \tag{3.3}$$

The local incidence angle is extracted from the GIM with:

$$\theta_{loc} = \frac{GIM - (GIM \; mod \; 10)}{100} \tag{3.4}$$

The ground backscatter σ^0 (in dB) for each pixel can then be derived using the local incidence angle θ_{loc} with:

$$\sigma^0_{dB} = \beta^0_{dB} + 10 \cdot \log_{10}(\sin(\theta_{loc})) \tag{3.5}$$

We converted the σ^0 raster to 45 m pixel spacing using a 3x3 average filter to produce pixels larger than the resolution of the original product (40 m, Table 3.5). A 5x5 rectangle median filter was then applied to further reduce speckle in the data.

3.4.1.2 Determination of Radiometric Resolution

Our interest is in the temporal variability of backscatter over the ice cap which requires knowledge of the radiometric resolution (RR), i.e., the precision of the backscatter value in dB for a scene. If multiple Wide ScanSAR scenes were acquired in the same geometry, at the same time and processed in the same way, the calculated backscatter value for a given pixel would not be exactly the same in all these scenes. The RR is thus a measure of this residual variation in backscatter value per pixel. Knowledge of this parameter is necessary to determine the smallest significant change in backscatter that can be detected between two scenes acquired at different times. Defining ScanSAR RR is more complex than for other radar modes due to the combination of multiple beams. It is not specified for Wide ScanSAR (6 beams) in the product documentation but is mentioned to be "*similar to"* the 0.6 dB long-term absolute accuracy of the TerraSAR-X stripmap product (Fritz & Eineder, 2013).

To mitigate speckle in SAR data, *multilooking* is often performed. This process is defined as a non-coherent averaging of L independent measurements of the intensity image and results in the improvement of radiometric accuracy at each pixel, at the expense of reduced resolution (Olivier & Quegan, 2004). All L independent measurements provide an independent "Look" of the data at each position. For the TerraSAR-X six beam wide ScanSAR, multilooking parameters are different for each beam to achieve a consistent ground range resolution between 30 and 40 m. The number of range looks varies between 6 to 8 from beam to beam (Fritz & Eineder, 2013).

Radiometric resolution depends on the number of looks performed in the processing of the SAR data. Each post-processing step (geocoding, resampling, filtering, etc.) modifies the original number of independent looks at each pixel and alters radiometric resolution. It is then the "Equivalent Number of Looks" (ENL), number of looks after post-processing, that must be used to determine RR. As it is not straight-forward to estimate the ENL from the known system parameters, Olivier and Vidal (1994) presented a way to perform an *a posteriori* estimation with the actual data ready for analysis using the contrast ratio σ/μ. This measure of texture represents the spread of speckle and is defined as the ratio of standard deviation (σ) to mean intensity (μ) over a statistically uniform region. The radiometric resolution of a post-processed scene, denoted by γ, can be estimated from a homogenous group of pixels using:

$$\gamma_{dB} = 10\log_{10}\left(1 + \frac{1}{\sqrt{ENL}}\right) = 10\log_{10}\left(1 + \frac{\sigma}{\mu}\right) \quad (3.6)$$

To choose a homogenous area over DIC we first calculated the standard deviation and the mean intensity at each pixel for a 11 x 11 window and then calculated the contrast ratio for each scene. We selected a large rectangle area (~488 km^2) in the center of the ice cap, where the RR was most homogeneous within all scenes. To be conservative, we chose the maximum RR value that occurred within this homogenous area as our final RR. With error propagation, a significant change in backscatter ($\Delta\sigma^0$) will only be detectable between two scenes if the difference is greater than its error (e_{σ^0}) calculated as:

$$e_{\sigma^0} = \sqrt{\gamma_{dB}^2 + \gamma_{dB}^2} \quad (3.7)$$

3.4.2 Snowpack Depth: Automatic Weather Station Data

Snow accumulation patterns and rates have been reported for DIC (e.g., Koerner, 1966; Colgan & Sharp, 2008; Sylvestre et al., 2013) but variability in snow depth (not converted to water equivalent) has not been previously reported. Knowing the importance of katabatic winds for snow redistribution on the ice cap (Koerner, 1966; Mair et al., 2005), we hypothesized that snowpack depth was the most important factor affecting surface elevation during the frozen season. We therefore used field data to determine the variability in snowpack height between November and May inclusively, corresponding to the interval of the rawDEM acquisitions. We used the relative surface height change data available since 2010 for the five AWS in the NW basin of DIC (Fig. 2.4). The data was acquired hourly using a high-accuracy (±1 cm) sonic ranger (Campbell Scientific SR50A) to aid in the interpretation of the in-situ mass balance data (Burgess, 2017). The complete dataset was provided in Excel file format by Dr. David Burgess (GSC).

We used the temperature corrected distance as the measurement of relative surface height. This correction is automatically applied on the distance data using the temperature data recorded hourly at each station using a Campbell Scientific 44212 temperature probe (±0.1°C, up to -50°C) (Burgess, 2017). Following the specification of the SR50 instrument (Campbell Scientific, 2019; https://www.campbellsci.ca/sr50a), we removed all values below the minimum recording distance of the instrument (0.5 m), and when air temperature was below -45°C. Large shifts in the data are visible when the height of the instrument was changed in late April-May during field visits in some

years. To calculate a continuous record of surface height change including these periods, we therefore adjusted the values by equalizing the first relative surface height value and all subsequent ones to the last value before each shift. Only frozen season data with valid values within a 24-hour period around the shift were kept after this adjustment. The datasets were then averaged daily to smooth and remove outliers. Statistics of all values between the November-May inclusive intervals were then calculated for periods with >75% valid data at all five weather stations.

3.5 In-Situ Mass Balance Time Series: Proxy for Summer Conditions and Estimation of the Equilibrium Line Altitude

The in-situ mass balance time series complements the analysis of the elevation bias in the TanDEM-X rawDEMs by providing information on the evolution of: (1) the net NW basin balance, which is a proxy for summer conditions as it is most affected by the intensity and duration of summer melt (Koerner, 2005), and (2) the ELA, which provides a good estimation of the location of the boundary between the accumulation and ablation zone for the NW basin. As the current glaciological mass balance reported by the GSC uses outdated basin area and a low accuracy elevation model for the hypsometry, we updated the in-situ mass balance time series with better basin geometry and hypsometry data to improve the accuracy of the ELA estimations.

The in-situ mass balance transect on the NW basin of DIC covers the elevation range ~100-1900 m a.s.l., from the terminus of Sverdrup Glacier to the ice cap summit. A second arm descends to the western margin from ~1300 to ~400 m a.s.l. (Fig. 2.4). The annual mass balance is derived following the stratigraphic system from the detection of two successive summer surfaces in the field (Cogley et al., 2011). The detected summer surface corresponds to the annual minima at each stake location at the end of the ablation season. Then the mass balance year starts at the end of the melt season in September; e.g., the mass balance year 2017 is from September 2017 to end of August 2018.

During fieldwork in late April or early May the height above the ice or firn of each stake is measured, as well as snowpack depth and bulk density. Combined with the AWS relative surface height measurements, the winter and summer balances at each stake can then be calculated. The surface type (firn, icy firn, superimposed ice and ice) is assessed at each stake to use the appropriate density for height to mass change conversion. A third order polynomial is then fitted to the net

balances (winter + summer) of the stake network as a function of elevation and fitted values are extracted for each 100 m elevation band (Fig. 3.4). Using a third order polynomial fit best reflects the different slopes in mass balance gradients above and below the ELA, which typically get steeper at lower elevations (Thomson et al., 2016). The average basin-wide balance from the fitted net balance values are calculated with the area-elevation distribution of each 100 m band across the basin. From this methodology, the ELA and the accumulation area ratio (AAR) can also be calculated yearly.

The initial basin delineation was determined by Dr. Roy Koerner (GSC) at the start of the mass balance program in 1960 and has been kept for consistency in reporting mass balance data, even though it does not properly represent the ice divide between the bordering basins. The DEM used for hypsometry is the Canadian Digital Elevation model (CDEM), which is based on topographic maps (at 1:50,000 and 1:250,000 scales) created from aerial photography campaigns in the Arctic in 1959-60 (at 1:60,000 scale). Its vertical accuracy is quite low with reported errors of ±20 m over bedrock, ±50 m along outlet glaciers and ±100 m in the ice cap interior due to limited bedrock control points, photogrammetric data capture over low contrast regions, and conversion of data from analog to digital formats (Burgess & Sharp, 2008).

The basin ice divides were updated with basin outlines derived from ice flow patterns from Van Wychen et al. (2012). Ice cap margins and shapefiles of nunatak outlines from 1960 and 1999 were available from the Burgess and Sharp (2004) study on area change of the ice cap (Table 3.6). We extended this series to 2010 by digitizing the NW basin margin on Landsat 7 ETM+ summer scenes. A total of 6 scenes from late July to early June 2010 were used to obtain full coverage of the margin and remove data gaps caused by presence of clouds and by the failure of the scan line corrector in Landsat 7 ETM+ (Table A.2 in Appendix). The color bands were pan-sharpened with the panchromatic band in ENVI Software (V5.0, Harris Geospatial Solutions) to delineate the glacier outline at the highest resolution of 15 m. Images were displayed in a false color composite (bands 7-4-2 in RGB channels) to easily differentiate between ice and rock. Following Hall et al. (2003), the line placement error was determined as:

$$d = \sqrt{r^2 + r^2} \tag{3.8}$$

where r is the cell size of the image. The error of the basin area can then be calculated as:

$$a = A \cdot \left(\frac{2d}{x}\right) \tag{3.9}$$

where A is the area and $A = x^2$, and x is the linear side dimension (same as the cell size). For our delineation of the 2010 basin area, d = 21.1 m and a = 0.00636 km^2 which corresponds to less than 0.01 % error over the total basin area of 1808 km^2. To determine the error in the area due to inconsistent digitizing by the analyst, a snow patch (5.4 km^2) was digitized five times at the same resolution to calculate the percent area change (White & Copland, 2015). This exercise gave on average a 1.06% area error. Half of this error was kept as the final area error reported in Table 3.6 because only half of the total basin is manually delineated (fixed ice divides) and because it is larger than a.

The area of each 100 m elevation band was calculated using the basin hypsometry from the TanDEM-X 2010-11 mosaic supplied by DLR. We produced three basin area-elevation distributions for each of the three basin delineations. We assume that these distributions can still be used for years prior to 2010, justified by the fact that the basin mass balance only serves as context to interpret elevation biases in TanDEM-X rawDEMs. We are confident that the use of the TanDEM-X mosaic DEM improves the overall accuracy of the time series considering the large elevation biases of the originally used CDEM.

We recalculated the mean basin mass balance, cumulative thickness change, ELA and AAR from the original compiled mass balances measured in cm w.e. at each stake from 1960 to 2015 provided by Dr. David Burgess (GSC). The coefficient of determination (R^2) of the third order polynomial fit was >85% except for two years (1995 and 1975), but the third order polynomial fit was still judged better than a linear fit for the two cases. The ELA was extracted on the polynomial curve where the thickness change was equal to 0 (Fig. 3.4). A fit could not be calculated for four of the years (1962, 1966, 1967 and 1969) because the minimum number of data points required to fit a third-order polynomial (4 points) was not met or because the data did not reasonably cover the entire elevation range of the basin (e.g., all points in the ablation area). For these years, we used the mass balance value and ELA value modelled by Dr. Roy Koerner (GSC), which were based on analysis of the spatial correlation between poles measured in previous years (unpublished data). The mean basin mass balance was then calculated for each year as the weighted average of the mass balance at each 100 m elevation band according to the relevant area-elevation

distribution: 1960 distribution used for the 1960-1998 period, 1999 distribution for 1999-2009, and 2010 distribution for 2010-2015.

3.6 Influence of Near Surface Stratigraphy and Density: Comparison with Subsurface Datasets

3.6.1 Shallow Firn Cores

To aid in the interpretation of potential elevation bias at the location of our five dGPS transects, we also collected three shallow firn cores at all sites during the spring 2018 field season on DIC. A Kovacs corer (9 cm diameter x 1.2 m long) was used at the three upper dGPS transect sites (DV1H, DV3F and DV7D) (Fig. 2.4) to collect a core until a thick ice layer was observed at the bottom (~250 cm cored at each site). Core stratigraphy was visually logged in the field and firn types and ice layers were qualitatively recognized based on air bubble content. Bulk density was measured by grouping naturally broken core pieces with a nylon bag and hand scale. We estimate the error on our density measurements to be ±20% by combining the errors from measurements with the scale (±0.05 kg) and with the ruler for the length of the core sections (±0.5 cm). Snow pit stratigraphy and average snow depth at the corresponding AWS of each dGPS transect were also recorded.

3.6.2 Ground Penetrating Radar Profiles

Ground penetrating radar (GPR) is often used to study subsurface properties of glaciers over large areas, notably to locate snow facies boundaries and ice thicknesses. The difference in dielectric constant between snow and ice, reflecting the speed at which the radar wave travels through a medium, enables the detection of their layering below the surface. Depth and thickness of major layers can be determined from the appearance of clear internal reflecting horizons at the interface between ice and firn. These typically reflect a significant change in density from firn (heterogeneous ice and air bubbles) to ice (more homogenous, less air bubbles), and vice versa (Gascon et al., 2013; Sylvestre et al., 2013).

Overlap of rawDEMs and validation elevation datasets with two GPR profiles collected in spring 2011 on DIC enables us to compare our calculated elevation bias with subsurface properties. Gascon et al. (2013) used a 500 MHz GPR system to survey a 40 km transect along the CryoSat

line from Site 1 (~1800 m a.s.l.) to Site 3 (~1000 m a.s.l.) covering the major facies of the ice cap on the SW basin (Fig. 2.4). De Jong (2013) used a 450 MHz GPR system to survey a 25 km transect along the in-situ mass balance transect on the NW basin from the CryoSat line Site 1 (~1800 m a.s.l.) to mass balance stake DV12, above the DICS AWS (~1340 m a.s.l.) (Fig. 2.4.). Data in both studies was processed in a similar way and average radar wave velocities (0.20 m ns^{-1} in De Jong (2013) and 0.23 m ns^{-1} in Gascon et al. (2013)), used to convert data from the time domain to the distance domain, were determined from average firn core density data acquired during the surveys.

We use published figures of radar profiles from Gascon et al. (2013) and De Jong (2013) to compare to our calculated elevation differences. As we did not have the exact GPR transect locations (only start and end points), we assume that they are within ± 100 m of the 2011 dGPS tracks used for validation as both transects followed the same GPS points to navigate. In addition, it was shown in Gascon et al. (2013) that the horizontal spatial variability in the position and thickness of ice layers seen in the GPR profile was negligible within 100-200 m of the GPR transect. Hence, we are confident that the GPR profiles represent the subsurface conditions of our calculated elevation differences. The elevation bias values from overlapping dH rasters in mass balance year 2010-11 were extracted at a 12 m interval along the GPR transect lines.

Table 3.1 Details of TanDEM-X rawDEMs and associated metadata used in this study. Underlined and in italics are acquisitions that were rejected from the analysis. Vertical and horizontal (not shown) displacement from the block adjustment procedure have been applied before the analysis, except for the vertical adjustment of 1512481_2 and 3 and the horizontal adjustment of ~4 m for 1106088_1 and 2, corresponding to a 1-pixel shift.

Frozen Season	Acquisition ID	Date (dd/mm/yyyy)	Raw DEM ID	Block Adjustment Vertical Displacement (m)	Height of Ambiguity (m)	Perpendicular Baseline (m)	Equator Crossing Direction	Incidence Angle Range (near - far) (°)
2010-11	1009244	12/12/2010	2	-0.455	46.45	146.30	Ascending	39.32 - 42.09
			3		46.86	145.03		
			4		47.26	143.65		
	1009588	23/12/2010	3	0.167	45.93	137.35	Ascending	37.13 - 39.86
	1011088	*10/02/2011*	*2*	*0.763*	*53.17*	*136.67*	*Ascending*	*41.49 - 43.85*
			3		*53.58*	*135.70*		
	1013058	21/03/2011	2	3.288	58.24	123.91	Ascending	41.11 - 43.52
			3		58.78	122.78		
	1023146	07/04/2011	1	-1.751	55.69	113.21	Ascending	37.06 - 39.89
	1023147	07/04/2011	2	4.816	54.59	115.26	Ascending	37.06 - 39.89
2011-12	1055856	24/03/2012	2	-2.759	85.26	80.54	Ascending	39.26 - 42.00
			3		85.54	80.35		
	1073326	15/04/2012	2	2.268	33.85	191.48	Ascending	37.96 - 40.68
			3		*34.11*	*190.02*		
			4		34.39	188.49		
2012-13	1107811	04/11/2012	2	0.962	37.08	187.49	Ascending	40.19 - 42.77
			3		37.27	186.52		
			4		37.48	185.47		
	1107810	15/11/2012	3	2.300	42.08	154.04	Ascending	38.05 - 40.72
			4		42.32	153.08		
	1106088	13/12/2012	1	4.475	45.95	136.66	Ascending	37.22 - 39.74
			2		46.08	136.18		
2013-14	1169772	13/12/2013	1	0.174	83.93	81.27	Descending	39.31 - 42.02
			2		83.72	81.42		
	1171318	04/01/2014	13	1.337	69.43	94.01	Descending	37.95 - 40.76
			14		69.10	94.43		
	1171718	10/01/2014	12	1.350	73.27	95.87	Descending	40.19 - 42.77
			13		72.92	96.25		
2017-18	1512481	07/05/2018	2	0.120	66.27	102.52	Descending	39.27 - 42.02
			3		65.70	103.52		

Table 3.2 Description of datasets used for elevation validation, their vertical accuracy, and associated references. Extent and overlap of these datasets is shown in Figure 3.3.

Dataset	Description		Time period	Resolution/ Spacing	Vertical Accuracy	Reference
IceBridge ATM L1B Version 1 and 2	Airborne laser altimetry point datasets for specific flight lines across Devon Ice Cap		early spring 2011, 2012, 2014	Average point density: 1 point per 10 m^2 Average swath width: 400 m	0.15 m RMSE error for cross-over points, 719 points, <1 m apart, from 2005-2013 data over Penny Ice Cap from Schaffer (2017)	Studinger (2010), Studinger (2013)
Kinematic dGPS Surveys	Differential GPS ground transects, processed using Precise Point Positioning (PPP) method (NRCAN)	summit grid (6 x 45 km) and IceBridge ATM flight lines	early spring 2011	Point spacing: ± 11 m	Typically <0.5 m Height error per point from PPP processing	Gray et al. (2015)
		5 transects of 100 x 100 m along mass balance transect on NW basin	early spring 2018	Point spacing: ± 2 m		Dataset acquired during Spring 2018 fieldwork for this project
Subglacial Extraterrestrial Analogue Research in the Canadian High Arctic (SEARCH) Laser Altimetry	Airborne laser altimetry survey as part of the SEARCH Arctic geophysical campaign over Devon Ice Cap: 5 x 5 km grid covering most of the ice cap dome, with sections at 2.5 x 2.5 km spacing		spring 2018	Along track resolution: ±20 m Typical ground spot size: 1 m wide	0.85 m RMSE over stable terrain after comparison with rawDEM mosaic 07-05-2018 (Section 3.2.1.1)	Data: personal communication, Dr. Anja Rutishauser, University of Texas Institute for Geophysics Altimeter set-up: Young et al. (2008)

Table 3.3 Accuracy assessment of the 2018 SEARCH laser altimetry point dataset on Devon Ice Cap based on analysis of cross-over points and stable terrain analysis with rawDEM 07/05/2018.

	Cross-over points				Difference with stable terrain (HEM ≤ 1m)	
	≤ 10 m	**≤10 m, slope ≤3°**	**≤ 5 m**	**≤5 m, slope ≤3°**	**Before shift**	**After shift**
N	91	57	15	10	190	190
Min. (m)	0.001	0.001	0.023	0.023	-6.82	-2.26
Max. (m)	0.831	0.686	0.464	0.464	-1.69	2.87
Mean (m)	0.234	0.215	0.188	0.209	-3.95	0.000
Median (m)	0.212	0.185	0.126	0.165	-3.91	-0.040
SD (m)	0.184	0.160	0.149	0.172	0.853	0.853
RMSE (m)	0.297	0.266	0.238	0.268	4.04	0.851

Table 3.4 Summary of applied shifts and co-registration statistics for ArcticDEM strip DEMs (N = 17).

	Applied shifts (m)			Elevation differences (m)				Area (km^2)
	dx	dy	dz	Mean	Median	SD	RMSE	
Min.	-7.83	-5.68	-1.64	-0.06	-0.01	0.62	0.62	1.42
Mean	-2.72	-1.11	1.50	-0.02	0.01	0.86	0.86	15.05
Max.	-0.26	3.56	4.30	0.01	0.02	1.75	1.75	75.78
SD	2.20	2.53	1.80	0.02	0.01	0.28	0.29	18.53

Table 3.5 Specifications of the TerraSAR-X/TanDEM-X Wide ScanSAR (6 beams) scenes used in this study. All scenes are right looking, descending passes from orbit 113 with incidence angles ranging from 22 to 43° acquired in single HH polarization. Pixel spacing of 15 m and resolution of 40 m.

Period	Date	Orbit cycle
Fall 2017 – Spring 2018	2017-10-09	343
	2017-12-14	349
	2018-01-16	352
	2018-02-18	355
	2018-03-23	358
	2018-04-25	361
Summer 2018	2018-06-30	367
Fall 2018 – Spring 2019	2018-10-07	376
	2018-11-09	379
	2018-12-23	383
	2019-01-25	386
	2019-02-27	389
	2019-04-01	392
	2019-05-04	395

Table 3.6 Devon Ice Cap geometry vector datasets used to update the in-situ mass balance time series and to create masks to isolate stable terrain and on-ice cap pixels (Section 3.3.1).

Dataset Name	Time Validity	Description, Coverage and Reference	Reported Accuracy
Area polygons (including nunataks delineation)	1959-1960	Entire ice cap outline polygon delineated from air photos of 1:60,000 (Burgess and Sharp, 2004)	Line placement: ±75 m Area: ±40 km^2
	1999	Entire ice cap outline polygon delineated from Landsat 7 ETM+ satellite images (Burgess and Sharp, 2004)	Line placement: ±120 m For area: ±31 km^2
	2010	NW basin only: created in this study from Landsat 7 ETM+ satellite images (listed in Table A.2, in appendix)	Line placement: ± 21 m For area: ±8 km^2
Drainage divides	Still valid as of 2017 (Van Wychen et al., 2017)	Basins delineated from Landsat 7 ETM+ satellite images from 1999-2000, Canadian Digital Elevation Model (Burgess & Sharp, 2004), and updated with bed topography (Dowdeswell et al., 2004) and InSAR derived flow directions (Burgess et al., 2005; Van Wychen et al., 2012)	Absolute accuracy (before updates) is ±15 m (Burgess & Sharp, 2004)

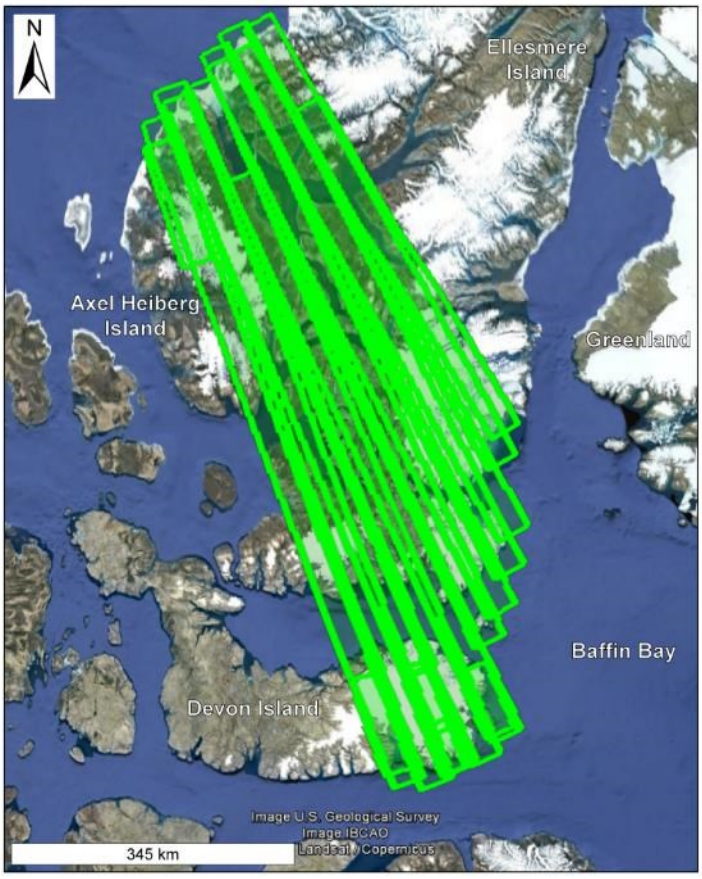

Figure 3.1 Block adjustment areas (green rectangles) used for the first acquisitions of rawDEMs over Devon Ice Cap. Provided by Dr. Birgit Wessel (German Remote Sensing Center, DLR), Google Earth image screenshot.

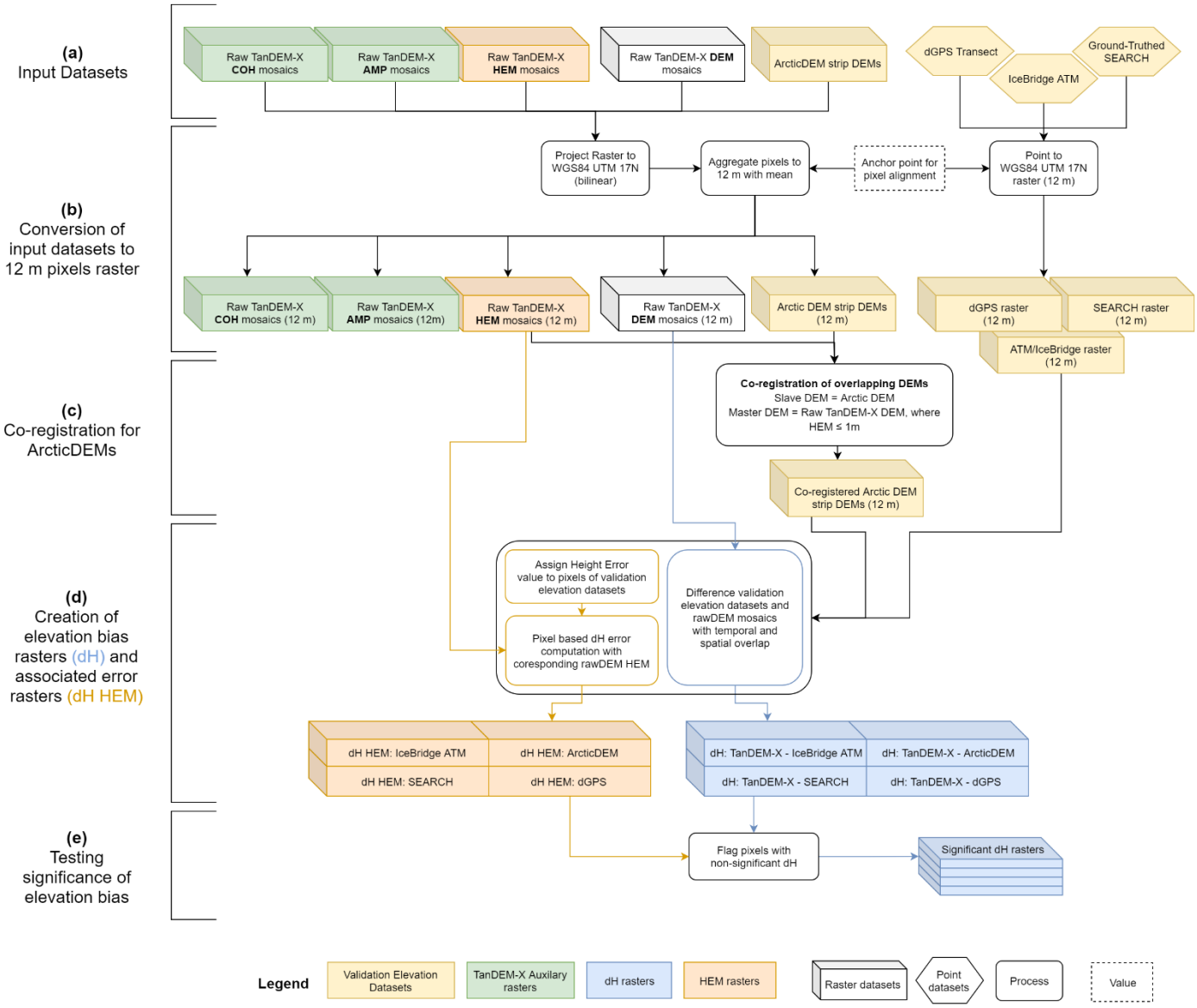

Figure 3.2 Flow chart showing the methodology used to create elevation difference (dH) rasters and height error map (HEM) rasters from rawDEM mosaics and validation elevation datasets. Includes processing of TanDEM-X auxiliary raster of coherence (COH) and amplitude (AMP).

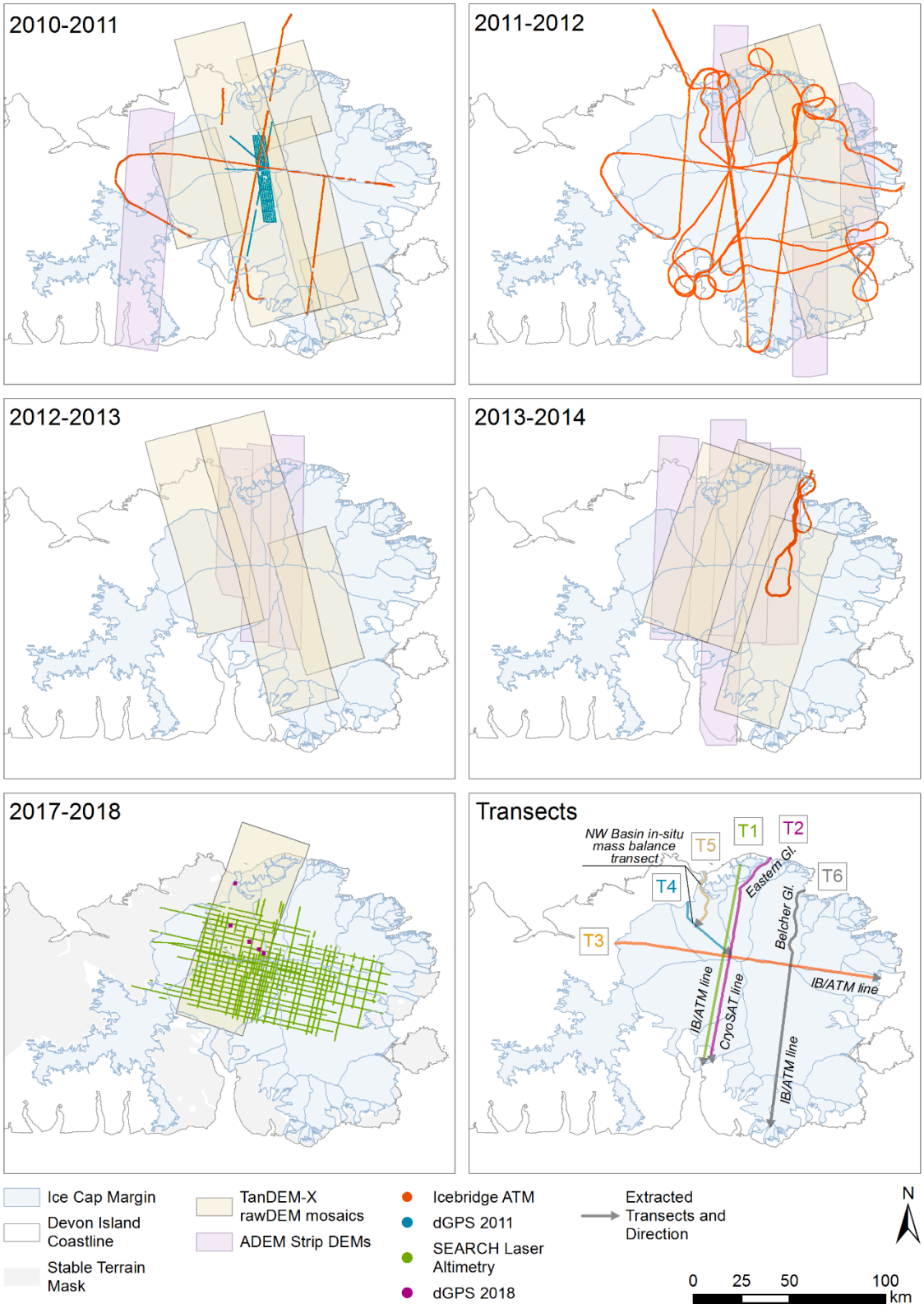

Figure 3.3 Footprint of TanDEM-X rawDEM mosaics and elevation validation datasets over Devon Ice Cap for each frozen season except for the bottom right panel, where the six selected transects to extract elevation differences between TanDEM-X rawDEMs and validation elevation datasets are shown. Stable terrain mask shown for 2017-18 only, but valid for all years.

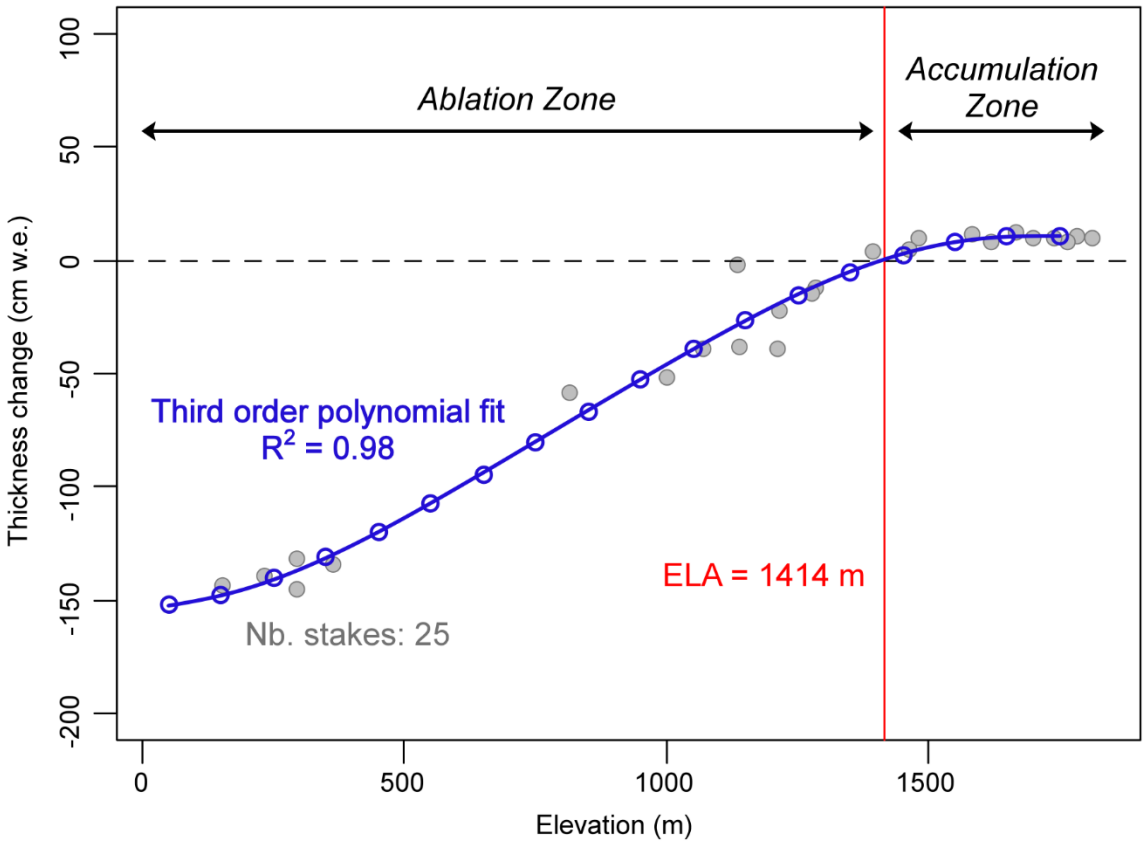

Figure 3.4 Example of the determination of the in-situ mass balance for the Northwest basin of DIC (thickness change in cm w.e.) at each 100 m elevation band from a third order polynomial fit to mass balance stake measurements and extraction of the equilibrium line altitude (ELA). Data presented for mass balance year 2006-07, when 25 mass balance stake measurements were made.

Chapter 4: Results

In this chapter we present the information required to evaluate the elevation bias of TanDEM-X rawDEMs on DIC. We start by presenting the estimated variability in DIC surface height that occurs from fall to spring that could influence the calculation of elevation differences between the rawDEMs and the validation elevation datasets from different acquisition times. We then present the updated in-situ mass balance time series including the modelled ELA in the NW basin. This is followed by elevation differences over stable terrain. Lastly, elevation differences over the ice cap surface are presented, including their relationship with SAR acquisition parameters, their spatiotemporal variability and their comparison with subsurface datasets.

4.1 Potential Variability in TanDEM-X Derived Elevation During the Frozen Season

In order to compare TanDEM-X rawDEM elevations acquired in the fall and winter (as early as November and up to May) with validation elevation datasets typically acquired in the spring (April to early June), we start by considering potential influences on interferometrically derived elevations on the ice cap during the frozen season. Three components can influence real and perceived elevation at any point on the ice cap during this season: (1) variation in backscatter, (2) variation in snowpack depth, and (3) background dynamic elevation changes. We first present results for components (1) and (2) based on our analyzes of the Wide ScanSAR scenes and of the relative surface height change measured with a sonic ranger at the AWS. We then combine these results with estimates of dynamic elevation changes from the literature to evaluate potential height bias due to different rawDEM acquisition times.

4.1.1 Backscatter Variability in Wide ScanSAR Scenes

For the 14 Wide ScanSAR scenes analyzed, the radiometric resolution γ_{dB} is mostly <1 dB within the ice cap interior on low slopes, with higher values up to ~10 dB on bedrock and steep valley sides (Fig. 4.1a). Slightly more variability is seen within the selected homogenous area (Fig. 4.1a) to calculate γ_{dB} in the 2018-19 scenes (Fig. 4.1b and c). The scene closest to the melt season (2019/05/04), and within the melt season (2018/06/30), had noticeably low radiometric resolution, i.e., higher precision. This reflects generally homogeneous backscatter during this period when the snowpack is metamorphosing with increasingly warmer temperatures for the first case, and when

the surface is wet during melting in the second case. The final radiometric resolution was taken as the most conservative value in both frozen seasons within the homogenous area: $\gamma_{dB} = 0.84\ dB$ (Fig. 4.1b and c). Hence, a significant change in backscatter could only be detected between two scenes if the difference was more than their combined error: $e_{\sigma^0} = 1.19\ dB$ (Eq. 3.7).

Looking at the range in backscatter values within both frozen seasons, approximately 85% of the pixels vary by <3.5 dB on the ice cap (Fig. 4.2). A few pixels have values above 6 dB and occur only on nunataks, valley sides or at glacier termini. A clear spatial pattern emerges in Fig. 4.2 when setting all pixels below our change detection limit of 1.19 dB to the same color. Nearly horizontal (±4 km) and vertical (±200 m) stripes appear. These patterns are due to the acquisition process of Wide ScanSAR scenes, where 6 ground subswaths are scanned quasi-simultaneously and processed into one scene (Fritz & Eineder, 2013). The overlap of these subswaths results in the acquisition of more data, thus improving the radiometric resolution (mostly <0.5 dB) and increasing the number of pixels where change is undetectable.

To easily detect areas where changing backscatter is occurring, we subtracted the mean backscatter value of the current frozen season from each scene (Fig. 4.3a). The variability in backscatter is within ±3 dB for both years and a general trend is visible as the winter progresses. Backscatter is typically lower than the mean from October-December, increases above the mean during the coldest months of January-March, and lowers towards the start of the spring in April-May. There is a much larger decrease in backscatter (up to -30 dB) in the only scene we analyzed when melt was occurring (30/06/2019, Fig. 4.3b). The pattern in winter variability is similar in both frozen seasons even if the mean backscatter values are different: higher in 2018-19 on the outskirts of the ice cap and lower in the ice cap center (Fig. 4.3c).

To investigate any potential relationship between backscatter and elevation, we extracted the mean and standard deviation of backscatter on ice-covered areas only in all scenes at 100 m elevation band intervals. There is a clear positive relationship between backscatter and elevation in all scenes, with no outliers appearing (Fig. 4.4). This positive correlation can be explained by the general similarity in subsurface properties with elevation within respective glacier facies zones. As mentioned in Section 2.2.1, backscatter is highest in the percolation zone where most volume scattering occurs, and decreases with reducing elevation as the glacier surface below the snowpack transitions from firn to glacier ice (Casey & Kelly, 2010). The decrease in the standard deviation

of backscatter values towards higher elevations can be explained by the decrease in glacier surface roughness and increase in homogeneity of the subsurface, which creates less spatial variability in backscatter. A clear difference in mean backscatter is visible between the two frozen seasons (Fig. 4.4b) but mean backscatter values per elevation band are all within one standard deviation of each other. The larger variability in mean backscatter for the 0-100 m elevation band (Fig. 4.4a) is likely due to the inclusion of sea ice, open water or bedrock pixels from inaccuracies of the ice mask near glacier termini. Mean backscatter of the entire ice cap during the frozen season is -4.14 dB for 2017-18 and -3.34 dB for 2018-19, with ranges below 0.5 dB: 0.297 dB and 0.460 dB for 2017-18 and 2018-19, respectively.

4.1.2 Snowpack Depth Variability from Automatic Weather Station Data

Relative surface height change from November to May could only be extracted from ~50% of the AWS station records over the periods 2010-11 to 2017-18 due to missing data, removal of outliers, and installation of all stations in 2011-12 except DICS and DV1H (Fig. 4.5). No stations had valid data for >75% of the days in 2017-18 because long intervals with values of zero were recorded. These values indicate that the snow surface was at the sensor or above it but does not inform us of relative surface height change and for this reason were judged invalid. Even with this dataset, it is clear that most annual accumulation occurred from August to October with an increase in relative surface height of ~30 to 40 cm at all stations over this period, followed by a relatively stable height until the start of melt in June. In this dataset we are also able to see when surface lowering occurs at the start of the melt season, which is on average during the last week of May for DVSVW and in the first half of June at the other weather stations. This timing is the same as what has been reported previously by Wang et al. (2005) and Casey and Kelly (2010). Over 2010-11 to 2017-18, the three upper stations (DV1H, DV3F and DV7D) gained a total of ~1-2 m in relative elevation. Station DICS was stable and DVSVW on Sverdrup Glacier lost ~4-5 m in relative elevation.

Distributions of the relative surface height for all stations and years are shown in Figure 4.5, where the mean values have been set to zero for comparison. No clear pattern is visible of higher or lower ranges between the years across all the AWS. Most distributions are bimodal or heavily skewed towards the lower values (small changes in relative surface height), which is represented in Figure 4.5 by minimum values being close to one standard deviation below the mean in most

cases. Stations DV3F and DV7D stand out in frozen season 2015-2016, with ranges of 39.6 cm and 30.8 cm respectively, with most values between 20 to 30 cm but some instances below 1 cm. For all stations and years combined, the mean range is 21.2 cm and below 29.5 cm for 90% of the cases. The mean standard deviation is 4.6 cm and below 7.9 cm for 90% of the cases. We judge that with our data manipulations these values are only precise to the nearest centimeter. We then estimate that the typical range of variability in snowpack depth on the ice cap from November to May, corresponding to the maximum separation between a rawDEM and validation elevation datasets acquisitions, lies between the rounded mean standard deviation of 5 cm and the rounded mean range of 21 cm.

4.1.3 Combination with Dynamic Elevation Change Estimates

Dynamic elevation changes refer to thinning and thickening of the ice cap surface, typically due to the redistribution of mass from the accumulation zone to the ablation zone along a glacier profile. Submergence, or net vertical downward motion, occurs in the accumulation zone due to firn compaction and the vertical component of ice flow (normal strain) as new snow buries old firn below. In the ablation zone there is emergence, or net vertical upward motion, due to the vertical component of ice flow as ice removed by surface melt is replaced by ice flowing in from higher elevations (Cuffey & Paterson, 2010). The processes of submergence and emergence dynamically impact the elevation of a glacier continuously over time.

In an ideal case where a glacier is in balance, net annual accumulation is equal to net annual ablation. Then, long-term thinning (where long-term is defined as the time it takes for the glacier dynamics to adjust to the prevailing climate) in the accumulation zone would not be observed as mass would be added at the same rate that it would flow and be compacted. Similarly, long-term thickening due to emergence in the ablation zone would not be observed as mass would ablate at the same rate as it would be replaced from the mass flux across the ELA (Benn & Evans, 2010). Net thinning however can occur in a balanced glacier system in the accumulation zone due to meltwater percolating in porous firn and refreezing at depth. This causes the upper layers of firn to densify and as a result, a surface lowering can be observed but no mass has been lost (Bezeau et al, 2013). This complicates the consideration of measured thinning at the surface as equivalent to submergent motion. Ice caps are unlikely to be in balance in a warming climate, and so background vertical velocity (i.e., thinning or thickening rates reflecting the long-term imbalance

state of a glacier) can be measured to differentiate long-term submergence and emergence trends from elevation change due to current mass balance and potential enhanced firn densification.

As glacier surface topography is continually adjusting to the influence of on-going ice dynamics, we inventoried background vertical velocity values calculated for DIC in the literature to estimate their potential effect on elevation bias due to differences in acquisition times between TanDEM-X rawDEMs and validation elevation datasets. Alongside our estimates of backscatter and snowpack depth variability during the frozen season, we report their values in Table 4.1. Precise and accurate measurements of vertical velocities in the field require multiple field seasons and have been previously conducted on DIC by Paterson (1976) from borehole strain measurements and repeat GPS measurements of poles drilled into the ice cap (Burgess, Pers. Comm.). Vertical movement of each measured pole was corrected for downslope movement due to ice motion. In the case of Burgess and Sharp (2008), basin-wide rates of ice thickness change were estimated by the subtraction of a modelled ice flux in a balance state from the measured ice mass flux as detailed in Section 2.5.3. Results from this study indicated net thinning across the accumulation zone of most basins (significant values range from -0.23 to -0.08 m a^{-1}, averaged in Table 4.1), with net thinning observed in the ablation zone of all basins, except for the SW basin where the ice flux across the ELA exceeds mass loss (Burgess & Sharp, 2008).

Combining the estimates in Table 4.1 by adding the maximum snowpack depth variability to the vertical velocity estimates over a period of six months (November to May) yields some estimates of maximum and minimum elevation change:

- Accumulation zone using thinning rate from Burgess and Sharp (2008):
  - maximum thinning of -0.33 m, maximum thickening of +0.09 m
- Ablation zone:
  - thinning in all basins (except SW): maximum thinning -0.37 m, maximum thickening +0.05 m
  - thickening in SW basins using rate from Burgess and Sharp (2008): maximum thinning -0.04 m, maximum thickening +0.46 m

Overall, the maximum elevation bias that could result from the difference in acquisition time of a TanDEM-X DEM and a validation elevation dataset is $\leq \pm 0.50$ m, but could be zero for both accumulation and ablation zones, either thinning or thickening. Vertical velocity rates from

Burgess and Sharp (2008) were preferred to calculate these estimates as they are averaged for the accumulation and ablation zones separately per basin, compared to the other estimates which are point values. These estimates do not include any contribution from variability in backscatter on variability in interferometrically-derived elevation over DIC, as these complex calculations are outside the scope of this thesis. However, the negligible impact of an environmental variability in backscatter of ±3 dB during the frozen season is discussed in Chapter 5.

4.2 Validation of TanDEM-X RawDEMs on Stable Terrain (Off-Ice Cap)

To investigate the accuracy of the TanDEM-X rawDEMs over terrain not covered by glacier ice we calculated elevation differences between IceBridge ATM points and overlapping rawDEM mosaics on bedrock (as defined for the co-registration process, Section 3.3.1). We first removed outliers by applying the *3 sigma rule*, removing all values greater than 3 standard deviations from the mean (>~99.7%) (Pukelsheim, 1994), which removed 0.84% of the dataset. As seen in Fig. 4.6, the remaining distribution of elevation differences is narrower than a normal distribution, with a slightly negative mean of -0.29 m and tail values up to ±6 m. The 90% confidence interval of the absolute value of all pixels is 1.54 m.

Investigation of the accuracy over stable terrain of the global TanDEM-X DEM was conducted by Wessel et al. (2018), who analyzed elevation difference with high-accuracy dGPS stations on open flat terrain. They reported a positive linear relationship between the theoretical height error (HEM) and elevation differences and a consistent mean error, but larger ranges of values for larger slopes. We investigated the influence of these two parameters on our dataset by sub-setting the pixels above and below a HEM of 1 m and a slope of 20° (Table 4.2). These cut-offs represent approximately the 90th percentile in the distribution of pixels. We found that standard deviation, RMSE and 90% confidence interval of elevation differences are reduced when considering pixels with HEM ≤1 m or slopes ≤20°, similar to findings in Wessel et al. (2018). These values are further reduced when combining the HEM and slope factor to attain a 90% confidence interval of 1.21 m. The 90% confidence interval increases up to 3.02 m in case of a HEM >1 m with all slope values combined, and to 3.59 m in case of a slope of >20° and all HEM values combined, suggesting that these factors are mostly responsible for the large range of elevation differences in this dataset (Fig. 4.6).

4.3 Updated In-Situ Mass Balance Time Series

We have updated the in-situ mass balance time series of the NW basin of DIC with more accurate hypsometry and basin divides mainly to obtain an updated time series of the net basin balances and the ELA. The net basin balances inform us of the summer conditions as they are most affected by the intensity and duration of summer melt (Koerner, 2005). The modelled ELA informs us of the location of the accumulation and the ablation facies on the ice cap, which we can relate to elevation bias patterns. Below we first describe the updated mass balance series followed by a description of the interannual variability during our study period. This information will be linked with the observed spatiotemporal patterns in elevation bias on the ice cap in the next sections.

Use of the TanDEM-X 2010-11 mosaic for the basin hypsometry to calculate mean NW basin mass balance led to a much smoother and realistic division of the elevation bands than with the previously used CDEM data (Fig. 4.7b). The use of the updated ice divide from Burgess and Sharp (2004) resulted in an increase in the NW basin area of approximately 113 km^2 between 600 and 1300 m a.s.l. (Fig. 4.7). This resulted in addition of area in the accumulation zone for 55 % of the time series (when ELA ≤1300 m a.s.l., Fig. 4.8c). We calculated that the NW basin area is 1808 ±8 km^2 in 2010, which is not significantly different from the area reported for 1960 (1811.57 ±5 km^2) and 1999 (1816.40 ±4 km^2) (Burgess & Sharp, 2004). Updating the hypsometry increased the net yearly basin mass balances on average by 1.79 ±0.59 cm w.e. and the ELA increased on average by 9.20 ±89.73 m (Fig. 4.8a). From the complete updated mass balance time series and associated parameters in Figure 4.8, the clear negative trend in mass balance since 2005 is still visible. This increase in mass loss has occurred across all ice caps in the CAA since 2005 due to an increase in summer temperatures (Sharp et al., 2011). The NW basin has thinned on average by -13.9 cm w.e. a^{-1} since 1960, a rate which has tripled after 2007 to -43.5 cm w.e. a^{-1}, from which 50% of the total 1960-2015 mass loss occurred since 2007 (Fig. 4.8b). We estimate the total thinning for the 56-year period since 1960 to be 775 cm w.e., equivalent to a mass loss of 14.03 Gt of water, or to a mass loss rate of 0.25 Gt a^{-1}. These values calculated with the updated TanDEM-X hypsometry agree with the ~700 cm w.e. (1960-2014) mass loss reported by Burgess (2017) using the old basin divides and the CDEM.

Large variations occur in the net basin balances and ELA position within the period of our validation of TanDEM-X elevations. The related variations in melt affect the subsurface properties

and could potentially affect the accuracy of the rawDEMs. Subsurface conditions affecting the frozen season TanDEM-X acquisitions reflect the last summer melt season and so the last mass balance year. For example, the in-situ data for 2009-10 reflects the conditions on the NW basin for the TanDEM-X DEM collected in fall 2010 to spring 2011. Mass balance year 2010-11 was the most negative year of the record, with a basin thinning average of -74.3 cm w.e. and an ELA at 1656 m a.s.l. Two years later, mass balance year 2012-13 stands out with a slightly positive mass balance of +1.3 cm w.e. and an ELA <1100 m a.s.l., a first since 2003-04. These extremes correlate well with the record of mean summer temperatures in the CAA reported in Mortimer et al. (2016) from LSTs derived from MODIS, climate reanalysis data and near-surface air temperatures recorded at Environment and Climate Change Canada weather stations in the Arctic. Summers 2009-2012 were exceptionally warm in the CAA and presented positive anomalies in mean summer land surface temperature, enhancing ice cap melt. Enhanced melt features and formation of thicker ice lenses in the percolation and saturation zone due to intense melt events could potentially reduce the observed elevation bias for these years. Summer 2013 was abnormally cold and amongst the coldest summers on record at the Resolute Bay weather station (Cornwallis Island, west of Devon Island), which likely caused little melt on DIC. Lower melt and increased snowpack depth in the percolation and saturation zone after the end of a colder summer could lead to an increased elevation bias as volume scattering would be enhanced. The general increasingly negative mass balance trend resumed for 2014 and 2015, following this abnormally low melt year.

4.4 Validation of TanDEM-X Elevation Bias on Devon Ice Cap

In their investigation of elevation bias in TanDEM-X DEMs over Greenland, Abdullahi et al. (2018) showed that the HoA had a great influence on calculated elevation bias between rawDEMs and ICESat points for similar ground conditions. They ignored the impact of this parameter by choosing only rawDEMs with similar HoA for their analysis. With much fewer data available on DIC, we did not have the option to refine our selection of rawDEMs based on HoA. Hence, before presenting results on spatiotemporal variations of elevation biases over the ice cap and linking them with the in-situ mass balance time series, we first need to consider the impact of HoA on our dataset and its relationship with other SAR acquisition parameters.

4.4.1 Influence of SAR Acquisition Parameters on Elevation Bias on Glacierized Terrain

To investigate the impact of HoA in our dataset, we selected the few validation elevation datasets which overlapped multiple rawDEMs with different HoA acquired within the same frozen season. This resulted in the selection of 13 "pairs" of elevation difference (dH) rasters where ground conditions were the same but SAR acquisition parameters, namely HoA, baseline, coherence and amplitude were different. We calculated the mean elevation bias, coherence and amplitude in these overlapping regions per pair and present their relationships in Figure 4.9a and b.

As mentioned previously, coherence is degraded at small HoA, affecting the quality of the produced DEM (Gruber et al., 2016; Rizzoli et al., 2017a). This relationship is clear in Figure 4.9a where a positive correlation between coherence and HoA is visible (x-component of the arrows, pointing right), agreeing with the findings of Abdullahi et al. (2018). This also agrees with Martone et al. (2016), who showed a positive relationship between volume decorrelation and HoA in rawDEMs over the Greenland Ice Sheet (i.e., that less coherence is lost by volume scattering at higher HoA). Hence, the relationship between coherence and HoA observed in our dataset could be due to the large contribution of volume decorrelation to HoA.

The relationship of these two parameters (coherence and HoA) with the elevation bias is not as clear. In the pairs plotted in Figure 4.9a, the mean elevation bias varies by as much as ±2 m but stays within the standard deviation as a result of a change in HoA (y-component of the arrows in Fig. 4.9a). It is therefore difficult to identify from our dataset if the resulting absolute elevation bias from an increase in HoA is lower or higher. A smaller increase in HoA (~5-10 m) increases coherence and *reduces* elevation bias (group of arrows in the center pointing upwards, Fig. 4.9a). Conversely, a larger increase in HoA (~>10 m) increases coherence and *increases* elevation bias (arrows pointing downwards, Fig. 4.9a). This contradicting relationship is also visible in Figure 4 in Abdullahi et al. (2018), where for a similar HoA, as coherence increases absolute elevation bias decreases, but largest elevation biases are found at highest coherence and HoA. Hence, the few dH raster "pairs" with similar ground conditions and different SAR acquisition parameters in our dataset reflect a similar pattern to that seen in Abdullahi et al. (2018).

No specific relationship between mean amplitude, elevation bias and HoA is expected as amplitude is a function of the incidence angle (Wessel, 2016). Lowest amplitudes are seen for the

pairs with the largest standard deviation meaning that a larger area and range in backscatter values are covered by their overlapping region. An increase in HoA leads to a small positive or negative change of <50 DN in amplitude (Fig. 4.9b).

To summarize, with our relatively small sample (N = 13) we can illustrate that for unchanged ground conditions the relationship between SAR acquisition parameters and elevation bias on glacierized terrain in the TanDEM-X rawDEMs is as follows:

- For a large change in HoA (>10 m): $B_{\perp} \downarrow \rightarrow HoA \uparrow \rightarrow COH \uparrow \rightarrow |\boldsymbol{dH}| \uparrow$
- For a small change in HoA (5-10 m): $B_{\perp} \downarrow \rightarrow HoA \uparrow \rightarrow COH \uparrow \rightarrow |\boldsymbol{dH}| \downarrow$

4.4.2 Spatiotemporal Variability in Elevation Bias

We first investigated the general pattern of elevation bias ($|dH|$) in the rawDEM data by extracting significant dH values on ice for each validation dataset per year at 50 m elevation band intervals (Fig. 4.10). As mentioned in Chapter 3, in this thesis a negative elevation difference represents a TanDEM-X surface elevation that is below the "true" surface given by the validation elevation dataset and the term elevation bias is used to denote absolute elevation difference.

Average elevation bias on DIC ranges between -2.49 ±0.53 m in 2012-13 to -2.96 ±0.48 m in 2010-11, and height error is on average 1.18 ±0.08 m, albeit with some local variability (Fig. 4.10). There is generally good agreement between the results from the different types of elevation validation datasets except for frozen season 2013-14, when the IceBridge ATM data shows much lower elevation bias values compared to the ArcticDEM data. This is likely due to the difference in HoA of the rawDEMs used in these calculations, with the IceBridge ATM data having a HoA of 73 m over Belcher Glacier, compared to HoAs of 84 and 69 m over most of the ice cap for the ArcticDEMs (Fig. 3.3), although both datasets are within one standard deviation of each other. For the three first frozen seasons, dH dips slightly towards -4 m above ~1000 m a.s.l. elevation and then increases back towards -2 m. Highest elevation bias corresponds well with the location of the previous summer NW basin ELA, except for 2011-12. For this year, the data is from the eastern part of the ice cap only (Fig. 3.3) so a comparison with the NW basin ELA is more problematic. The three first years with relatively warm previous summers contrast with 2013-14 and 2017-18, where absolute elevation bias increases above ~1500 m a.s.l. This suggests that on average the cool summer of 2013 affected the near subsurface enough to modify elevation bias seen in the TanDEM-X data. Differences in elevation bias and height error above and below the 2000-2015

ELA at 1400 m a.s.l. are within one standard deviation of each other, hence not significantly different. However, significantly more variability in the height error is seen below 1000 m a.s.l. (1.24 ±0.06 m) compared to above (1.11 ±0.02 m) The same can be said from the average elevation bias with -2.55 ±0.15 m below 1000 m a.s.l. and -2.94 ±0.15 m above.

To visualize spatial variability of elevation bias and any difference before and after the cool summer of 2013 we mosaicked the ArcticDEM-derived elevation bias rasters and auxiliary rawDEM datasets (Fig. 4.11). Effects of mosaicking multiple rasters are visible in both years in Figure 4.11c to g due to the combination of ArcticDEMs with variable height errors following co-registration, and rawDEMs with different SAR acquisition parameters. As expected, negative dH is located on the ice cap and snow-covered areas and non-significant dH on bedrock areas (Fig. 4.11b). Non-significant dH is located on the ice cap mostly at lower elevations within the upper reaches and valleys of Sverdrup, Eastern and North Croker Bay glaciers. Some pixels with positive bias on the order of a few meters occur sparsely on bedrock areas and rarely on the ice cap.

Different spatial patterns in the frozen seasons of 2012-13 and 2013-14 appear on the ice cap in the negative elevation bias, height error, coherence and amplitude rasters (Fig. 4.11c to g). In 2012-13, elevation bias is lower above ~1600 m a.s.l. (-2 to -3 m), increases at lower elevations until ~1300-1100 m a.s.l. (-3 to -5 m), then decreases again at lower elevations in the upper reaches of Sverdrup and Eastern glaciers where pixels with non-significant bias start to dominate. The boundary of this zone in the center of the ice cap matches well with the previous summer ELA in the NW basin (1548 m a.s.l.) suggesting that it corresponds to the boundary between the percolation and saturation zone. This pattern is even clearer when subtracting the mean bias on the ice cap (Fig. 4.11d). The central zone, above ~1600 m a.s.l., consists of a random distribution of pixels with values of ±1 m around the mean bordered by pixels well below the mean. The location of pixels with dH values well above the mean (+3 to +4 m) corresponds exactly to the location of increased ice flow velocity into Sverdrup, Eastern and North Croker Bay glaciers as reported in Van Wychen et al. (2017). The different elevation bias zones correlate well with the mosaic of the height error map and the coherence of the rawDEMs. The areas with lower elevation bias on the ice cap have a higher coherence and lower height error, with highest coherence occurring in the bedrock areas, where the height error is <1 m. This corresponds to flat and low sloped terrain, and where volume scattering is reduced by only occurring in the snowpack over bedrock. This results

in a non-significant elevation bias. Amplitude correlates mostly with elevation and incidence angle, visible on eastern valley sides where maximum amplitude is recorded entirely due to the incidence angle on the local topography.

In 2013-14, the elevation bias pattern is completely changed in the ice cap center where a low to high absolute dH gradient occurs from east to west (Fig. 4.11). Upper reaches of valley glaciers still display higher values than the mean dH, mostly visible in the case of North Croker Bay Glacier. Even if the HoAs of the rawDEMs used in 2013-14 are much higher than for 2012-13 (noticeable from the increase in coherence on the ice cap, Fig. 4.11g), the presence of a different pattern is still valid because the change in HoA would only affect the magnitude of the calculated elevation differences. Significant differences also occur in this frozen season for the height error map, with values between 1 and 1.5 m over the ice cap center and higher on the valley glaciers, compared to a majority below 1.25 m in 2012-13. This is due to higher RMSE on average from co-registration of ArcticDEM strip DEMs for 2013-14.

To obtain a better overview of the spatial and temporal patterns in dH we extracted values on 6 transects across the ice cap which covered most basins and the entire elevation range (Fig. 3.2, Fig. 4.12). We obtained a single elevation bias profile per frozen season by averaging data from all validation elevation datasets, regardless of the HoA of their corresponding rawDEMs. To illustrate a larger error in the case of averaging dH values associated with different HoAs, we kept the largest range in error values (dH HEM). A moving average window size of 5 (~250 m) was applied to smooth the datasets for better visualisation of elevation bias patterns, which removed most values for frozen season 2017-18 from the SEARCH data.

In all transects, elevation bias for all the frozen seasons are within error limits of each other. This can be explained in two ways: (1) change is occurring at a smaller scale than we can detect and is below our error limits, and/or (2) difference in HoA in the rawDEMs and its effect on elevation bias is preventing us from detecting any change occurring at the scale we are observing. In parts of some transects, general patterns of spikes and troughs are aligned in multiple years but offset vertically, which points towards explanation (2) (e.g., transect 6, Fig. 4.12f). In other parts, a different pattern of spikes and troughs is seen between years, pointing towards explanation (1) (e.g., km 40 to 80 in transect 2, Fig. 4.12b). This uncertainty could be resolved with comparison of subsurface data over multiple years, but data to do this is currently very limited. Hence, we

focus our analysis on the general patterns of elevation bias, linking them to elevation range, glacier facies zones, and ice surface velocity patterns.

For the North-South transects 1 and 2, less variability in elevation bias between -2 to -4 m is seen at elevations above ~1500 m a.s.l. compared to lower elevations (Fig. 4.12a and b). These elevations correspond to the accumulation zone and correlate well with the updated ELA from the NW basin for frozen seasons 2010-11 to 2012-13. The first 27 km of transect 2 are in the valley of Eastern Glacier, in the bare ice zone, where the error limits in the elevation bias make it partly indistinguishable from zero (Fig. 4.12b). An interesting spike of lower elevation bias present in both 2012-13 and 2013-14 in transect 2 between km 30 and 31 (Fig. 4.12b) corresponds exactly to the transect crossing a zone with higher than average elevation bias in Figure 4.11d. For the East-West transect 3 (Fig. 4.12c), small variability is seen across the profile up to km 100, and then variability increases towards the eastern margin of the ice cap on land. In line with the different pre- and post-summer 2013 elevation bias trends seen in Figure 4.10 and 4.11, elevation bias in transect 3 decreases towards the summit (towards the East) around km 70 pre-2013, but increases post-2013. A sustained decrease in elevation bias between km 122 and 125 in transect 3 in 2011-12 corresponds to an increased ice flow area towards East 6 Glacier as reported in Van Wychen et al. (2012, 2017). In transect 4 (Fig. 4.12d), following the in-situ mass balance transect, elevation bias gradually increases as elevation increases and largest variability is seen close to the average 2000-2015 ELA at 1400 m a.s.l. A similar pattern in transect 4 to that shown in Figure 4.10 is seen pre-2013, where absolute dH decreases at higher elevations (past km 30) and the opposite occurs post-2013. In transect 5 (Fig. 4.12e), dH is not significantly different from zero in the Sverdrup Glacier valley and increases rapidly above ~1000 m a.s.l. when the transect bifurcates west. This agrees with the significance of elevation bias and difference with the mean as seen in Figure 4.11b, c and d. Along Belcher Glacier valley, the elevation bias in transect 6 is highly variable (Fig. 4.12f), in part not significantly different from zero and generally increasing past the main North-South ice divide (~km 45). A prominent lowering in elevation bias between km 74 and 80 corresponds to a surface depression and to the location of fast flowing ice in upper Southeast 2 Glacier as identified by Van Wychen et al. (2012, 2017).

4.4.3 Comparison with Observations of Near Surface Stratigraphy and Density

4.4.3.1 Shallow Firn Cores

Three shallow firn cores were collected in May 2018 at the three upper AWS on DIC where firn was present below the snowpack (Fig. 4.13a). Snowpack depth above the core location ranged from 29 to 38 cm, and all contained layers of hard wind packed snow, icy crusts and depth hoar at the bottom of the snowpack. Core densities ranged from ~350 to ~720 kg m^{-3}, encompassing the value of ~600 kg m^{-3} often assumed as the average firn density for mass balance calculations (Huss, 2013). The presence of piping and horizontal ice lenses in all cores demonstrates high spatial variability of melt features (Fig. 4.13a and c). This correlates well with previous work on the distribution of melt features in ice cores and snow pits in the accumulation zone of DIC, which has been characterized as sporadic, both vertically and horizontally (Bell et al., 2008; Koerner, 1997). Large layers of ice above firn and saturated firn follows the recent trend of increasing ice content in firn, and the movement of facies upglacier reported in Gascon et al. (2013).

Significant elevation differences occur in the comparison of the rawDEM collected in spring 2018 and the dGPS transect collected near the AWS and firn core locations (Fig. 4.13b). Proportions of pixels with significant elevation differences are 100%, 99%, 92%, 100% and 35% for DV1H, DV3F, DV7D, DICS and DVSVW, respectively. Mean elevation bias cannot be directly linked to a specific depth in the firn core, but their stratigraphy gives a general indication of the subsurface properties near the dGPS transect that can be related to glacier facies zones. Sites DV1H and DV3F have similar core stratigraphy with alternating firn and ice layers below 125 cm and a very similar distribution in elevation bias: median dH and median error of -2.78 ±1.04 m and -2.76 ±0.89 m respectively. The upper part of the cores, free of piping but with thin horizontal ice lenses, suggest that they are in the percolation zone where low melt conditions occurred in the past few summers prior to core collection. Thick ice layers at depth above firn (below 150 cm), especially thicker for DV3F, indicates higher melt events in the recent past. These ice layers could have been created in the warm summer conditions of 2010 to 2012 and have increased in thickness as water percolating down in subsequent years refreezes at the ice layer interface. This phenomenon would be similar to the reported increased thickness of ice layers in the upper 3 m of firn core collected between Sites 1 and 2 of the CryoSat transect by Bezeau et al. (2013) between 2006 and 2012 during a period of increasing surface melt.

The stratigraphy of core DV7D suggest that it could be in (and have alternated between) the saturation zone or the superimposed ice zone depending on the thickness of the bottom ice layer of the core and presence of firn below. This agrees with the boundary of the upper superimposed ice zone being identified higher at 1658 m a.s.l. in spring 2011 in the GPR profile of De Jong (2013). This site is also above the maximum ELA recorded in the updated in-situ time series in 2010-11 at 1656 m a.s.l., which further supports its location as being in the lower saturation/superimposed ice zone. Median dH and error are the lowest at this site with values of -1.85 ±0.83 m. This could be due to higher coherence values at this site in the rawDEM acquisition due to the presence of melt features and thick ice layers closer to the surface, but this cannot be verified due to the COH raster for the 2018 spring rawDEM being unavailable.

No core was collected at site DVICS because the surface was pure glacier ice below the snowpack and near the AWS. Higher dH and associated error at this site suggest an overall lower coherence. The rawDEM of spring 2018 was acquired with a relatively low HoA (65.70 m) and lower coherence, meaning that a larger dH on average can be expected. Located at ~1335 m a.s.l., this site was in the bare ice zone in summer 2017 or in the lower superimposed ice zone in recent cool years.

Site DVSVW is in the bare ice zone and is the only site at which significant positive elevation biases (~ +2 m) were detected at a few pixels even with the largest height error on average (median = 1.23 m). Snow cover was relatively thick (~50 cm) at this site, which provided a level surface for the dGPS transect acquisitions. The variability in dH potentially reflects the variability in the ice surface condition at this site (presence of debris, cracks, cryoconite holes, etc.) making it the only one where most pixels are within error limits and elevation bias is not dominant.

4.4.3.2 Ground Penetrating Radar Profiles

GPR profiles acquired in spring 2011 by Gascon et al. (2013) and De Jong (2013) form a continuous line from the SW basin towards the summit and downwards to the NW basin as they both started at Site 1 on the CryoSat transect (Fig. 2.4). Average slope of both transects is low, with 2.5° in the SW (~800 m drop over 40 km) and 1.15° in the NW (~500 m drop over 25 km).

Facies boundaries have been identified in both transects from the presence and density of ice layers at depth in the GPR profile and ice cores by Gascon et al. (2013), and from GPR and

backscatter intensity in ENVISAT imagery by De Jong (2013). Over the period 2006-2011 where both studies overlap, the location of the upper superimposed ice zone was identified to be ~240 m higher on average in the NW basin than in the SW basin. A higher boundary for this facies in the NW basin is expected as the long-term ELA has been shown to be higher in this basin than in the SW basin (Koerner, 2005). A similar pattern in the elevation bias is apparent in both transects where elevation bias is significant and negative (Fig. 4.14 and 4.15). In the percolation zone, dH is on average -3 ±1.5 m. Towards the superimposed ice zone an increase in dH is seen with larger variability, closer to -4 ±2 m. This is clear in Fig. 4.14b in the saturation zone where dH seems to follow an inverse relationship with depth of the thick ice layers: it increases when thick ice layers are closer to the surface and reduces when a pocket of firn is located above them. The pattern is not so evident in the NW transect due to the horizontal scale of Fig. 4.15 but spikes in the spline fit of dH do occur at boundaries of changing ice layer thickness. Large variability in dH continues in the superimposed ice zone in Fig. 4.14a, where measured values are as low at -7.5 m and as high as -1 m. A slight decreasing tendency in absolute dH is visible in the glacier ice zone in the SW basin (Fig. 4.14a).

Table 4.1 Factors affecting real and perceived surface elevation on Devon Ice Cap over a period of 6 months (frozen season), corresponding to the maximum difference between a rawDEM acquisition and validation data acquisition. Estimate of height change derived from Burgess and Sharp (2008) converted from m w.e. a^{-1} to m a^{-1} using ice density of 900 kg m^{-3}.

Component		Estimates	Reference	Estimate of height change from November to May (m)
Perceived	Variability in backscatter	Environmental variability: ±3.5 dB from October to May from analysis of Wide ScanSAR scenes over 2 consecutive winters	(this study)	Most likely negative but negligible
Real	Snowpack depth variability	Relative surface height data from AWS on mass balance transect (NW basin): ± 0.05 m on average, ±0.21 m at 90% confidence interval	(this study)	± 0.05 to ± 0.21
	Dynamic vertical elevation change	- 0.57 m a^{-1}, combination of reported firn compaction rate and normal strain rate	Paterson (1976): measured from deformation in surface to bedrock borehole in 1971 near Devon Ice Cap summit	Accumulation zone: - 0.29
		Linear trend from ~ -0.5 m a^{-1} in the percolation zone towards 0 m a^{-1} at the upper ablation zone boundary. Increases rapidly to +0.8 m a^{-1} at the ice cap margin.	Unpublished data, personal communication with Dr. Burgess (GSC): measured on 37 mass balance poles along the CryoSat transect (Fig. 2.4) intermittently between 2004 and 2012, each point is averaged from at least 3 consecutive years.	Accumulation Zone: - 0.25 to 0 Ablation Zone: 0 to + 0.40
		Accumulation zone: indistinguishable from 0 except for • SE basins: -0.23 ±0.11 m w.e. a^{-1} • upper Fitzroy and Eastern Glaciers: -0.07 ±0.64 m w.e. a^{-1} Ablation zone: • indistinguishable from 0 in Southeast Glaciers • NE and SE basins: -0.36 ±0.21 m w.e. a^{-1} • SW basins: 0.55 ±0.22 m w.e. a^{-1} • NW basins: -0.14 ±0.06 m w.e. a^{-1}	Burgess and Sharp (2008): Basin-wide thickness changes from difference in balance velocity fluxes and observed velocity fluxes. Estimate extracted from Fig. 3 in Burgess and Sharp (2008).	Accumulation zone: 0 to - 0.12 Ablation zone: - 0.16 to + 0.25

Table 4.2 Elevation difference over stable terrain for a subset of IceBridge ATM points based on Height Error Map (HEM) or surface slope. Range of values for HEM: 0.20 to 18.35 m. Range in slopes: 0 to 62.43°.

Subset of IceBridge ATM points	N	Mean Error (m)	Standard Deviation (m)	RMSE (m)	Absolute values 90% Confidence Interval (m)
HEM ≤1 m	84984	-0.30	0.85	0.90	1.32
HEM >1 m	12775	-0.21	1.78	1.79	3.02
Slope ≤20°	87754	-0.29	0.83	0.88	1.32
Slope >20°	10005	-0.29	2.05	2.07	3.59
HEM ≤1 m and Slope ≤20°	79005	-0.29	0.74	0.80	1.21

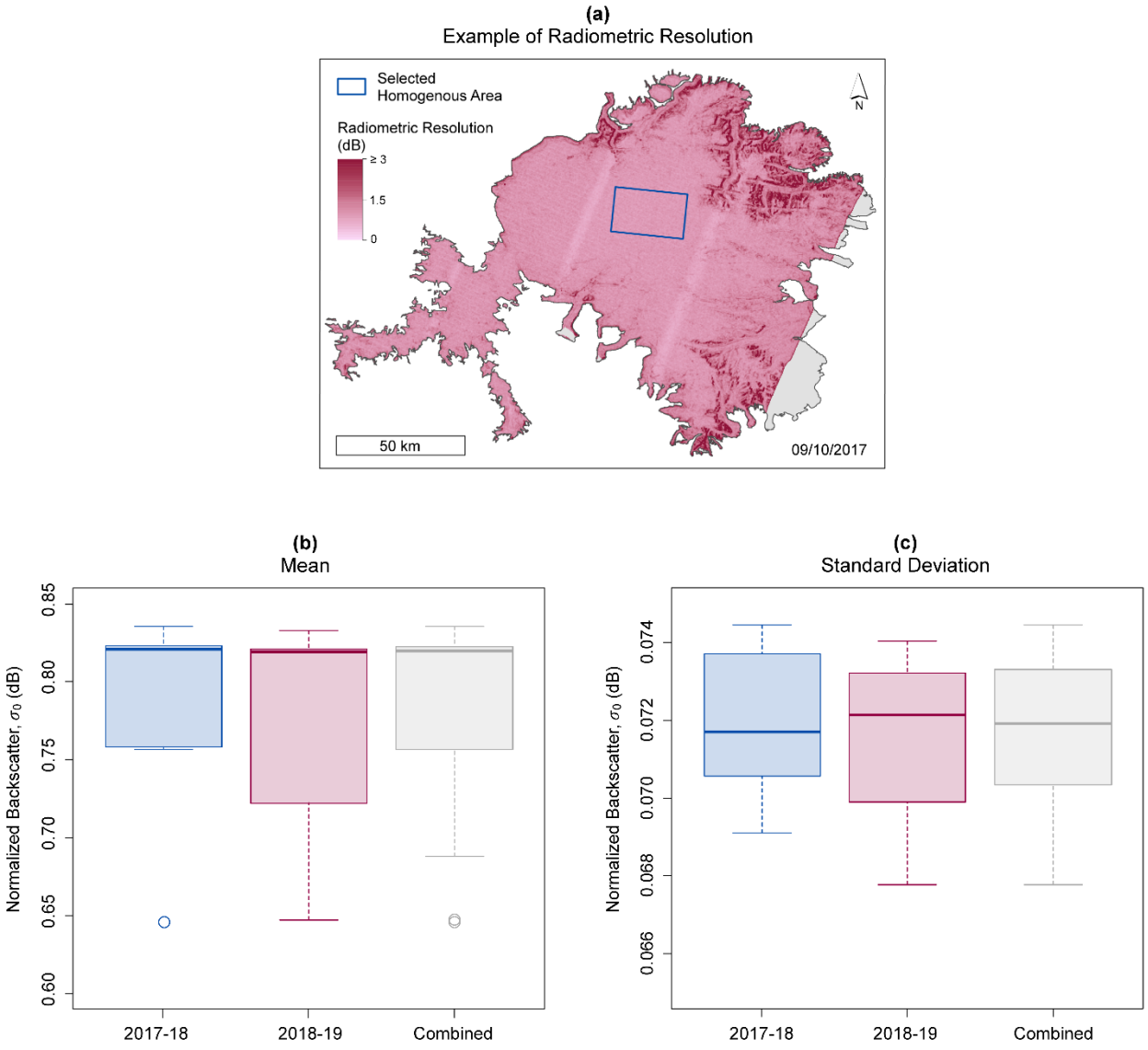

Figure 4.1 (a) Example of radiometric resolution (dB) for Wide ScanSAR scene 09/10/2017 and selected homogenous area in the middle of Devon Ice Cap (~488 km^2). Ice Cap outline in grey from Burgess and Sharp (2004). Projected in WGS84 UTM 16N. Wide ScanSAR TerraSAR-X and TanDEM-X data © DLR, 2019. Boxplots of: (b) mean, and (c) standard deviation of radiometric resolution in dB calculated in the selected homogenous area shown in (a) for 2017-18 (including the summer scene), for 2018-19, and for both periods combined.

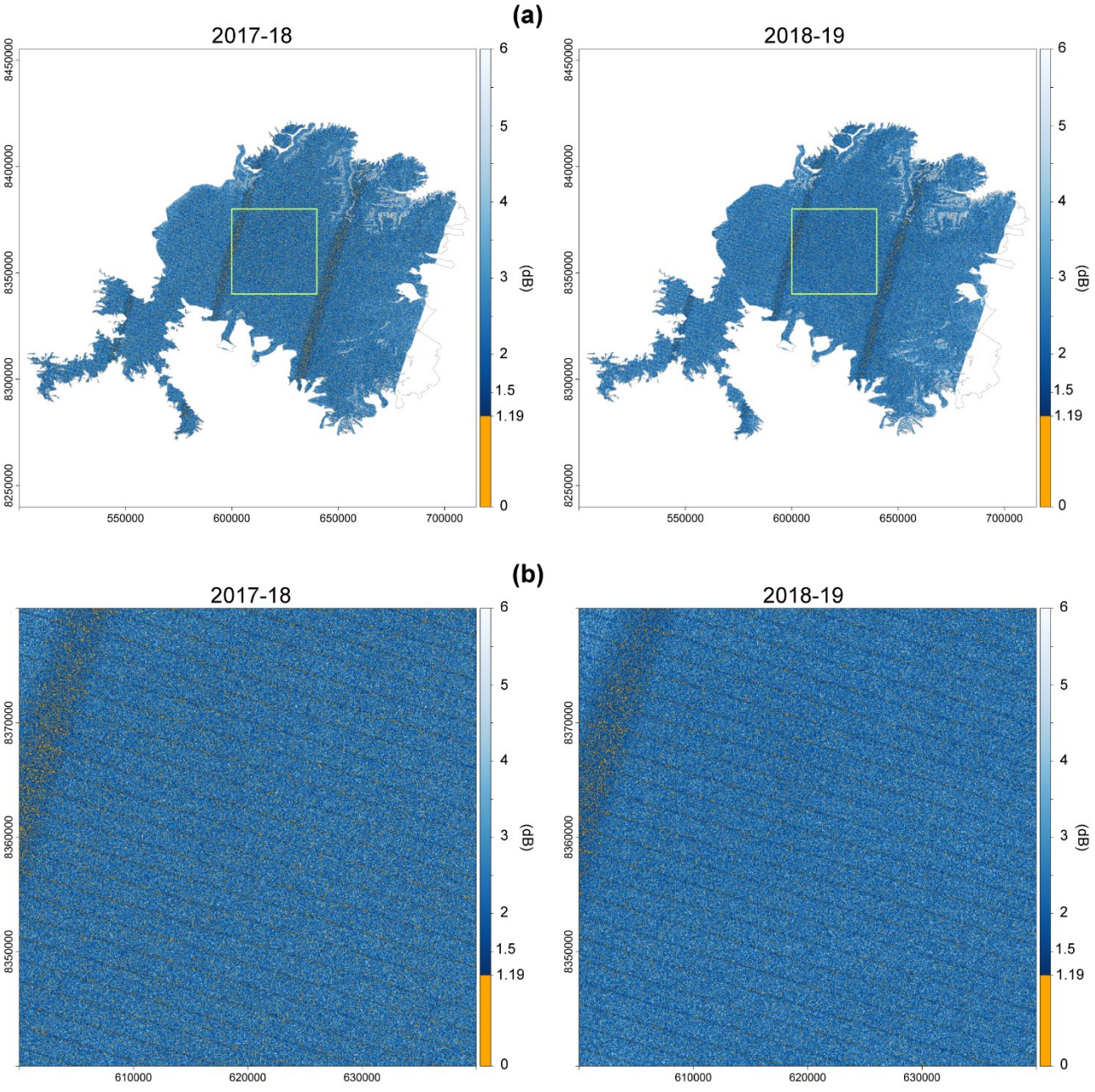

Figure 4.2 (a) Range of backscatter values (in dB) per pixel from October to May in 2017-18 and 2018-19. Green box shows the extent of the zoom in (b). Pixels where no change can be detected (<1.19 dB) are in orange. Devon Ice Cap 1999 outline from Burgess and Sharp (2004) in grey. Projected in WGS84 UTM 16N. Wide ScanSAR TerraSAR-X and TanDEM-X data © DLR, 2019.

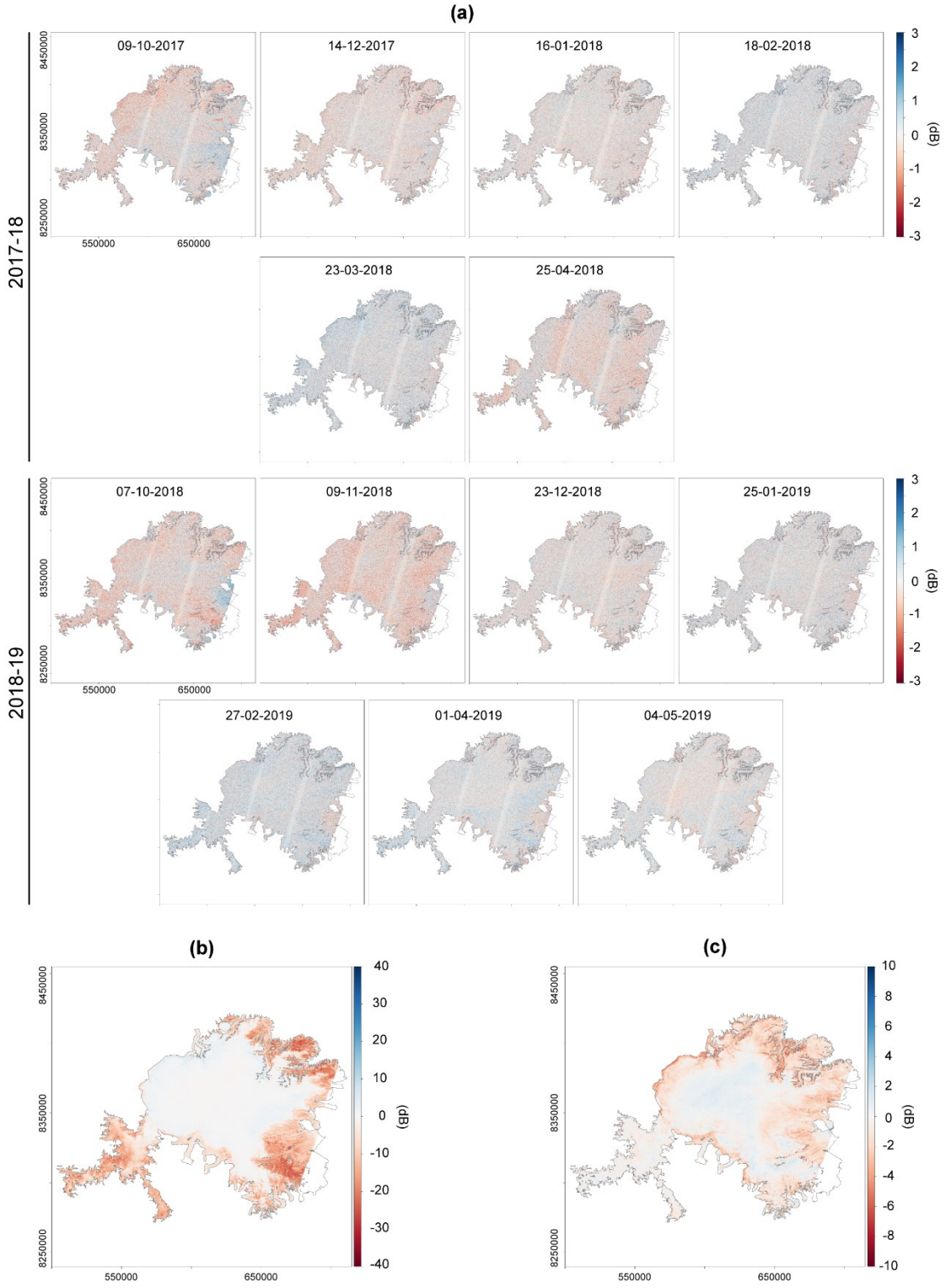

Figure 4.3 (a) Difference of each scene from their respective October to May mean, top rows: 2017-18, bottom rows: 2018-19. (b) Difference between scene 30/06/2018 (when melt is occurring) and the 2017-18 frozen season mean. (c) Difference between the 2017-18 and 2018-19 frozen season means. For all panels the pixel spacing is 45 m and the Devon Ice Cap 1999 outline from Burgess and Sharp (2004) is grey. Projected in WGS84 UTM 16N. Wide ScanSAR TerraSAR and TanDEM-X data © DLR, 2019.

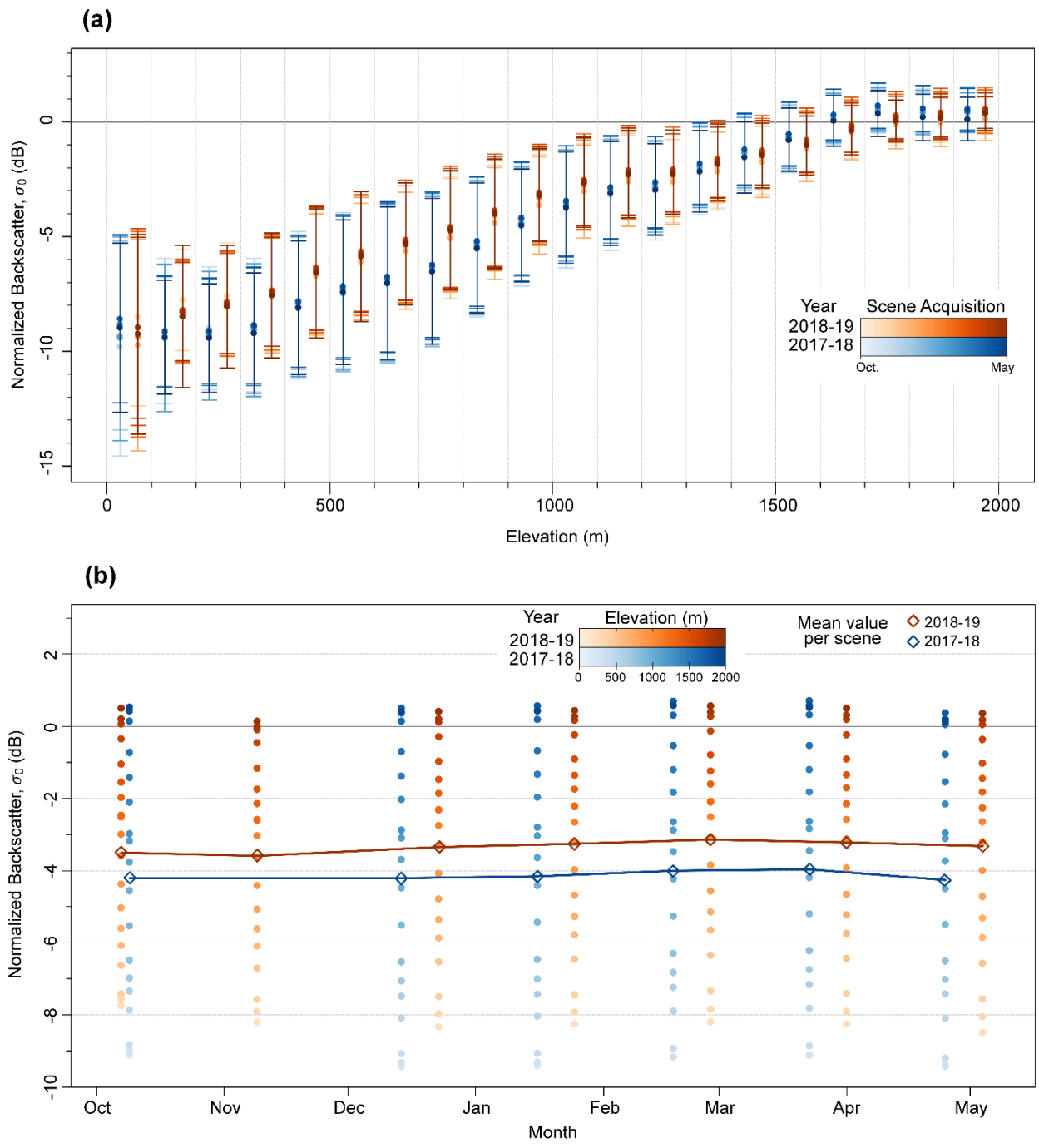

Figure 4.4 (a) Mean backscatter and standard deviation per 100 m elevation band on ice for all frozen season scenes. Colour gradients from first fall acquisition to last spring acquisition in each year. (b) Mean backscatter per scene for elevations above 100 m. Points represent mean value per 100 m elevation band from 100 to 1920 m a.s.l. Elevation bands created from TanDEM-X 2010-14 mosaic and masked with the ice mask described in Section 3.3.1.

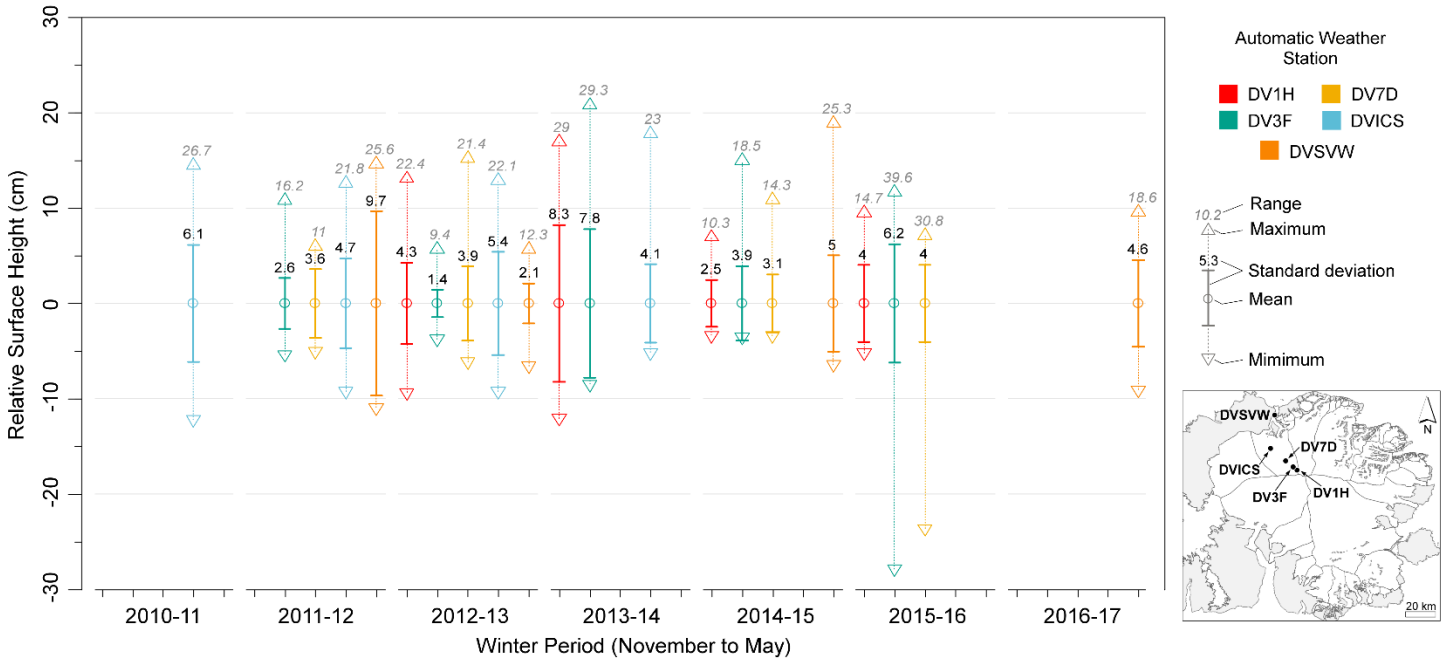

Figure 4.5 Distribution of relative surface height measured at all Automatic Weather Stations for the November to May inclusive periods from 2010-11 to 2016-17. Mean in each distribution was set to 0 to facilitate comparison between them. Data shown for all stations with at least 75% of days with data (159/244 days); note that no stations had sufficient valid data in 2017-18.

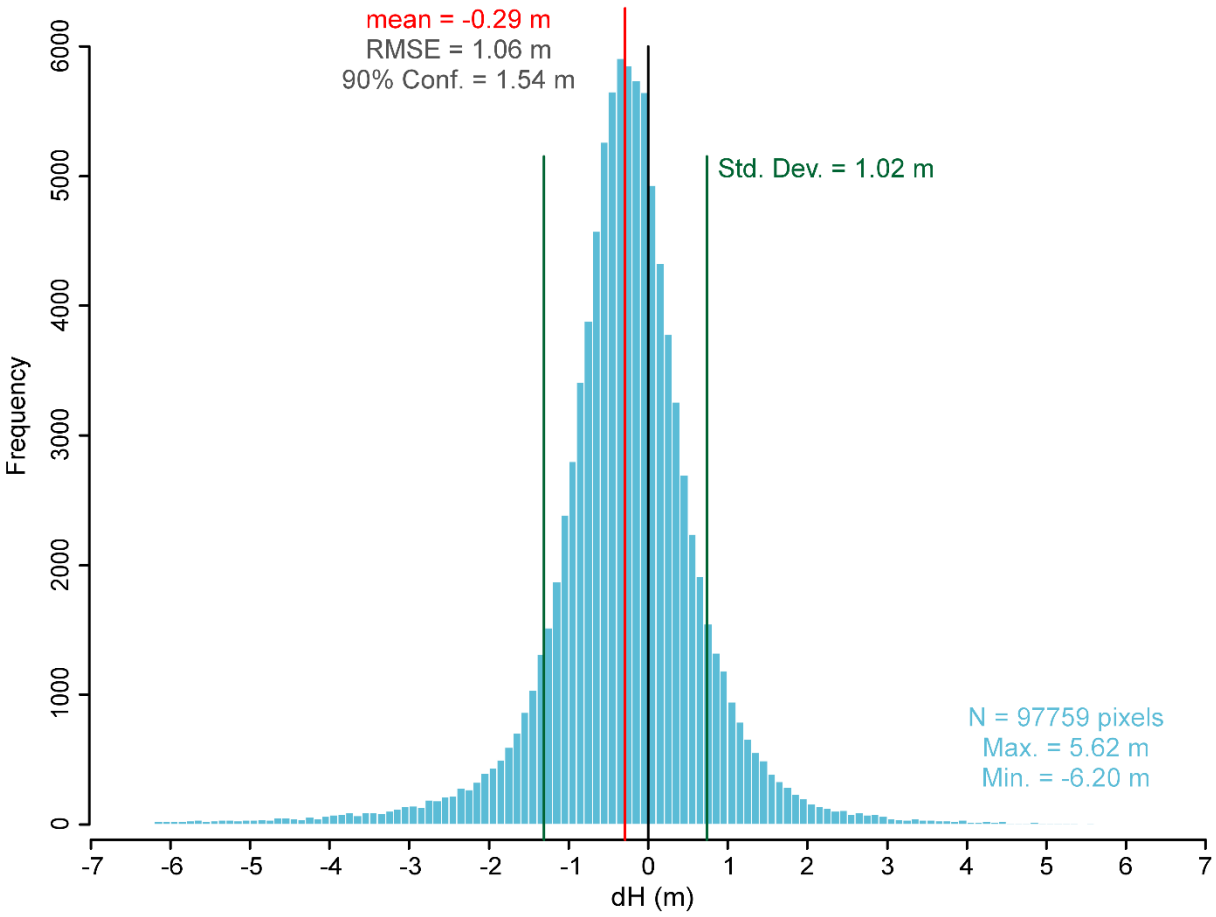

Figure 4.6 Histogram of elevation difference (dH) over stable terrain for IceBridge ATM (2012 and 2014) points converted to 12 m pixels which overlapped rawDEM mosaics (1009244_12/12/2010,1023146_07/04/2011,1055856_24/03/2012,1073326_02_04_15/04/2012). Bins are 0.1 m wide. Vertical accuracy of IceBridge ATM points is 0.15 m (Schaffer, 2017).

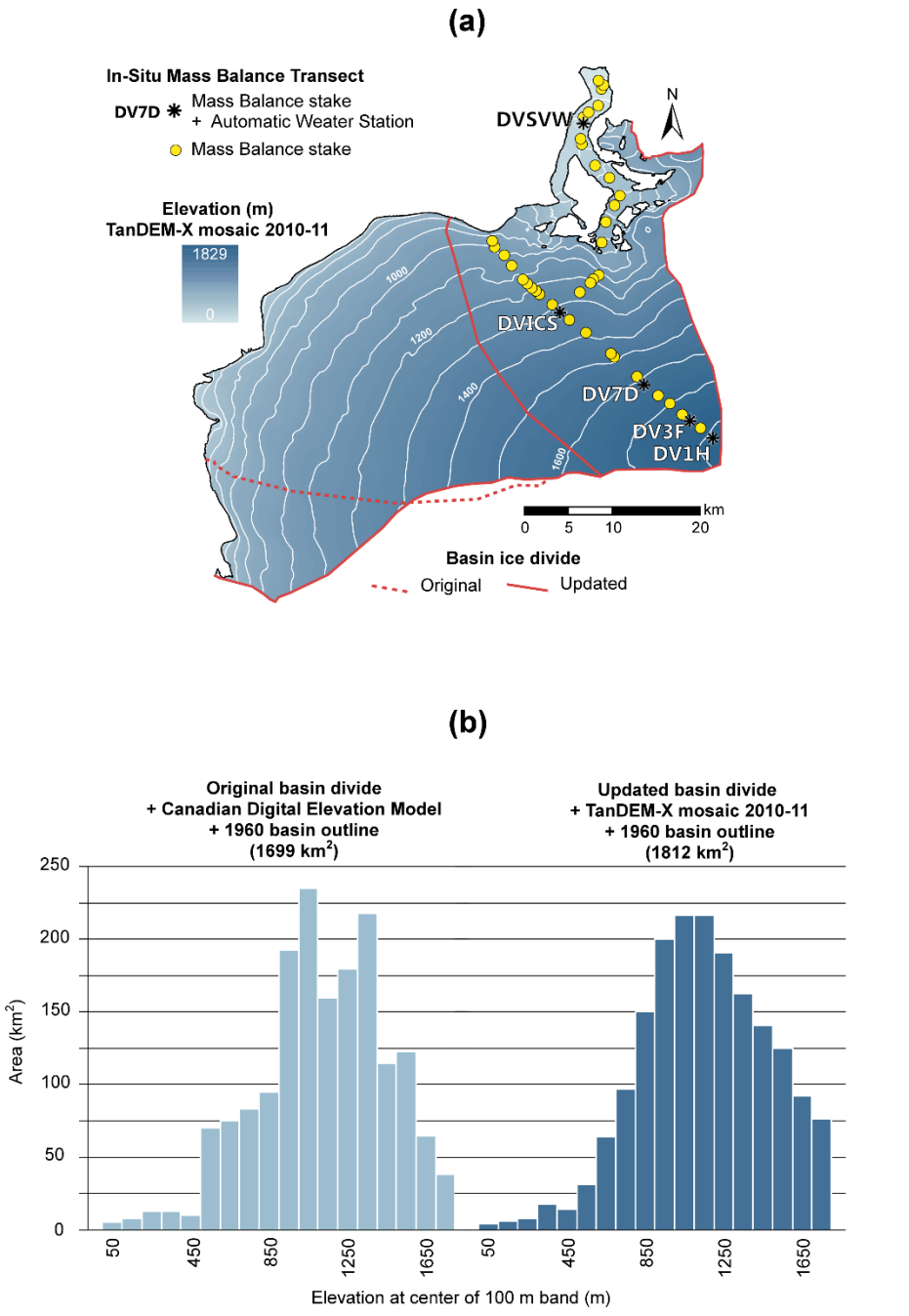

Figure 4.7 (a) Representation of original and updated ice divides from Van Wychen et al. (2012) for the NW basin of Devon Ice Cap with TanDEM-X DEM mosaic from 2010-11 and location of the in-situ mass balance transect. (b) Comparison of basin hypsometry from the original basin divide and the Canadian Digital Elevation Model with the updated basin divide and the TanDEM-X 2010-11 mosaic. The 1960 basin outline from Burgess and Sharp (2004) is used in both cases. The TanDEM-X derived hypsometry from the 2010-11 mosaic is assumed to be valid for 1960 because large elevation bands (100 m) are used. The last elevation band (1700 to 1800 m) includes the small portion of area above 1800 m a.s.l..

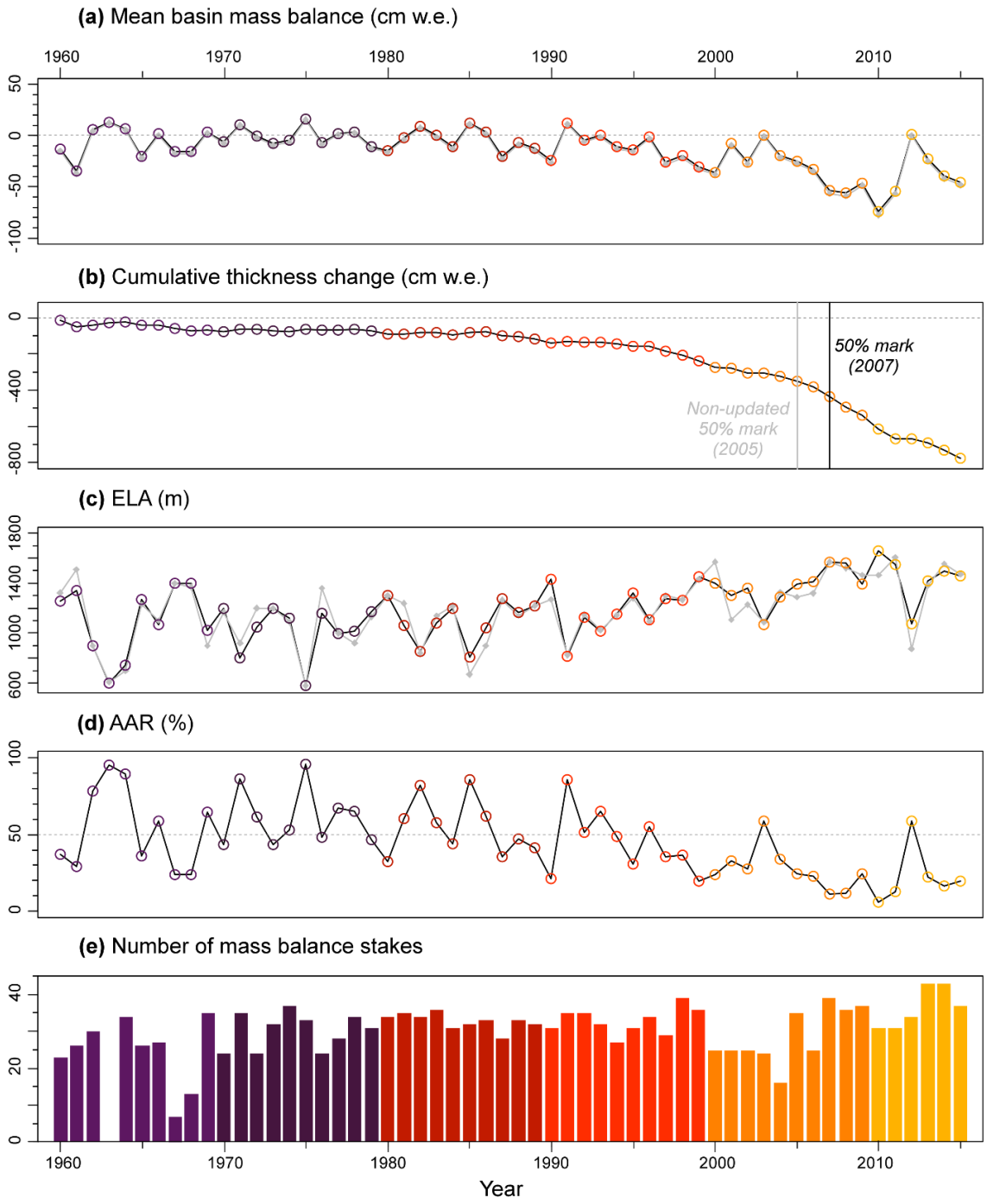

Figure 4.8 (a) The 56-year (1960-2015) NW basin mass balance record using updated hypsometry. Mass balance values are reported as thickness change in cm w.e. A third order polynomial was fitted to the individual stake balances and modelled values were extracted at the centre of each 100 m elevation band. Net average values were calculated as a weighted average according to the most recent basin hypsometry (updated in 1999 (Burgess and Sharp, 2004) and 2010 (this study)). Non-updated time series in grey. (b) Cumulative basin mass balance reported as thickness change in cm w.e. (c) Modelled equilibrium line altitude (ELA). Non-updated time series in grey. (d) Accumulation area ratio (AAR) defined as the fraction of area of the basin above the ELA. (e) Number of stakes with recorded mass balance (max. = 43).

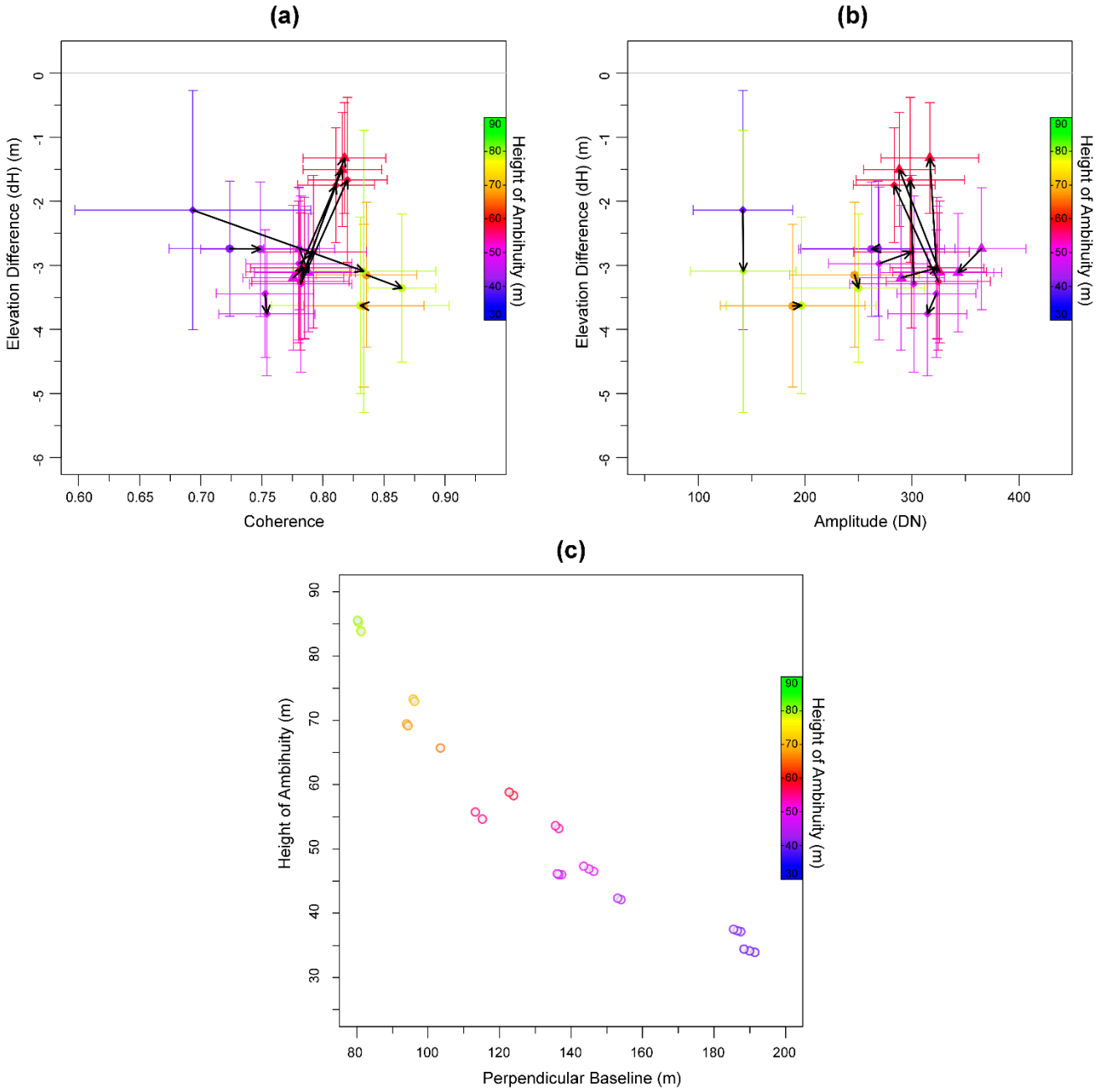

Figure 4.9 Relationship between: (a) mean coherence and mean elevation bias, (b) mean amplitude and mean elevation bias, coloured by Height of Ambiguity (HoA) calculated from all validation datasets overlapping multiple rawDEMs in the same mass balance year (N = 26, 13 pairs). Arrows link each pair from the associated rawDEM HoA from the smallest to the largest. Elevation bias values calculated on ice only using the ice mask described in Section 3.3.1. Error bars indicate the standard deviation. (c) Distribution of perpendicular baseline and associated HoA for all rawDEMs (N = 29), colored by HoA.

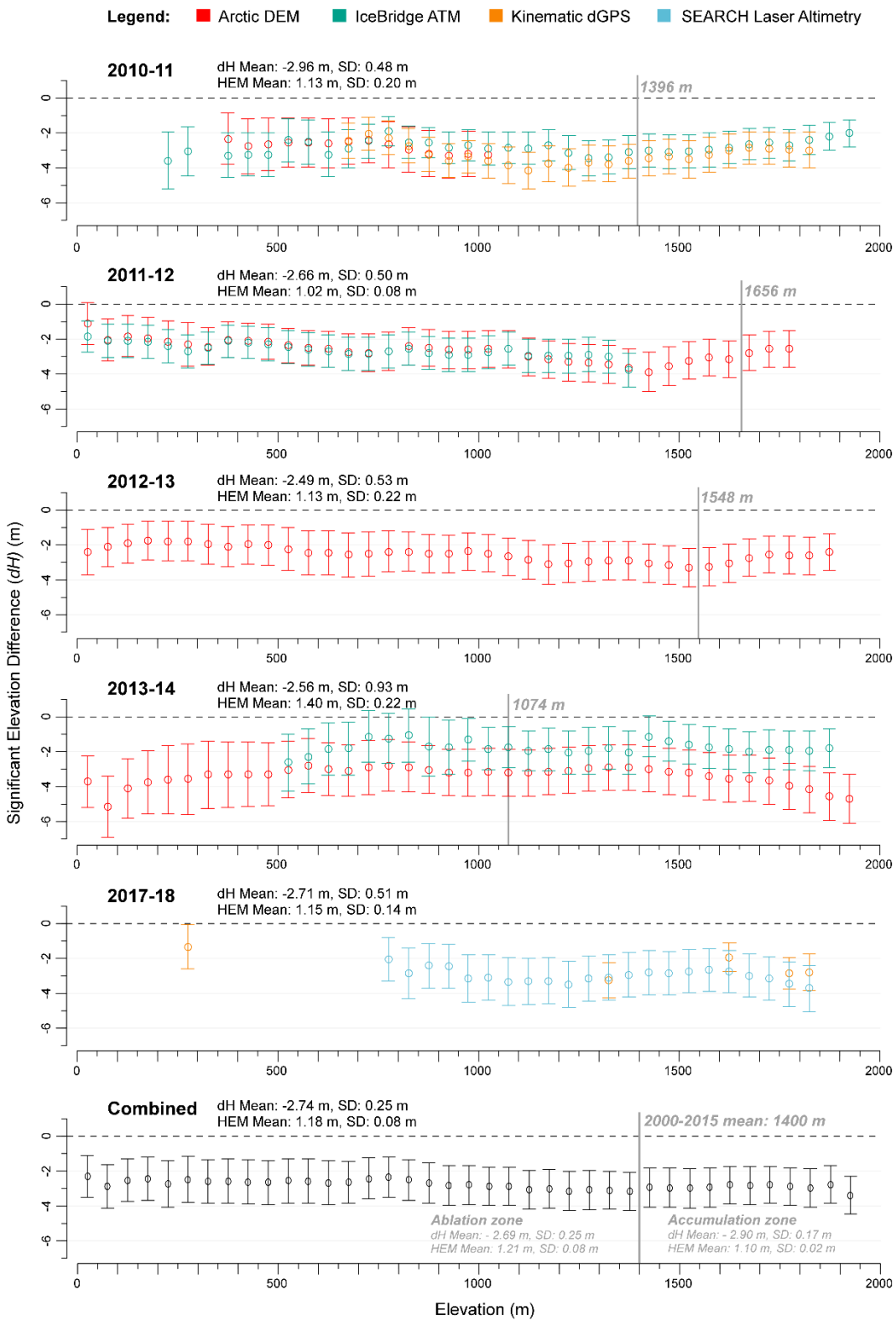

Figure 4.10 Mean elevation bias (dH) of the rawDEM data and associated error (HEM) on the ice cap per 50 m elevation band for available elevation validation datasets for all frozen season and combined. Only pixels with significant elevation bias were used. Previous summer Equilibrium Line Altitude (ELA) in grey modelled from in-situ mass balance transect on NW basin (Fig. 4.8c). Elevation extracted from 2010-14 TanDEM-X mosaic of Devon Ice Cap.

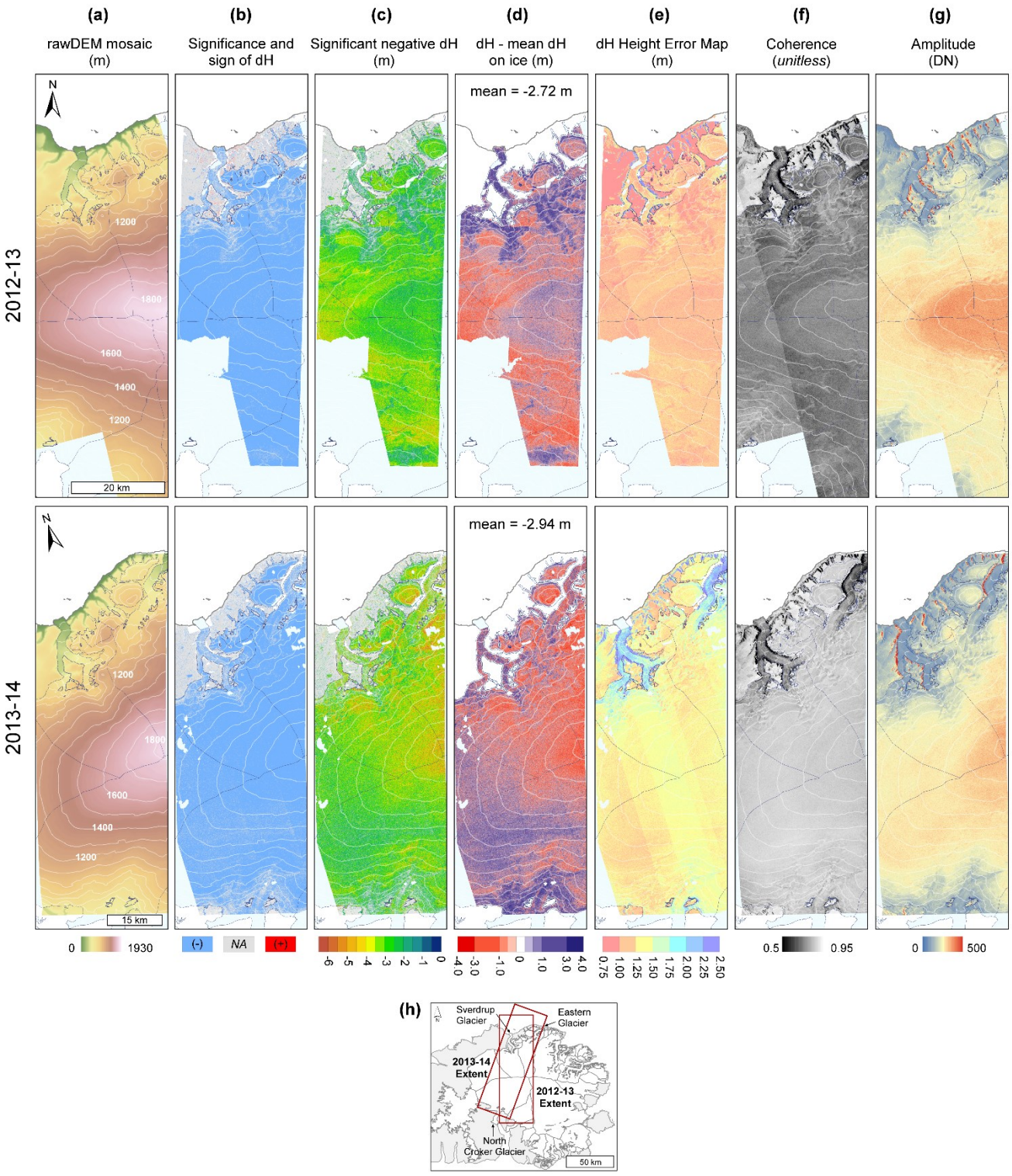

Figure 4.11 Comparison of rawDEM mosaics and ArcticDEM strip DEMs for years 2012-13 (rawDEM mosaics 2012-11-04 and 2012-11-15 with three ArcticDEM strip DEMs) and 2013-14 (rawDEM mosaic 2013-12-13 and four ArcticDEM strip DEMs). In (a) to (g) multiple rasters have been mosaicked to their mean value for visualisation purposes. Contours in white derived from the TanDEM-X 2010-14 mosaic. DIC outline shown in light blue with basin divides valid for 1999 (Burgess & Sharp, 2004). Datasets cropped to Devon Island coastline. TanDEM-X data ©DLR, 2019. (h) Map of Devon Ice Cap showing the extent of panels (a) to (g) for both years.

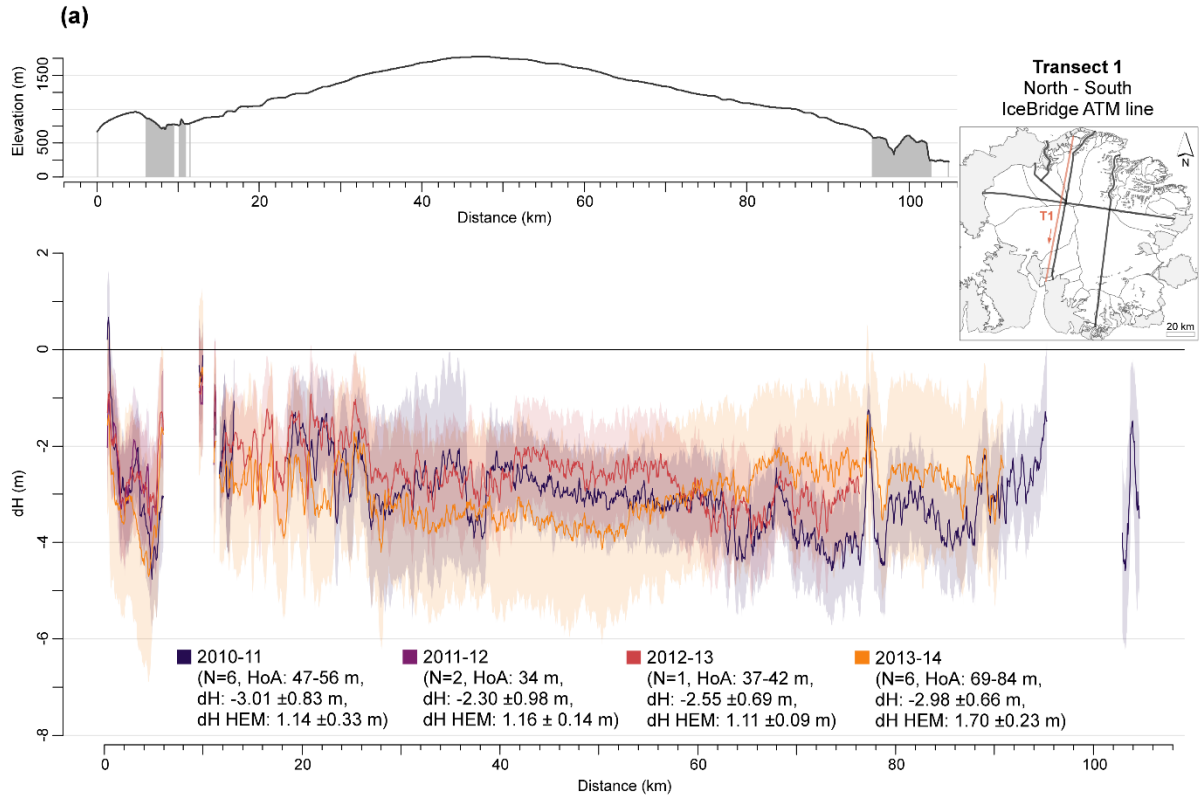

Figure 4.12 (continued on the following 3 pages): (a) Extracted elevation bias (dH) on Transect 1 across Devon Ice Cap (DIC). (top) Surface elevation profile of the transect extracted from TanDEM-X 2010-14 mosaic. Bedrock areas shaded in grey. (top right) Map of DIC showing the location and direction of the transect. (bottom) Elevation difference per mass balance year for all dataset types and rawDEM mosaics combined. Values extracted on ice only following the ice mask described in Section 3.2.2 at an interval of 50 m within a 25 m radial buffer. A moving average filter of window size 5 (~250 m) has been applied. Shaded area represents the average height error (dH HEM) where maximum range in error is shown when multiple values are averaged for a year. Statistics per frozen season in the legend where N is the number of datasets averaged, followed by the range in Height of Ambiguity (HoA) of the rawDEM mosaic used and by average and standard deviation of dH and dH HEM.

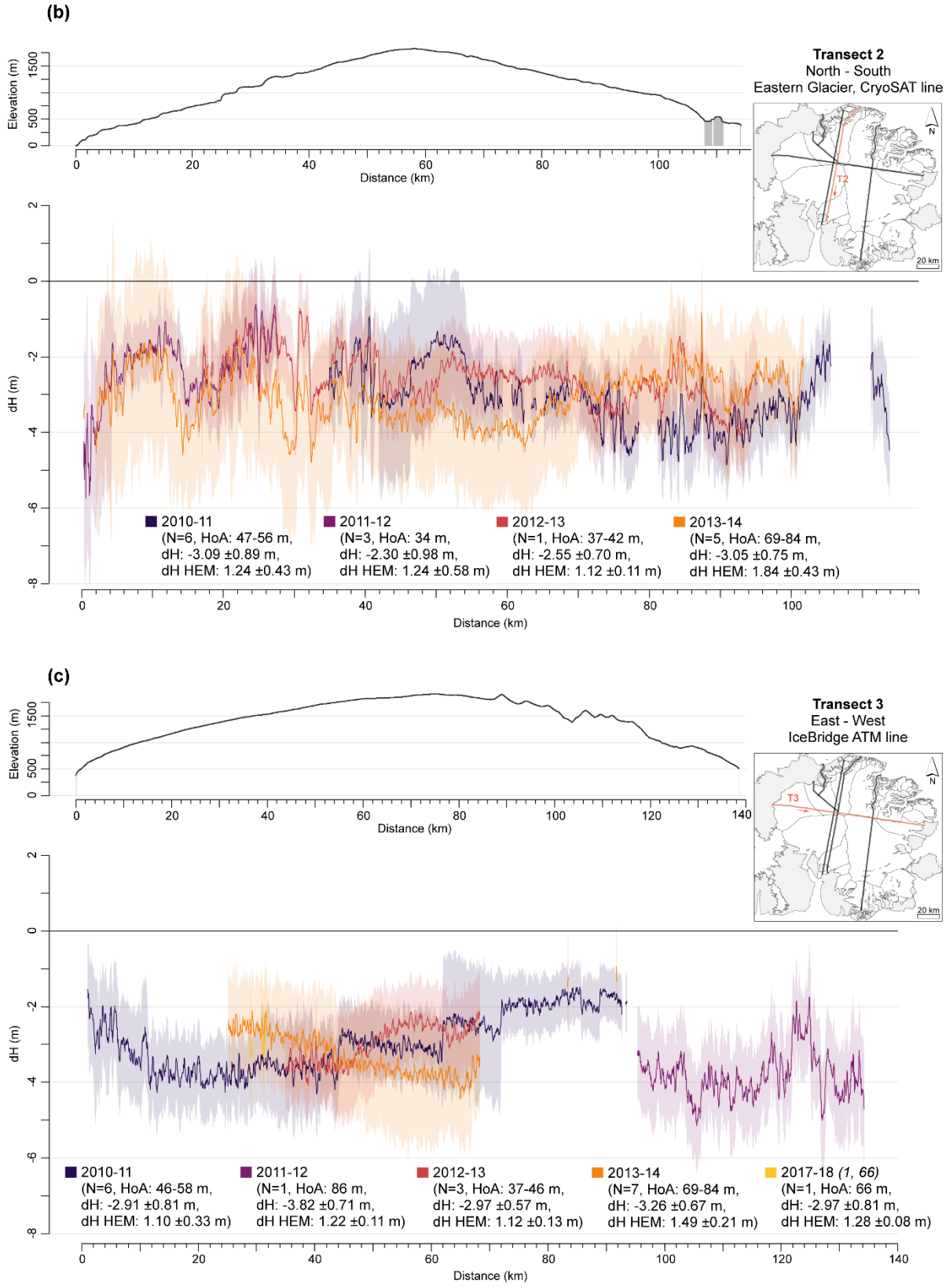

Figure 4.12 (b-c) Extracted elevation bias (dH) on Transects 2 and 3 across Devon Ice Cap. Panel descriptions as in the caption for Fig. 4.12a.

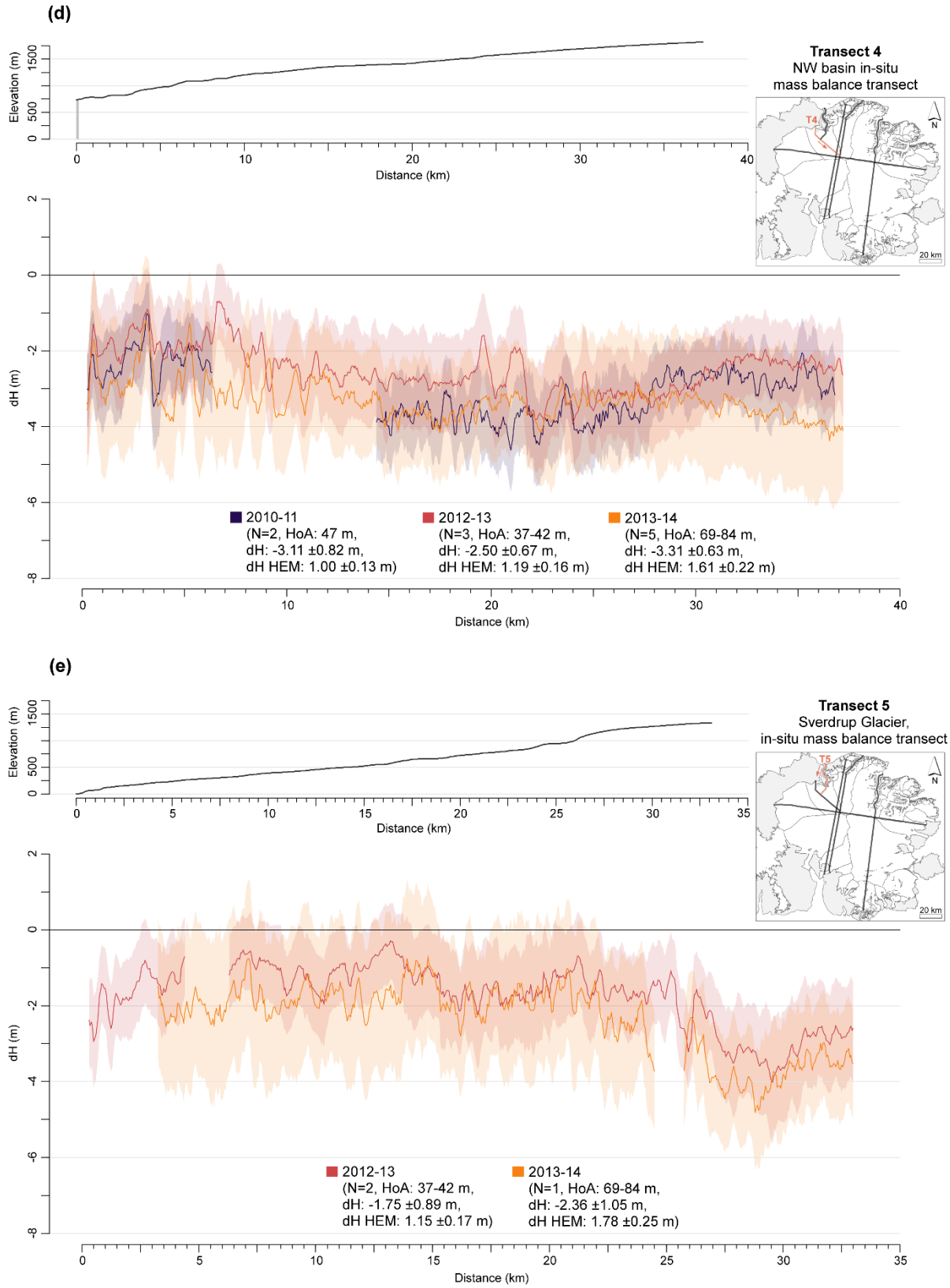

Figure 4.12 (d-e) Extracted elevation bias (dH) on Transects 4 and 5 across Devon Ice Cap. Panel descriptions as in the caption for Fig. 4.12a.

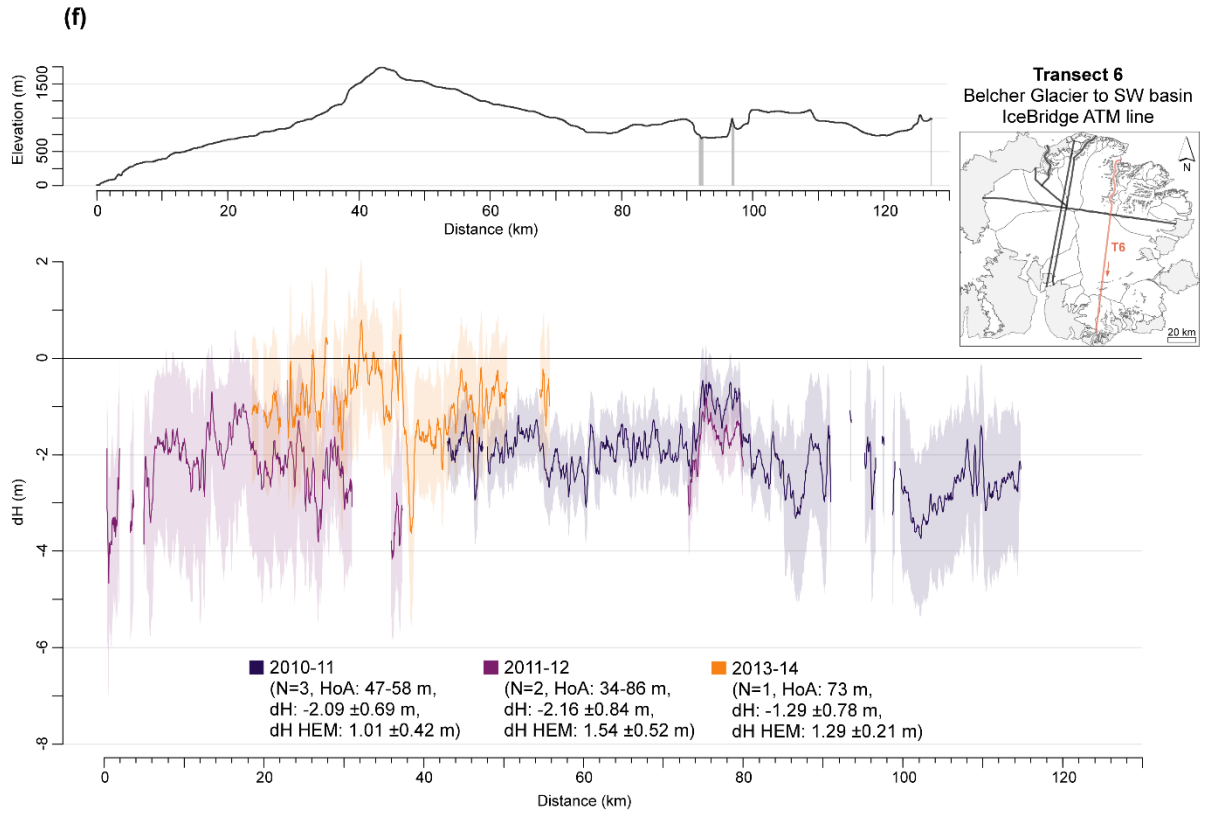

Figure 4.12 (f) Extracted elevation bias (dH) on Transect 6 across Devon Ice Cap. Panel descriptions as in the caption for Fig. 4.12a.

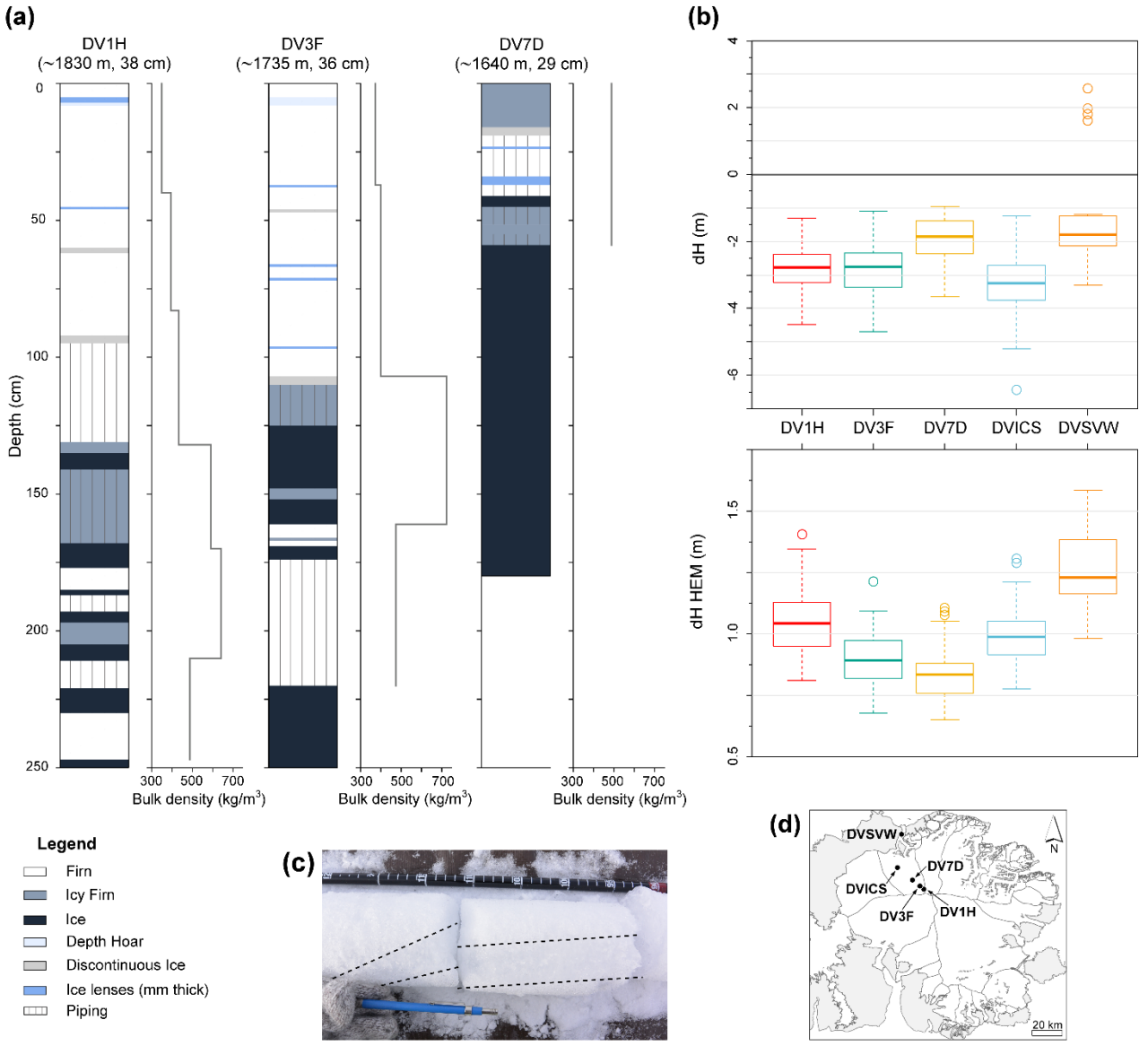

Figure 4.13 (a) Stratigraphy and bulk density of shallow firn cores collected in May 2018 near the three upper Automatic Weather Station (AWS) sites on the NW basin in-situ mass balance transect. Approximate elevation and average snowpack depth from five snow probe measurements indicated below each station name. Cores DV1H (281 cm) and DV3F (255 cm) consist of ice only beyond 250 cm. (b) Boxplots of elevation bias (dH) and associated error (dH HEM) for pixels with significant elevation bias (|dH| > dH HEM) at each 2018 dGPS transect location near the five AWS. Calculated with rawDEM mosaic 1512481_2018-07-05. (c) Visible ice piping in firn core between the dashed lines on the DV1H core. (d) Location of the five AWS and 2018 dGPS transects made in the vicinity of each AWS on Devon Ice Cap.

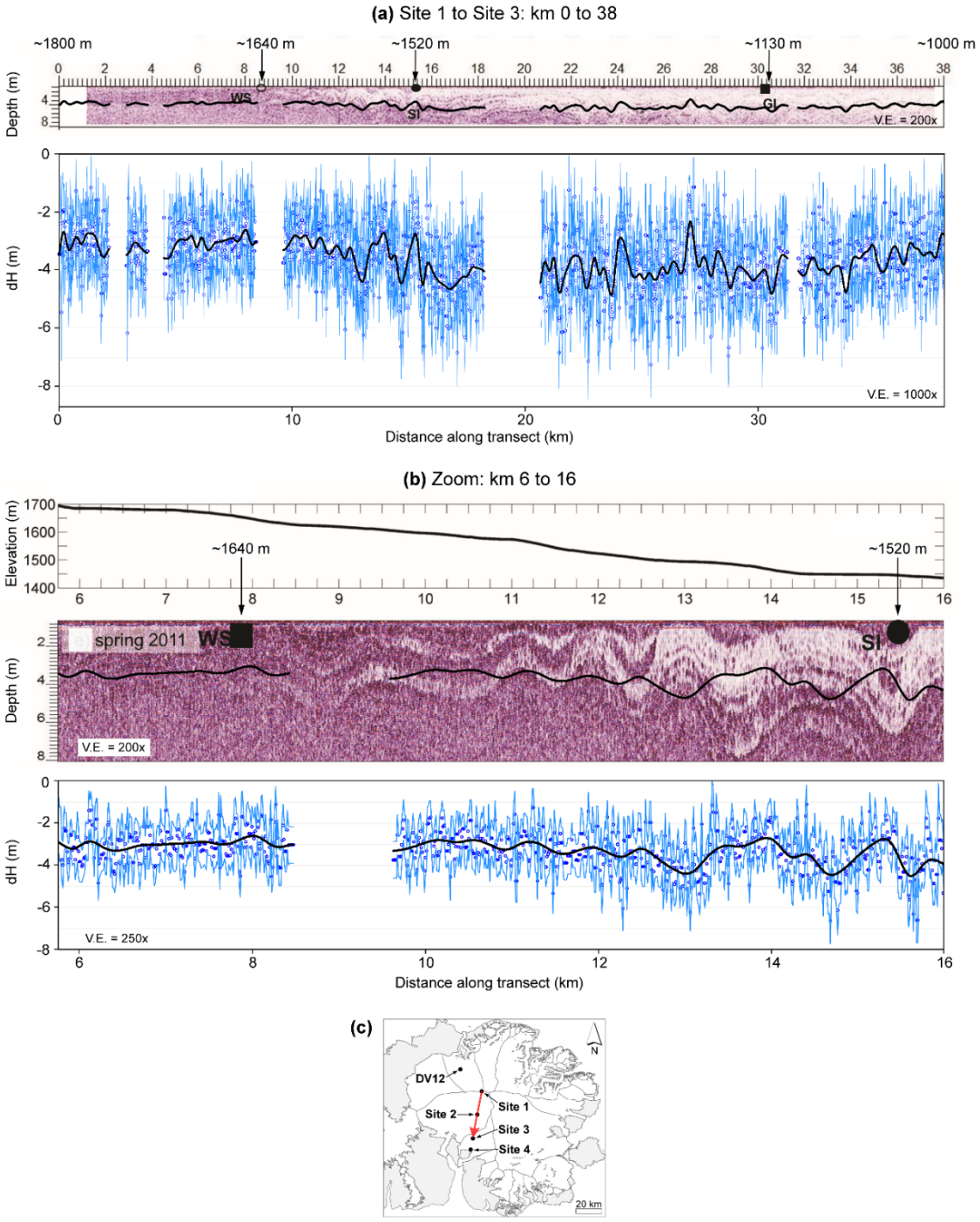

Figure 4.14 (a, b) Comparison of ground penetrating radar (GPR) profiles acquired in spring 2011 by Gascon et al. (2013) and elevation bias between 2010-12-12 TanDEM-X rawDEM and dGPS data from spring 2011. White layers in the GPR profile represent ice and purple signatures represent firn. Upper boundaries of snow facies from Gascon et al. (2013) shown in the GPR profile: wet snow zone (WS) or saturation zone, superimposed ice zone (SI) and glacier ice (bare ice) zone (GI). Black line is a spline fit of elevation bias values (blue points). Error bars are plotted as lines in light blue. (c) Location of GPR transect from Site 1 to Site 3 on the CryoSat line on Devon Ice Cap.

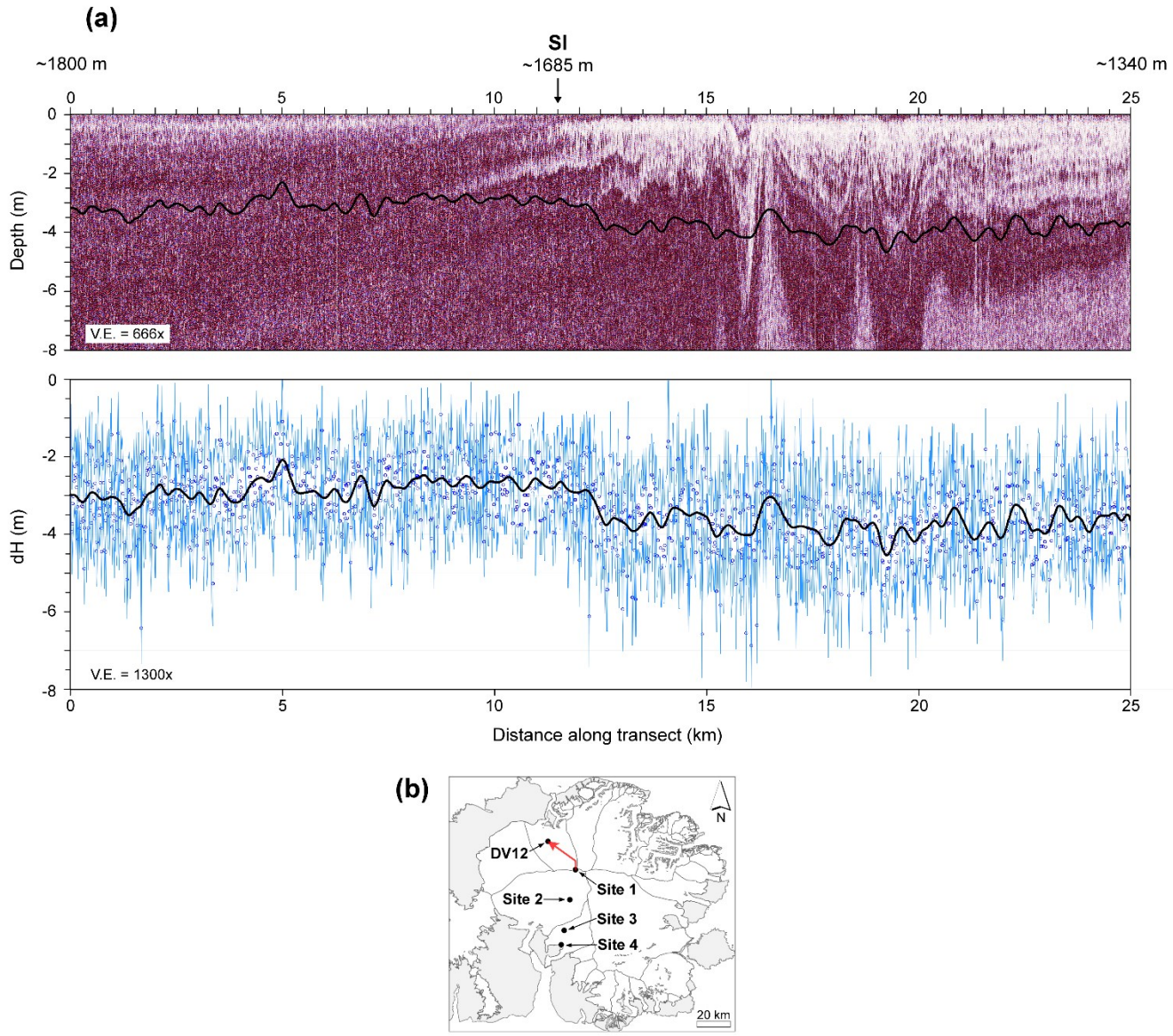

Figure 4.15 (a) Comparison of ground penetrating radar (GPR) profile acquired in spring 2011 by De Jong (2013) and elevation bias between 2010-12-12 TanDEM-X rawDEM and dGPS data from spring 2011. White layers in the GPR profile represent ice and purple signatures represent firn. Upper superimposed ice limit (SI) as defined by De Jong (2013) and elevation are indicated on top. Black line is a spline fit of elevation bias values (blue points). Error bars are plotted as lines in light blue. (b) Location of GPR transect from Site 1 in the CryoSat line to pole DV12 of the in-situ mass-balance transect on Devon Ice Cap.

Chapter 5: Discussion and Conclusion

In this chapter we discuss the implications of our results for the validation of TanDEM-X rawDEMs and relate them to the literature. We first discuss our assumption that no significant change occurs on the ice cap surface from fall to spring and that we can use rawDEMs from the fall and winter months to calculate elevation bias with validation elevation datasets from the spring. Then we discuss the elevation bias as seen on stable terrain and on the ice cap, including the effects of SAR acquisition parameters. We conclude with a review of the factors affecting our calculated elevation bias.

5.1 Potential Variability in TanDEM-X Derived Elevation During the Frozen Season

An underlying assumption that is investigated in this thesis is whether validation elevation datasets collected in the spring can provide an effective measure of the elevation bias in the rawDEMs collected at a different time in the same frozen season. From the combination of backscatter and snowpack depth variability, together with vertical velocity data, we estimate that surface elevation change during a single frozen season on DIC is typically below 0.50 m. This estimate is conservative because the largest snowpack depth variability and thinning and thickening values extracted from Burgess and Sharp (2008) were used to estimate vertical velocity. This maximum bias of 0.50 m is valid for only two rawDEMs with a separation of 6 months from the acquisition time of the validation elevation datasets, as all the others had a difference of <5 months. A surface elevation change <~0.50 m is lower than the HEM of rawDEMs over DIC, even for acquisitions with the largest HoA and increased coherence. The validation of elevation bias in the TanDEM-X DEMs over the ice cap yields average values of ~-3 m and maximum values of up to ~-8 m at high elevation. It is therefore clear that the elevation bias caused by different acquisition times between the TanDEM-X DEMs and any elevation validation dataset is much smaller than the elevation bias related to the penetration of the radar signal into the glacier surface. This analysis provides confidence that our comparison of rawDEM surface elevation with validation data in the same frozen season is an effective way to detect elevation bias caused by the penetration of the radar signal.

5.1.1 Combination of Snowpack Depth Variability and Vertical Velocity Estimates

If we exclude the influence of backscatter variability, our reported range of potential elevation change (maximum thinning of -0.37 m and thickening of +0.46 m) depends on the multiple assumptions within each dataset and their representativeness of conditions over the entire ice cap. With knowledge of the importance of katabatic winds for snow redistribution on DIC (Koerner, 1966; Mair et al., 2005), we had hypothesized that snowpack depth would be the largest factor affecting surface elevation during the frozen season. However, our estimates for snowpack depth variability are within the same range or smaller than dynamic vertical changes (Table 4.1). Our AWS measurements and Koerner (1970a) show that most annual snowfall occurs between August and October, so variations after this period are probably mainly due to wind redistribution. Snowpack depth variability from November to May can then be as much as its thickness at high elevations and could even be double at lower elevations and in concave areas. The bimodal nature of the relative height distribution at most AWS stations suggests that significant increases or decreases in snowpack depth are related to specific wind or snow events and are not gradual.

Previous studies of the accumulation patterns on DIC reported that elevation, slope and aspect were the main three factors that explained variability (Sylvestre et al., 2013; Colgan & Sharp, 2008; Mair et al., 2005). The aspect component is related to the proximity to the North Open Water Polynya leading to increased precipitation and accumulation on the SE part of the ice cap (Koerner, 1977; Burgess et al., 2005). Extrapolating snowpack depth from the NW basin to the entire ice cap is clearly not representative, but our dataset represents variability in snowpack depth following the main snowfall period. Hence, we judge that variability between 5 and 21 cm for the November to May period are realistic average values for the entire ice cap.

Estimates of dynamic thinning or thickening reported in Burgess and Sharp (2008) vary greatly in sign and magnitude across the different basins of DIC and Table 4.1 already provides a summary of these. Calculation of the background thinning and thickening rates using the flux divergence method was done using multiple datasets, but care was taken to adjust them to obtain values representative of accumulation and ablation trends in different basins. Since the datasets of Burgess and Sharp (2008) were representative of the long-term trends for 1960-2000, it is possible that these have changed since 2000 given the notable increase in mass loss and gradual increase in ELA since 2005, as seen in the in-situ mass balance record (Fig. 4.8). However, the study of

Burgess and Sharp (2008) is the only source that reported dynamic vertical changes that differentiated between basins and the accumulation and ablation zones. We are therefore constrained in assuming that the range of values we used (-0.23 to 0 m w.e. a^{-1} in the accumulation zone and -0.36 to +0.55 m w.e. a^{-1} in the ablation zone) is still representative of the conditions on the ice cap for the period of this study (2010-2018).

Another parameter that could influence real and perceived elevation change during the frozen season is horizontal surface velocity. Surface velocity could influence interferometrically-derived elevation if it is high enough to "move" the subsurface more than one pixel away, changing the elevation of each pixel and the horizontal location of the subsurface scatterers. Reported velocities for the ice cap interior are low at <20 m a^{-1} (Van Wychen et al, 2017), corresponding to less than a pixel change in the rawDEMs over 6 months (10 m). In the upper reaches and on valley glaciers, velocities gradually increase from 25 m a^{-1} to 150 m a^{-1} and can reach up to 300 m a^{-1} near the terminus of some glaciers (Van Wychen et al., 2017). Surface velocities are generally 11-19% lower during the frozen season compared to the summer, when enhanced flow due to melting conditions is present. Surface elevation differences during the frozen season due to horizontal surface velocities are therefore likely in valley glaciers and could be positive or negative and on the order of 10's of centimeters to meters. However, elevation bias is typically non-significant in these areas in the rawDEMs due to a rougher surface and the presence of supraglacial debris, leading to lower volume scattering. This potential bias will be considered when discussing calculated elevation bias in the bare ice zone, but can be assumed to be negligible in the other glacier facies at higher elevations. As most of our validation elevation datasets cover the ice cap interior and because the quantification of this bias during the frozen season has not been reported, we did not include it in our estimates reported in Table. 4.1.

5.1.2 Backscatter Variability in Wide ScanSAR Scenes

In relation to the evolution of backscatter on DIC during the frozen season, our methodology enabled us to detect some variability even with a conservative radiometric resolution of 0.84 dB. Analysis of two frozen seasons with different surface conditions revealed that the mean ice cap backscatter varies <0.5 dB from October to May, with on-ice per pixel variability below 3.5 dB. Even if we cannot transfer this variability to a direct effect on interferometrically-derived surface height, we deduce that the sign of this bias would be negative. The variability of backscatter on

the ice cap during the winter months of ±3 dB presented in Figure 4.3a likely reflects seasonal changes in moisture content and temperature of the snowpack and upper layers of firn. As the snowpack gets gradually thicker and air temperatures colder, from October through March, there is a net loss of moisture in the snowpack and upper layers of firn as constructive metamorphism occurs and hoar crystals are formed at depth (Sommerfeld & LaChapelle, 1970). During this period, an increase in mean backscatter is seen on the ice cap which directly reflects changes in snowpack properties, which seem to be independent of elevation or facies location. From a transect of snow pits along the CryoSat line in 2004 and 2006, Bell et al. (2008) reported a low-density hoar layer at the bottom of the snowpack along the totality of their transect and similar layers were detected in our snow pits on the NW basin in spring 2018. An increase in grain size, layering and potentially snow depth as the winter progresses increases volume scattering (Garrity, 1992), increasing total backscatter. This would result in larger volume decorrelation affecting the quality of SAR interferometry due to lower coherence and higher height error, leading to a potentially larger negative elevation bias. As the sun comes back in early spring and the snowpack warms up to the freezing point, moisture content increases and volume scattering decreases which negatively influences backscatter intensity (Snehmani et al., 2015; Tsai et al., 2019) and positively influences interferometric coherence. From these observations, we suggest that the seasonal cycle of the snowpack most likely influences interferometrically derived surface height negatively, potentially on the order of a few cm to 10s of cm, and that this bias is highest in the coldest time of winter when stronger volume scattering occurs. Variability in backscatter on DIC for the frozen season from QuikSCAT Ku-band scatterometer can be estimated from data presented in Figure 9 in Wolken et al. (2009) along the CryoSat transect from 1999 to 2007 and in Figure 5 in Casey and Kelly (2010) for each facies zones from 2004 to 2006. In both studies the variability in backscatter is not quantified, but from interpretation of their figures it seems to be between 2 and 3 dB when no melt is occurring, agreeing with our value.

Our observations using the Wide ScanSAR product are not exactly comparable to the Stripmap acquisition method for the creation of TanDEM-X DEMs due to different ranges in incidence angles. By looking at the GIM over the water surrounding the ice cap for the Wide ScanSAR scenes, incidence angles range from ~22 to 35° over DIC compared to ~37 to 44° for the Stripmap scenes (Table 3.1). As backscatter is also a function of incidence angle (Snehmani et al., 2015 and Eq. 3.5), our analysis of backscatter evolution during the frozen season likely would

have given slightly different results for the Stripmap mode but we assume that relative differences would be similar. The environmental variability of ±3 dB detected in the frozen season would likely be reduced with a higher resolution imaging mode such as in the Stripmap mode (radiometric resolution of 0.6 dB (Fritz & Eineder, 2013)). The Wide ScanSAR product was chosen as it covered the entire ice cap in one scene and was available at short repeat intervals for two consecutive frozen seasons. The appearance of a banding pattern in the Wide ScanSAR images due to the combination of multiple swaths (Fig. 4.2) reveals that this product is not suited for accurate detection and quantification of backscatter change because radiometric resolution was clearly lower where more information was acquired. Further, considering the magnitude of backscatter decrease when melt occurs (~-20 dB), we are confident of our assumption that the environmental variability of ±3 dB has a negligible impact on TanDEM-X derived surface elevation.

5.2 Validation of TanDEM-X RawDEMs on Stable Terrain (Off-Ice Cap)

Our validation of TanDEM-X rawDEMs over stable terrain with IceBridge ATM data revealed a relative accuracy of 1.54 m at the 90% confidence interval, which was reduced to 1.21 m when only considering slopes ≤20° and HEM ≤1 m. Both of these values are lower than the reported relative accuracy in the global TanDEM-X mosaic product (≤ 2m for slopes ≤ 20° at the 90% confidence level, Wessel (2016)), which was confirmed by comparison with GPS data in Wessel et al. (2018). The positive correlation between HEM and elevation bias over stable terrain supports our use of pixels with HEM ≤1 m for the ArcticDEM co-registration and the ground truth of the SEARCH data.

The consideration of slope and HEM did not influence the negative mean height error of 0.29 m over stable terrain, but lowered the RMSE from 0.9 m to 0.8 m (Table 4.2). The magnitude of our mean height error is similar to what was observed over forested areas by Wessel et al. (2018) where height error was higher due to volume decorrelation: +0.37 m over forested areas compared to +0.13 m for developed areas and -0.02 m for low vegetation areas. Our comparison on "stable terrain" (off ice cap and perennial snow patches) was undertaken for data acquired during the frozen season, so the presence of snow could explain this slight negative mean bias. A more in-

depth analysis could be completed by selecting pixels with little or no snow cover identified from high-resolution satellite images, as was done for the ground truthing of the SEARCH data.

Our dataset suggests that the block adjustment procedure using select ICESat points to process the rawDEMs (detailed in Chapter 3, Section 3.1) improves the relative height accuracy of the rawDEMs. The vertical displacement applied on the four rawDEMs that were compared with the IceBridge ATM data (-0.455 m, -1.751 m, -2.759 m and -2.268 m from Table 3.1) are higher than the RMSE and bias at the 90% confidence interval for three out of the four DEMs. Not applying these offsets would have worsened the mean elevation bias over stable terrain by ~2 m. For the creation of the global TanDEM-X mosaic product, a specific block adjustment procedure was developed to minimize elevation bias over Greenland and Antarctica using tie points from coastal regions (stable terrain) and calibrating the DEMs in an outer-to-inner fashion (Wessel et al., 2016; Rizzoli et al., 2017a). Compared to adjustment blocks over Greenland which include multiple snow facies (Wessel et al., 2016), a large portion of terrain not covered by glaciers is present in the areas of the adjustment blocks over the Canadian Arctic (Fig. 3.1), as would be the case for other glacierized regions outside the ice sheets. This makes the current calibration method satisfactory over glacierized terrain, but the presence of snow during some of ICESat and rawDEM acquisitions will always contribute to the presence of a certain bias.

5.3 Validation of TanDEM-X RawDEMs on Devon Ice Cap

5.3.1 Influence of SAR Acquisition Parameters on Elevation Bias on Glacierized Terrain and Implication for Modelling

The influence of SAR acquisition parameters on elevation bias was investigated by comparing the differences in elevation (dH) from pairs of dH rasters with identical ground conditions but with different baseline, HoA, mean coherence and mean amplitude. Our dataset shows that a change in perpendicular baseline and by default of HoA that is >5m could lead to a change in the mean elevation bias in a rawDEM of ~±2 m without any change on the glacier surface. This effect could be significant considering it is of the same magnitude as the relative vertical accuracy of the TanDEM-X global mosaic product (≤2m for slopes ≤20° at the 90% confidence level (Wessel, 2016)).

As was reported by Abdullahi et al. (2018), our results show that HoA and coherence are positively correlated (Fig. 4.9a). The relationship between HoA and volume decorrelation over glacierized terrain has been reported by Martone et al. (2016), Rizzoli et al. (2017b) and Hoen and Zebker (2000) in their investigations of glacier facies on Greenland based on the volume decorrelation component isolated from total coherence in interferograms. Facies of the Greenland Ice Sheet have been successfully classified using only backscatter intensity and volume decorrelation from TanDEM-X data by Rizzoli et al. (2017b). The latter is the most relevant factor affecting decorrelation for terrain where large volume scattering occurs. This explains why an optimal acquisition geometry with smaller baselines (larger HoAs) was favoured over Greenland and Antarctica for the TanDEM-X acquisitions, because of the large potential for loss of coherence due to volume scattering over glacierized terrain (Rizzoli et al., 2017a).

As mentioned in Section 4.3.1, the relationship between coherence, baseline and HoA with elevation bias is more complex and our dataset is too small (N = 13) to define it precisely. Our observations still agree with Abdullahi et al. (2018), who compared ICESat points with multiple rawDEMs acquired over Greenland. It seems that for similar ground conditions, the sign of the change in elevation bias is dependent on the magnitude of the change in baseline and HoA. For a small increase in HoA (between 5 and 10 m), our results suggest that coherence is improved and that this reduces the depth of the mean phase center, yielding a decrease in elevation bias. The inverse occurs for a larger change in HoA (>10 m), suggesting that the geometric configuration of the acquisition (effect of baseline and HoA) increases the depth of the mean phase center more on average than it could be reduced by the increase in coherence, thus increasing elevation bias. This relationship could be further complicated by the dominant scattering mechanisms in different glacier facies, but investigating it in a detailed manner goes beyond the scope of this project. A starting point to investigate this relationship could be the study by Dall (2007) who showed that for a uniform volume with infinite penetration depth and negligible surface scattering, the ratio of elevation bias to HoA depends only on the ratio of penetration depth to HoA and that the elevation bias can be expressed in terms of coherence magnitude.

Nevertheless, our results highlight that HoA and/or baseline must be included as a parameter in the modelling of elevation bias in glacierized terrain in order to develop a model applicable to the complete range of HoA for all rawDEMs acquired on glacierized terrain. This is especially important for rawDEMs on glacierized terrain outside the ice sheets (e.g., in the Canadian Arctic),

for which acquisitions at smaller baselines were not necessarily favoured. A similar conclusion was found by Abdullahi et al. (2018), who argued that the applicability of a model at a larger scale needs to include HoA, along with coherence and backscatter intensity. Testing of more complex non-linear models to capture their relationship with elevation bias without the input of field based measurements was also proposed. As mentioned by Rizzoli et al. (2017b), we suggest that the volume decorrelation factor, as isolated from the coherence, could also provide more information to help in the modelling of the elevation bias.

5.3.2 Detection of Spatiotemporal Patterns of Elevation Bias on Devon Ice Cap

Our investigation of the spatiotemporal patterns in elevation bias on DIC reveal that it can occur at all elevations, averages -2.74 ±0.25 m and typically ranges between 0 and -5 m for all frozen seasons, glacier facies and rawDEMs combined (Fig. 4.10). This average value is in on the lower side of values found of ~3-7 m in previous studies in the percolation and saturation zone for the Greenland Ice Sheet, the Antarctic Peninsula and high mountainous terrain in the Karakoram using TanDEM-X data (see Section 2.4). We have considered both the height error (HEM) of the rawDEMs and the height errors of our validation datasets and still detected some elevation bias significantly different from zero across the entire elevation range of DIC. The comparison with the NW basin ELA from the updated in-situ mass balance transect and with the subsurface data provided by the GPR transects, shallow firn cores and facies boundaries identified in the previous literature helped us constrain the general elevation bias pattern of different facies.

As was mentioned in Chapter 2, the dry snow zone is intermittent on DIC and melt has been detected on the entire ice cap in summers 2009 to 2015 (Mortimer et al., 2016). Hence, a dry snow zone like that detected in SAR data from Greenland was not present on DIC during our study period.

In our dataset we can differentiate the percolation zone from the saturation zone due to the lower variability in elevation bias in the percolation zone. This is most clear in the comparison of elevation bias in the GPR transects from 2010-11 in Figure 4.14 and 4.15 but can also be observed from the lower standard deviations in 2018 dGPS transects at DV1H (~1830 m a.s.l.) and DV3F (~1735 m a.s.l.) compared to DICS (~1335 m a.s.l.) on the NW basin and from our mosaicking of ArcticDEM datasets in Figure 4.11 in 2012-13. As seen in transects 1 to 3 (Fig. 4.12a to c), the elevation bias at highest elevations (>~1500 m a.s.l.), which in most cases comprises the

percolation zone, is generally between -2 and -4 m with a range of ~1 m. At lower elevations, in the saturation and superimposed ice zones, we observed an elevation bias of approximately -1 to -5 m with a range of ~2 m. We combined the saturation and the superimposed ice zones in our detection of elevation bias pattern as they seem to be similar based on our analysis of subsurface data from the GPR profiles (Fig. 4.14 and 4.15).

In the percolation zone, we can expect a high backscatter due to the presence of melt features acting as subsurface scatterers and medium coherence as some volume scattering occurs (Casey & Kelly, 2010; Rizzoli et al., 2017b). This is exactly what is seen in Figure 4.11f and g in 2012-13 above ~1600 m a.s.l., which is above the NW basin modeled ELA of ~1548 m a.s.l. from the previous summer. In the saturation zone below, backscatter is lower and more heterogeneous due to the presence of larger scatterers as larger melt features and thick ice layers closer to the surface reduce volume scattering. Greater backscatter heterogeneity in this zone leads to greater variability in coherence, and larger variability in the localization of the mean phase center. This increase in variability in the saturation zone compared to the percolation zone is also visible in the elevation differences, coherence and backscatter presented in Abdullahi et al. (2018) for northwest Greenland using TanDEM-X rawDEMs. In their results, the average elevation bias in these zones was between -3 and -5 m, but the variability was doubled in the saturation zone. Larger variability in the saturation zone compared to the percolation zone can also be seen in the results of Dall et al. (2001) and Rizzoli et al. (2017b) in Greenland.

Previous studies have shown that radar signal can penetrate a bare ice surface and that a negative elevation bias can be detected in the bare ice zone (e.g., Rignot et al., 2001; Zhao & Floricioiu, 2017). On DIC, most of the pixels with non-significant elevation bias were located in the bare ice zone even if the rawDEM height error was generally higher on valley glaciers due to a rougher terrain, presence of moraines, crevasses and supraglacial channels. We have calculated that elevation bias below 1000 m a.s.l. was significantly lower by ~40 cm and height error was significantly higher by ~23 cm compared to that above this elevation (Section 4.4.2). The bare ice zone does extend above 1000 m a.s.l., but this elevation is generally the boundary where ice transitions from the main ice cap dome into the valley glaciers where rougher terrain occurs. This pattern was best observed in transects 4 and 5 (Fig. 4.12d and f), where non-significant bias was detected at lower elevations but variations were large and then elevation bias became more

significant above ~1000 m a.s.l. Overall, in the bare ice zone significant elevation bias was typically less than the ice cap average, and this was also the only zone where significant positive elevation bias was detected (Fig. 4.11b). Presence of positive elevation bias in the bare ice zone was also reported by Abdullahi et al. (2018) in Greenland during the winter and by Zhao and Floricioiu (2017) in Antarctica over bare blue ice, but in both studies the bias was less than the accuracy of the TanDEM-X DEMs (≤2 m) and can be judged non-significant.

We have also linked areas of the bare ice zone with lower elevation biases than their surroundings in the upper reaches of glaciers, to areas of faster flowing ice as identified in Van Wychen et al. (2012, 2017). These areas are generally characterized by larger slopes as the ice accelerates as it flows from the main ice cap dome into valleys. Slope has been identified as an important parameter affecting TanDEM-X elevation bias (Gardelle et al., 2012a; Pandey et al., 2016) due to its effect on local incidence angle of the radar signal. Faster flowing areas probably also exhibit a smoother ice surface below the snowpack as coherence is higher but backscatter is lower on average (Fig. 4.11, 2012-13). Ice crystal orientation and bubble content are two other factors that might have a greater impact than slope and surface roughness on the elevation bias, but their influence can't be quantified without field data. Slight differences in ice density and impurity content could also impact backscatter properties of these areas. The relationship between slope, surface roughness, crystal orientation, ice bubble content and the elevation bias would benefit from being investigated further as it could bring new insights to understand the high variability in the bare ice zone, even if the average elevation bias is non-significant.

It is important to acknowledge that out of the four validation elevation datasets used in this study only two, the IceBridge ATM and ground dGPS points, could be used directly and qualify as completely independent validation datasets. The calibration performed on the ArcticDEM and on the SEARCH data involves potential further bias in the calculation of elevation difference. However, the calculation of elevation bias with the ArcticDEM makes it possible to visualize its spatial variability, even if this dataset is the least precise due to higher height error from co-registration with the rawDEMs. An apparent change in elevation bias pattern across the ice cap before and after the cool summer of 2013 was mentioned in Chapter 3 (seen in Fig. 4.11) and could have been overlooked in our transects (Fig. 4.14) due to the overlap of the error margins for all frozen seasons. The occurrence of an abnormally cool summer in 2013 (Mortimer et al., 2016), has caused an apparent increase in the elevation bias in the percolation zone and potentially in the

upper saturation zone. Considering that the snowpack experienced less melt during this cool summer, a thicker snow cover with fewer and smaller melt features than usual would have been left on the surface before the next frozen season started and new snow fell. A thicker snowpack above the firn or ice surface would cause an increase in volume scattering and hence in volume decorrelation, leading to the localization of the mean phase center even deeper below the surface. This would result in an increased elevation bias in the rawDEMs.

Availability of datasets and their coverage is a major factor affecting the ability to detect spatiotemporal patterns in elevation bias across DIC in this study. Enough data was available to validate the rawDEM elevations and quantify the general pattern of elevation bias in glacier facies even with the complicating effect of differing HoAs in the rawDEM acquisitions. However, due to the location of overlap of rawDEMs with the validation elevation datasets (Fig. 3.3), our analysis has focused on the western, central and northern parts of the ice cap, which prevents us from providing comprehensive conclusions concerning temporal changes in elevation bias at the ice cap scale. One way to undertake future more detailed analysis would be to compare elevation bias patterns with high-resolution optical satellite images acquired during the summer and the winter to link surface features such as crevasses, surface undulations, melt ponds and channels, and presence of supraglacial debris to calculated elevation bias.

One parameter that has not been discussed yet is the occurrence of melt and the start of the melt season. Based on the study of melt duration and melt extent in the Queen Elizabeth Islands from 1999 to 2005 by Wang et al. (2005), we assumed that no significant melt occurred before the start of June and after September in our study period from 2010 to 2018. The occurrence of a melt event creating liquid water in the snowpack, decreasing backscatter and lowering the elevation bias for the surface elevation to be closer to the "true" surface during our frozen season (November to May) is unlikely, but not impossible. In addition, as melt duration is negatively correlated with elevation (Wang et al., 2005), such an event would probably only affect lower elevations of the ice cap where elevation bias is on average non-significant. There is only one dataset that could have been significantly affected by melt, which is the SEARCH dataset acquired in late May to early June. However, observation of the "quick-look" Wide ScanSAR scenes of DIC from this period reveals that widespread melt didn't start until June 8-19, 2018.

5.4 Summary of Presented Factors Affecting Surface Elevation on Devon Ice Cap

A large part of the validation of the surface elevation of TanDEM-X rawDEMs in this study has been to quantify the factors that could affect the detection of a significant elevation bias. In Table 5.1 we review the factors discussed above and their influence on our calculated elevation differences. As expected, the largest uncertainties are caused by a change in baseline, HoA, coherence and by the rawDEM height error, which is derived from HoA and coherence (Eq. 3.1). Caution should be taken when comparing elevation bias over DIC derived from rawDEMs of different acquisition times with HoA that differ by ≥5 m as our data shows that individual values could be biased by as much as ~2 m. This explains why we are unable to detect significant temporal variations in the elevation bias patterns in our extracted transects in Figure 4.12 as the error margins composed of all the contributing rawDEMs can span a range as large as ~4 m. By accepting that no temporal variation could be detected, the analysis of all the rawDEMs with different SAR acquisition parameters still enabled us to estimate average elevation bias and its variability in three distinct glacier facies. The percolation zone and the saturation/superimposed ice zone have an average bias of -2.90 ±0.17 m (Fig. 4.10), but variability is doubled in the saturation zone (range of ~2 m) compared to the percolation zone (range of ~1 m). In the bare ice zone, significant elevation differences are slightly lower at -2.69 m with a larger standard deviation of 0.25 m. However, on most pixels in this zone, especially below ~1000 m a.s.l. on valley glaciers, the calculated elevation difference is not significantly different from zero. As discussed above, the magnitude of these elevation biases agree with previous studies using TanDEM-X DEMs. We are therefore confident that the elevation biases we have calculated on DIC are due to the localization of the mean phase center below the true surface related to the penetration of the X-band radar signal into the glacier surface, and not due to physical change in the surface elevation during the frozen season (November to May).

Table 5.1 Summary of the parameters influencing the validation of the surface elevation in TanDEM-X rawDEMs over Devon Ice Cap during the frozen seasons (November to May) discussed in this study.

Parameter	Description of the investigation in this study	Magnitude of induced elevation bias	Sign of induced elevation bias
Backscatter Intensity (Amplitude)	Variability during from October to May in Wide ScanSAR scenes, entire ice cap	10's of cm	(-)
Snowpack Depth	Variability during the frozen season from relative surface height change measurements, Automatic Weather Stations, NW basin	~0.05 m to ~0.21 cm	(±)
Ice Dynamics: background vertical velocity	Combination from estimates in the literature, mainly from Burgess and Sharp (2008)	<0.5 m	Accumulation zone: (-) Ablation zone: (±)
Height of Ambiguity, Perpendicular Baseline and Coherence	Comparison between elevation difference (dH) raster pairs from the same frozen season with same ground conditions	≤2 m	(±)
TanDEM-X rawDEM Height Error (HEM)	As supplied in the auxiliary rasters with each rawDEM	0.5 to 5 m on the ice cap, lower in the cap center, higher in valley glaciers	(±)
RawDEM Block Adjustment Procedure	Difference between rawDEMs and IceBridge ATM data over stable terrain in 2011-12 and 2013-14	Mean bias of 0.29 m	(-)

5.5 Conclusion

The main objective of this study was to validate the surface elevation of interferometrically-derived TanDEM-X DEMs of DIC in order to assess the magnitude of the elevation bias. We quantified this in the rawDEMs by comparing their surface elevations to independent elevation datasets from ArcticDEM, IceBridge ATM laser altimetry and ground differential GPS transects from frozen seasons November to May 2010-11 to 2017-18.

A significant elevation bias of -2.74 ±0.25 m on average was detected across the entire elevation range of DIC from the average of our validation datasets, with ranges from ~+3 m to ~-8 m. We were able to relate spatial patterns in elevation bias to near surface density conditions and more broadly to glacier facies, based on subsurface datasets and estimations of facies boundaries from in-situ and satellite measurements. As was expected from previously published literature, significant elevation bias mainly occurs in glacier facies on DIC where potential for volume scattering and loss of interferometric coherence is the highest: namely, in the saturation and percolation zones. On DIC, average elevation bias is statistically the same over both of these facies (-2.90 ±0.17 m), but greater variability was observed in the saturation/superimposed ice facies (range of ~2 m) compared to the percolation facies (range of ~1 m) due to greater subsurface heterogeneity in the location and size of scatterers. Our range in elevation biases in the accumulation zone agree with the general ranges of -3 to -7 m reported in other studies using TanDEM-X DEMs (Gardelle et al., 2012a; Groh et al., 2014; Seehaus et al., 2015; Rizzoli et al., 2017b, Zhao & Floricioiu, 2017). In the bare ice facies, positive as well as negative elevation biases were detected but most elevation differences calculated for this facies were below our error margins. Clearly reduced elevation bias over areas of faster flowing ice with potentially smoother surfaces, higher slopes, different ice crystal orientation and lower bubble content in the bare ice facies suggest that these factors can play an important role in the magnitude of the bias and should be investigated further in TanDEM-X DEMs of DIC. More detailed analysis could also be undertaken to compare elevation bias patterns with high-resolution optical satellite images to estimate the range in elevation bias not only by glacier facies, but by variations (spatial and temporal) in surface conditions (e.g. presence of supraglacial channels, melt ponds, debris cover and crevasses).

In this study, we have estimated multiple parameters that could have affected our ability to detect a clear elevation bias due to the localization of the mean phase center below the surface in the rawDEMs. Our results show that baseline and HoA most affect our calculated elevation biases, which prevented us from detecting clear temporal patterns on DIC. In agreement with the validation of TanDEM-X rawDEMs on the Greenland Ice Sheet and the results of the preliminary model developed by Abdullahi et al. (2018), our findings suggest that baseline, HoA and coherence can explain a large part of the variability in elevation biases detected on similar glacier surface conditions. Hence, we recommend their inclusion in a model with the goal of correcting TanDEM-X rawDEMs on glacierized terrain, especially if no preliminary assumptions or field data from which the dielectric properties of the glacier surface can be estimated are to be used.

To put our elevation biases in perspective, we provide some reflections on the reasonable timescales to calculate geodetic mass balance on DIC using TanDEM-X DEMs from various acquisition parameters. We can first perform a back-of-the-envelope calculation to estimate how much mass would be "missed" in a hypothetical TanDEM-X DEM of the ice cap if the elevation bias was ignored. If we assume an ELA of 1400 m a.s.l. defined by the 2000-2015 NW basin average, and an ice cap area of 12,794 km^2 (for 2000, excluding the SW arm, from Abdalati et al. (2004)), then ~17% of the ice cap area would be above the ELA in the 2010-14 TanDEM-X mosaic. Assuming that all pixels in the accumulation zone would have an elevation bias equal to the average reported in this study (-2.90 m), and that in the ablation zone 40% of pixels would be affected by the average bias in this zone (-2.69 m), we can use the average density of firn (600 kg m^{-3}) for the accumulation zone and of ice (900 kg m^{-3}) for the ablation zone to calculate the corresponding volume of water at the ice cap scale. With this simplified calculation, ~14 km^3 or Gt of water would be "missing" in this hypothetical TanDEM-X DEM. This mass is quite large considering that it is equivalent to the total estimated mass loss of the NW basin of the ice cap from 1960 to 2015 reported in this study, or to 50% of the yearly mass loss rate for the QEI from 1996-2015 as modelled by Noel et al. (2018). However, this volume does not necessarily equate the error due to the interferometric X-band bias if this uncorrected hypothetical TanDEM-X DEM was used to calculate geodetic mass balance for the entire ice cap.

Two current options can be envisaged for geodetic mass balance calculations on portions of DIC using the single acquisition date TanDEM-X rawDEMs from this study:

Option 1: Differencing a TanDEM-X rawDEM (uncorrected for elevation bias) with an older DEM calculated from spaceborne or airborne optical stereo photogrammetry or extrapolation of points from laser or radar altimetry.

To be able to determine the timescale over which it would be possible to detect significant elevation changes in a specific area using two DEMs, the height error of both DEMs and the lowest average annual elevation change need to be considered, which is most likely in the accumulation zone. On DIC the yearly rates of elevation change in the accumulation zone are +0.13 to +0.27 m w.e. a^{-1} (Boon et al., 2010) compared to ≥-1.00 m w.e. a^{-1} in the ablation zone (from the NW basin in-situ mass balance record and from Gray et al. (2015)). Based on our observations of relative height change from the AWS stations and from estimates in Boon et al. (2010), a realistic average accumulation rate on the ice cap (not reported in water equivalent) can be 0.25 m a^{-1}. For the TanDEM-X DEMs, the average height error due to the interferometric bias can be conservatively estimated as -3 m from the average elevation bias calculated in this study from 2010-11 to 2017-18. Then, depending on the accuracy of the older DEM being used, we can calculate some realistic timescales over which significant elevation changes in the accumulation zone of DIC could be detected. If the older DEM has a height error of ±0.5 m, then the reasonable timescale to calculate elevation change is 12 years (estimated minimum height change of ~3 m) using error propagation. For a ±1 m error it increases to 13 years (height change of ~10 m), for a ±2 m error to 15 years, and for a ±5 m error to 23 years. These errors-to-timescale relationships demonstrate that a calculation of geodetic mass balance following Option 1 would at least need the older DEM to be acquired 12 years prior to the TanDEM-X acquisition. The main complication in this option lies in the availability of such DEM (or any elevation data) which would overlap a rawDEM acquisition, preferably covering the entire elevation range of one ice cap basin, and that would fit in an appropriate error-to-timescale relationship. A dataset that would certainly fit these criteria is a DEM that could be created from the original 1960s air photos taken over DIC.

Option 2: Differencing two overlapping TanDEM-X rawDEMs (uncorrected for elevation bias) with different timestamps.

If it is assumed that the interferometric elevation bias is constant over time, it would be cancelled out when differencing two InSAR DEMs. This would then enable the geodetic mass balance to be calculated without considering this bias (e.g. Rankl and Braun (2016)). However,

our results suggest that temporal and spatial variations of this bias in TanDEM-X DEMs did occur on DIC in our study period due to changing surface conditions and migration of the facies boundaries in a changing climate. Hence, assuming that the interferometric bias is constant over time is not valid for an ice cap when: (a) extreme variations in ELA occur compared to the long-term average, and/or (b) when there is a rapidly increasing or decreasing trend in ELA . For such cases, in addition to the inherent height error of the rawDEMs used for geodetic mass balance, an error would need to be included to reflect the interannual variability of the elevation bias. For DIC this error can be estimated from the calculated standard deviation of the mean significant elevation bias in our datasets from 2010-11 to 2017-18. This corresponds to 0.17 m or 6% of the mean elevation bias, and 0.25 m or 9% of the mean elevation bias in the accumulation and ablation zones, respectively (Fig. 4.10). Using the same proportions and densities as in the back-of-the-envelope calculation above, this error alone would correspond to ±1.30 km^3 or Gt at the ice cap scale, or to ±0.15 Gt a^{-1} for the 2010-11 to 2017-18 period. This error alone could total ~15% of the annual mass loss given that previous geodetic mass balance estimates reported for DIC using various methodologies and for different time periods (see references in Section 2.5.3) have averaged ~1 Gt a^{-1}.

Another error should be budgeted for in this option if the acquisition parameters of the two rawDEMs are not similar. Following our analysis of influence of SAR acquisition parameters in Section 5.3.1, "similar" can be argued to be when ΔHoA ≤5 m for TanDEM-X DEMs. With our datasets, we estimated that changing acquisition parameters could modify the average elevation bias of ≤2 m (Table 5.1). Using again the same proportions and densities as in the back-of-the-envelope calculation above, this error could be as large as 10.28 km^3 or Gt at the ice cap scale, which is 8x higher than the internannual variability error.

As for option (1), the minimum useful timescale to calculate geodetic mass balance using only TanDEM-X DEMs on DIC is dictated by the conditions of the accumulation zone. Assuming that each rawDEM has an average height error of ~1 m over the ice cap, combining this error with the interannual variability in elevation bias of 0.17 m in the accumulation zone means that with error propagation an elevation change of only >~1.65 m can be detectable when differencing them. Considering these numbers with the estimated accumulation rate of 0.25 m a^{-1}, the minimum realistic timescale to confidently detect elevation changes over the entire elevation profile of DIC

from two rawDEMs is 7 years. This number would be one year less if the interannual variability error is omitted. In addition, if there are some significant differences in acquisition parameters of the two TanDEM-X DEMs (e.g., ΔHoA >5 m), we would caution against this calculation for a period of less than a decade considering that the additional bias can be up to 2 m (Table 5.1).

In summary, to provide confident estimates of glacier thickness change (and therefore geodetic mass balance) from TanDEM-X DEMs or other InSAR-derived DEMs, a proper assessment of their errors is required. The following can particularly help with this: (a) validation of InSAR heights against higher accuracy elevation datasets to estimate the underlying elevation bias due to signal penetration, (b) knowledge of average accumulation and ablation rates, (c) knowledge of the facies and ELA location through time, and (d) the use of InSAR DEMs with similar scene acquisition parameters or summer scenes when volume scattering is minimized.

Considering that the spatial and temporal resolution and coverage of TanDEM-X DEMs in the Canadian Arctic Archipelago is unprecedented, it becomes clear that developing a model to correct for the elevation bias in InSAR DEMs would be highly beneficial for monitoring change on glacierized terrain in this polar desert region. Two direct advantages of the availability of corrected rawDEMs on DIC would be: (1) the possibility of mosaicking neighboring rawDEMs with different acquisition parameters to produce more accurate yearly ice cap wide TanDEM-X DEMs, increasing the area over which geodetic mass balance can be calculated, and (2) reduction of the timescale required to calculate geodetic mass balance using Option 1 or 2 above.

In conclusion, the multiplicity of higher accuracy elevation datasets available for DIC and published knowledge on the evolution of near surface densities, the findings of this thesis position DIC as a valuable test site to validate and refine future iterations of elevation bias models for TanDEM-X DEMs developed at DLR. In turn, the geodetic mass balance of DIC using corrected TanDEM-X DEMs from any acquisition parameters could be computed with higher confidence over timescales of less than a decade and used to reanalyze the in-situ glaciological mass balance record.

Appendix

Table A.1 Sentinel-2 images (Level-1C) used to analyze the snow cover over stable terrain for ground truth of SEARCH data.

Mission	Date (dd/mm/yyyy)	Baseline Number	Relative Orbit	Tile Number
S2B	11/05/2018	206	127	17XMD
S2A	22/05/2018		70	T16XEJ
S2B	04/06/2018		41	T16XEJ
S2B	07/06/2018		84	T17XMD

Table A.2 Landsat 7 ETM+ images (Level-1TP) from Collection 1 used to delineate the NW basin of Devon Ice Cap in summer 2010.

Date (dd/mm/yyyy)	Path	Row
18/07/2010	39	06
18/07/2010	39	07
27/07/2010	38	06
09/07/2010	40	06
25/07/2010	40	06
26/08/2010	40	06
17/08/2010	41	06

Table A.3 Co-registration statistics for all strip ArcticDEM files used. Co-registration with RMSE > 1 m underlined and in italics.

Mass Balance Year	Raw TanDEM-X Mosaic			Strip DEM file name	Applied Shifts			Co-registration Statistics							
	Date (yyyy-mm-dd)	Path ID	Scene ID		dx	dy	dz	Mean	Median	SD	RMSE	Pixel Count	Area (km^2)	Nb. of iterations	Max. Slope
2010-11	2010-12-23	1009588	03	SETSM_W1W2_20110517_1020010013A2C900_103001000A338300_seg1	-3.272	2.218	-0.696	-0.030	0.010	0.707	0.708	69257	9.973	2	44.3
2011-12	*2012-03-24*	*1055856*	*03, 02*	*SETSM_WV01_20120511_102001001BBBF900_102001001B1D6A00_seg1*	*-1.018*	*0.186*	*1.146*	*-0.056*	*0.003*	*1.750*	*1.751*	*53154*	*7.654*	*1*	*40.9*
	2012-04-15	1073326	02, 04	SETSM_WV01_20120511_102001001BBBF900_102001001B1D6A00_seg1	-4.892	-0.956	2.255	-0.032	-0.009	0.775	0.775	67419	9.708	2	47.5
	2012-04-15	1073326	02, 04	SETSM_WV01_20120523_102001001C224E00_102001001D116600_seg3	-2.448	-3.390	1.873	-0.054	0.010	0.775	0.777	26495	3.815	2	57.0
	2012-04-15	1073326	02, 04	SETSM_WV01_20120515_102001001B3CE100_102001001B3C6A00_seg1	-2.925	0.882	2.866	-0.039	0.016	0.723	0.724	60543	8.718	2	44.2
2012-13	2012-11-04	1107811	02, 03, 04	SETSM_WV01_20130430_1020010023814400_1020010220E4300_seg1	-1.821	0.257	0.746	-0.024	0.011	0.680	0.681	195814	28.197	2	55.3
	2012-11-04	*1107811*	*02, 03, 04*	*SETSM_WV02_20130510_1030010021131C00_1030010022BBC900_seg1*	*-0.719*	*-2.738*	*-0.901*	*-0.007*	*-0.002*	*1.412*	*1.412*	*20844*	*3.002*	*2*	*55.3*
	2012-11-04	1107811	02, 03, 04	SETSM_WV02_20130527_10300100239D7100_1030010022CA4C00_seg2	-0.265	3.563	2.815	0.002	0.003	0.655	0.655	526239	75.778	2	56.6
	2012-11-15	1107810	03, 04	SETSM_WV02_20130527_10300100239D7100_1030010022CA4C00_seg2	-0.472	3.278	3.528	0.002	-0.002	0.616	0.616	283723	40.856	2	50.6
2013-14	2013-12-13	1169772	01, 02	SETSM_WV01_20140413_102001002F88D800_102001002CAB5F00_seg1	-6.393	-3.037	-1.644	-0.016	0.006	0.770	0.770	102189	14.715	2	48.3
	2013-12-13	1169772	01, 02	SETSM_WV01_20140408_102001002D9A1000_102001002B19D600_seg1	-7.829	-5.685	2.219	0.013	0.011	0.955	0.955	53224	7.664	2	46.2

2013-12-13	1169772	01, 02	SETSM_WV01_20140405_102001002C334900_102001002D6F3D00_seg1	-1.287	-2.521	-0.636	0.014	0.003	0.743	0.743	42487	6.118	2	42.4
2013-12-13	1169772	01, 02	SETSM_WV02_20140418_103001002E622700_1030010030B89500_seg1	-0.315	-1.525	3.390	-0.039	0.013	0.945	0.946	9886	1.424	2	45.3
2014-01-04	1171318	14, 13	SETSM_WV01_20140413_102001002F88D800_102001002CAB5F00_seg1	-5.128	-4.546	-1.027	-0.038	0.008	0.831	0.832	26192	3.772	2	45.9
2014-01-04	1171318	14, 13	SETSM_WV01_20140306_102001002C7B9C00_102001002A8EE400_seg1	-2.833	-2.557	2.423	-0.018	0.005	0.762	0.762	24381	3.511	2	45.9
2014-01-04	1171318	14, 13	SETSM_WV02_20140418_103001002E622700_1030010030B89500_seg1	-0.736	-1.719	4.298	-0.039	0.012	0.842	0.843	20697	2.980	2	45.9
2014-01-10	1171718	14, 13	SETSM_WV01_20140531_1020010031CE3900_102001002E9AE800_seg4	-3.883	-0.535	2.817	0.000	0.010	0.658	0.658	194193	27.964	2	44.9
			Average	-2.616	-0.943	1.521	-0.022	0.006	0.854	0.855	105180	15.146	1.938	48.0

References

Abdalati, W., Krabill, W., Frederick, E., Manizade, S., Martin, C., Sonntag, J., ... & Koerner, R. (2004). Elevation changes of ice caps in the Canadian Arctic Archipelago. Journal of Geophysical Research: Earth Surface, 109(F4).

Abdullahi, S., Wessel, B., Leichtle, T., Huber, M., Wohlfart, C., & Roth, A. (2018, July). Investigation of Tandem-x Penetration Depth Over the Greenland Ice Sheet. In IGARSS 2018-2018 IEEE International Geoscience and Remote Sensing Symposium (pp. 1336-1339). IEEE.

AMAP, 2017. Snow, Water, Ice and Permafrost in the Arctic (SWIPA) 2017. Arctic Monitoring and Assessment Programme (AMAP), Oslo, Norway. xiv + 269 pp

Bell, C., Mair, D., Burgess, D., Sharp, M., Demuth, M., Cawkwell, F., ... & Wadham, J. (2008). Spatial and temporal variability in the snowpack of a High Arctic ice cap: implications for mass-change measurements. Annals of Glaciology, 48, 159-170.

Benn, D. I., & Evans, D. J. A. (2010). Glaciers and Glaciation. 802 pp. Hodder Education, London.

Benson, C. S. (1962). Stratigraphic studies in the snow and firn of the Greenland ice sheet. U.S. Army cold regions research and engineering laboratory (CRREL) research report no. 70. 120 pp.

Berthier, E., Schiefer, E., Clarke, G. K., Menounos, B., & Rémy, F. (2010). Contribution of Alaskan glaciers to sea-level rise derived from satellite imagery. Nature Geoscience, 3(2), 92.

Bezeau, P., Sharp, M., Burgess, D., & Gascon, G. (2013). Firn profile changes in response to extreme 21st-century melting at Devon Ice Cap, Nunavut, Canada. Journal of Glaciology, 59(217), 981-991.

Bolch, T., Sandberg Sørensen, L., Simonsen, S. B., Mölg, N., Machguth, H., Rastner, P., & Paul, F. (2013). Mass loss of Greenland's glaciers and ice caps 2003–2008 revealed from ICESat laser altimetry data. Geophysical Research Letters, 40(5), 875-881.

Boon, S., Burgess, D. O., Koerner, R. M., & Sharp, M. J. (2010). Forty-seven years of research on the devon island ice cap, arctic canada. Arctic, 13-29.

Box, J. E., Colgan, W. T., Wouters, B., Burgess, D. O., O'Neel, S., Thomson, L. I., & Mernild, S. H. (2018). Global sea-level contribution from Arctic land ice: 1971–2017. Environmental Research Letters, 13(12), 125012.

Brun, F., Berthier, E., Wagnon, P., Kääb, A., & Treichler, D. (2017). A spatially resolved estimate of High Mountain Asia glacier mass balances from 2000 to 2016. Nature geoscience, 10(9), 668.

Burgess, D. O., & Sharp, M. J. (2004). Recent changes in areal extent of the Devon ice cap, Nunavut, Canada. Arctic, Antarctic, and Alpine Research, 36(2), 261-271.

Burgess, D. O., Sharp, M. J., Mair, D. W., Dowdeswell, J. A., & Benham, T. J. (2005). Flow dynamics and iceberg calving rates of Devon Ice Cap, Nunavut, Canada. Journal of Glaciology, 51(173), 219-230.

Burgess, D., & Sharp, M. J. (2008). Recent changes in thickness of the Devon Island ice cap, Canada. Journal of Geophysical Research: Solid Earth, 113(B7).

Burgess, D.O., 2017. Mass balance of ice caps in the Queen Elizabeth Islands, Arctic Canada: 2014 –2015; Geological Survey of Canada, Open File 8223, 38 p.

Campbell Scientific, Inc. (2019) SR50A-Series Sonic Ranging Sensors Product Manual. https://s.campbellsci.com/documents/us/manuals/sr50a-series.pdf

Casey, J. A., & Kelly, R. E. (2010). Estimating the equilibrium line of Devon Ice Cap, Nunavut, from RADARSAT-1 ScanSAR wide imagery. Canadian Journal of Remote Sensing, 36(sup1), S41-S55.

Climate Change, Cambridge, U. K.Thomson, L. I., Zemp, M., Copland, L., Cogley, J. G., & Ecclestone, M. A. (2016). Comparison of geodetic and glaciological mass budgets for White Glacier, Axel Heiberg Island, Canada. Journal of Glaciology, 63(237), 55-66.

Cogley, J. G. (2009). Geodetic and direct mass-balance measurements: comparison and joint analysis. Annals of Glaciology, 50(50), 96-100.

Cogley, J. G., & Adams, W. P. (1998). Mass balance of glaciers other than the ice sheets. Journal of Glaciology, 44(147), 315-325.

Cogley, J. G., Hock, R., Rasmussen, L. A., Arendt, A. A., Bauder, A., Braithwaite, R. J., ... & Zemp, M. (2011). Glossary of glacier mass balance and related terms. IHP-VII technical documents in hydrology, 86, 965.

Colgan, W., & Sharp, M. (2008). Combined oceanic and atmospheric influences on net accumulation on Devon Ice Cap, Nunavut, Canada. Journal of Glaciology, 54(184), 28-40.

Colgan, W., Davis, J., & Sharp, M. (2008). Is the high-elevation region of Devon Ice Cap thickening?. Journal of Glaciology, 54(186), 428-436.

Cook, A. J., Copland, L., Noël, B. P., Stokes, C. R., Bentley, M. J., Sharp, M. J., ... & van den Broeke, M. R. (2019). Atmospheric forcing of rapid marine-terminating glacier retreat in the Canadian Arctic Archipelago. Science advances, 5(3), eaau8507.

Cuffey, K. M., & Paterson, W. S. B. (2010). The physics of glaciers. Academic Press.

Dall, J. (2007). InSAR elevation bias caused by penetration into uniform volumes. I E E E Transactions on Geoscience and Remote Sensing, 45(7), 2319-2324.

Dall, J., Madsen, S. N., Keller, K., & Forsberg, R. (2001). Topography and penetration of the Greenland ice sheet measured with airborne SAR interferometry. Geophysical Research Letters, 28(9), 1703-1706.

De Jong, T. (2013). Recent Changes in Glacier Facies Zonation on Devon Ice Cap, Nunavut, Detected from SAR Imagery and Field Validation Methods (Master's thesis, University of Ottawa, Canada). Retrieved from: https://uottawa-primo.hosted.exlibrisgroup.com/permalink/f/ovsnv/UOTTAWA_IIIb4553351

Dehecq, A., Millan, R., Berthier, E., Gourmelen, N., Trouvé, E., & Vionnet, V. (2016). Elevation changes inferred from TanDEM-X data over the Mont-Blanc area: Impact of the X-band interferometric bias. IEEE Journal of Selected Topics in Applied Earth Observations and Remote Sensing, 9(8), 3870-3882.

Dowdeswell, J. A., Benham, T. J., Gorman, M. R., Burgess, D., & Sharp, M. J. (2004). Form and flow of the Devon Island ice cap, Canadian Arctic. Journal of Geophysical Research: Earth Surface, 109(F2).

Dowdeswell, J. A., Hagen, J. O., Björnsson, H., Glazovsky, A. F., Harrison, W. D., Holmlund, P., ... & Thomas, R. H. (1997). The mass balance of circum-Arctic glaciers and recent climate change. Quaternary research, 48(1), 1-14.

Foresta, L., Gourmelen, N., Pálsson, F., Nienow, P., Björnsson, H., & Shepherd, A. (2016). Surface elevation change and mass balance of Icelandic ice caps derived from swath mode CryoSat- 2 altimetry. Geophysical Research Letters, 43(23).

Foresta, L., Gourmelen, N., Weissgerber, F., Nienow, P., Williams, J. J., Shepherd, A., ... & Plummer, S. (2018). Heterogeneous and rapid ice loss over the Patagonian Ice Fields revealed by CryoSat-2 swath radar altimetry. Remote Sensing of Environment, 211, 441-455.

Fritz, T., Eineder, M. (2013). TerraSAR-X Ground Segment Basic Product Specification Document, Cluster Applied Remote Sensing (CAF), TX-GS-DD-3302, Issue 1.9.

Fritz, T., Rossi, C., Yague-Martinez, N., Rodriguez-Gonzalez, F., Lachaise, M., & Breit, H. (2011, July). Interferometric processing of TanDEM-X data. In 2011 IEEE International Geoscience and Remote Sensing Symposium (pp. 2428-2431). IEEE.

Gardelle, J., Berthier, E., & Arnaud, Y. (2012). Impact of resolution and radar penetration on glacier elevation changes computed from DEM differencing. Journal of Glaciology, 58(208), 419-422.

Gardelle, J., Berthier, E., & Arnaud, Y. (2012a). Impact of resolution and radar penetration on glacier elevation changes computed from DEM differencing. Journal of Glaciology, 58(208), 419-422.

Gardelle, J., Berthier, E., & Arnaud, Y. (2012b). Slight mass gain of Karakoram glaciers in the early twenty-first century. Nature geoscience, 5(5), 322.

Gardner, A. S., & Sharp, M. (2007). Influence of the Arctic circumpolar vortex on the mass balance of Canadian High Arctic glaciers. Journal of Climate, 20(18), 4586-4598.

Gardner, A. S., Moholdt, G., Cogley, J. G., Wouters, B., Arendt, A. A., Wahr, J., ... & Ligtenberg, S. R. (2013). A reconciled estimate of glacier contributions to sea level rise: 2003 to 2009. Science, 340(6134), 852-857.

Garrity C. (1992). Characterization of snow on floating ice and case studies of brightness temperature changes during the onset of melt. In: Carsey FD, ed. Microwave remote sensing of sea ice, Geophysical Monograph Series. Washington (DC): American Geophysical Union, 68, 313–328.

Gascon, G., Sharp, M., Burgess, D., Bezeau, P., & Bush, A. B. (2013). Changes in accumulation- area firn stratigraphy and meltwater flow during a period of climate warming: Devon Ice Cap, Nunavut, Canada. Journal of Geophysical Research: Earth Surface, 118(4), 2380-2391.

Gray, L., Burgess, D., Copland, L., Demuth, M. N., Dunse, T., Langley, K., & Schuler, T. V. (2015). CryoSat-2 delivers monthly and inter-annual surface elevation change for Arctic ice caps. The Cryosphere, 9(5), 1895-1913.

Gray, L., Burgess, D., Copland, L., Dunse, T., Langley, K., & Moholdt, G. (2017). A revised calibration of the interferometric mode of the CryoSat-2 radar altimeter improves ice height and height change measurements in western Greenland. The Cryosphere, 11, 1041-1058.

Groh A and 11 others (2014) Mass, volume and velocity of the Antarctic ice sheet: present-day changes and error effects. Surv.Geophys., 35(6), 1481–1505.

Gruber, A., Wessel, B., Huber, M., & Roth, A. (2012). Operational TanDEM-X DEM calibration and first validation results. ISPRS journal of photogrammetry and remote sensing, 73, 39-49.

Gruber, A., Wessel, B., Martone, M., & Roth, A. (2016). The TanDEM-X DEM mosaicking: Fusion of multiple acquisitions using InSAR quality parameters. IEEE Journal of Selected Topics in Applied Earth Observations and Remote Sensing, 9(3), 1047-1057.

Hall, D. K., Bayr, K. J., Schöner, W., Bindschadler, R. A., & Chien, J. Y. (2003). Consideration of the errors inherent in mapping historical glacier positions in Austria from the ground and space (1893–2001). Remote Sensing of Environment, 86(4), 566-577.

Hall, D. K., Williams, R. S., Barton, J. S., Sigurđsson, O., Smith, L. C., & Garvin, J. B. (2000). Evaluation of remote-sensing techniques to measure decadal-scale changes of Hofsjökull ice cap, Iceland. Journal of Glaciology, 46(154), 375-388.

Hanssen, R. F. (2001). Radar interferometry: data interpretation and error analysis (Vol. 2). Springer Science & Business Media.

Hastings, D. A., & Dunbar, P. (1998). Development & assessment of the global land one-km base elevation digital elevation model (GLOBE). International Society of Photogrammetry and Remote Sensing Archives, 32(4), 218-221.

Hoen, E. W., & Zebker, H. A. (2000). Penetration depths inferred from interferometric volume decorrelation observed over the Greenland ice sheet. IEEE Transactions on Geoscience and Remote Sensing, 38(6), 2571-2583.

Huss, M. (2013). Density assumptions for converting geodetic glacier volume change to mass change. The Cryosphere, 7(3), 877-887.

Huss, M., & Hock, R. (2015). A new model for global glacier change and sea-level rise. Frontiers in Earth Science, 3, 54.

Jaber, W. A., Floricioiu, D., Rott, H., & Eineder, M. (2013). Surface elevation changes of glaciers derived from SRTM and TanDEM-X DEM differences. In 2013 IEEE International Geoscience and Remote Sensing Symposium-IGARSS (pp. 1893-1896). IEEE.

Jezek, K. C., Gogineni, P., & Shanableh, M. (1994). Radar measurements of melt zones on the Greenland ice sheet. Geophysical Research Letters, 21(1), 33-36.

Koerner, R. M. (1966). Accumulation on the Devon Island ice cap, northwest territories, Canada. Journal of Glaciology, 6(45), 383-392.

Koerner, R. M. (1970a). Some observations on superimposition of ice on the Devon Island ice cap, NWT Canada. Geografiska Annaler: Series A, Physical Geography, 52(1), 57-67.

Koerner, R. M. (1970b). The mass balance of the Devon Island ice cap, Northwest Territories, Canada, 1961-66. Journal of Glaciology, 9(57), 325-336.

Koerner, R. M. (1977). Devon Island ice cap: core stratigraphy and paleoclimate. Science, 196(4285), 15-18.

Koerner, R. M. (1997). Some comments on climatic reconstructions from ice cores drilled in areas of high melt. Journal of Glaciology, 43(143), 90-97.

Koerner, R. M. (2005). Mass balance of glaciers in the Queen Elizabeth Islands, Nunavut, Canada. Annals of Glaciology, 42, 417-423.

König, M., Wadham, J., Winther, J. G., Kohler, J., & Nuttall, A. M. (2002). Detection of superimposed ice on the glaciers Kongsvegen and midre Lovénbreen, Svalbard, using SAR satellite imagery. Annals of Glaciology, 34, 335-342.

Koskinen, J., Pulliainen, J., & Hallikainen, M. (2000, July). Effect of snow wetness to C-band backscatter-a modeling approach. In IGARSS 2000. IEEE 2000 International Geoscience and Remote Sensing Symposium. Taking the Pulse of the Planet: The Role of Remote Sensing in Managing the Environment. Proceedings (Cat. No. 00CH37120) (Vol. 4, pp. 1754-1756). IEEE.

Lachaise, M., Fritz, T., & Bamler, R. (2017). The dual-baseline phase unwrapping correction framework for the TanDEM-X mission part 1: Theoretical description and algorithms. IEEE Transactions on Geoscience and Remote Sensing, 56(2), 780-798.

Mair, D., Burgess, D., & Sharp, M. (2005). Thirty- seven year mass balance of Devon Ice Cap, Nunavut, Canada, determined by shallow ice coring and melt modeling. Journal of Geophysical Research: Earth Surface, 110(F1).

Martone, M., Rizzoli, P., & Krieger, G. (2016). Volume decorrelation effects in TanDEM-X interferometric SAR data. IEEE Geoscience and Remote Sensing Letters, 13(12), 1812-1816.

Milillo, P., Rignot, E., Rizzoli, P., Scheuchl, B., Mouginot, J., Bueso-Bello, J., & Prats-Iraola, P. (2019). Heterogeneous retreat and ice melt of Thwaites Glacier, West Antarctica. Science advances, 5(1), eaau3433.

Millan, R., Mouginot, J., & Rignot, E. (2017). Mass budget of the glaciers and ice caps of the Queen Elizabeth Islands, Canada, from 1991 to 2015. Environmental Research Letters, 12(2), 024016.

Moholdt, G., Nuth, C., Hagen, J. O., & Kohler, J. (2010). Recent elevation changes of Svalbard glaciers derived from ICESat laser altimetry. Remote Sensing of Environment, 114(11), 2756-2767.

Moreira, A., Prats-Iraola, P., Younis, M., Krieger, G., Hajnsek, I., & Papathanassiou, K. P. (2013). A tutorial on synthetic aperture radar. IEEE Geoscience and remote sensing magazine, 1(1), 6-43.

Mortimer, C. A., Sharp, M., & Wouters, B. (2016). Glacier surface temperatures in the Canadian High Arctic, 2000–15. Journal of Glaciology, 62(235), 963-975.

Muller, K., Hamran, S. E., Sinisalo, A., & Hagen, J. O. (2011). Phase center of L-band radar in polar snow and ice. IEEE Transactions on Geoscience and Remote Sensing, 49(11), 4572-4579.

Noël, B., van de Berg, W. J., Lhermitte, S., Wouters, B., Schaffer, N., & van den Broeke, M. R. (2018). Six decades of glacial mass loss in the Canadian Arctic Archipelago. Journal of Geophysical Research: Earth Surface, 123(6), 1430-1449.

Nolin, A. W., & Payne, M. C. (2007). Classification of glacier zones in western Greenland using albedo and surface roughness from the Multi-angle Imaging SpectroRadiometer (MISR). Remote Sensing of Environment, 107(1-2), 264-275.

Nuth, C., & Kääb, A. (2011). Co-registration and bias corrections of satellite elevation data sets for quantifying glacier thickness change. The Cryosphere, 5(1), 271-290.

Oliver, C., & Quegan, S. (2004). Understanding synthetic aperture radar images. SciTech Publishing.

Olivier, P., & Vidal-Madjar, D. (1994). Empirical estimation of the ERS-1 SAR radiometric resolution. Remote Sensing, 15(5), 1109-1114.

Pandey, P., Manickam, S., Bhattacharya, A., Ramanathan, Singh, G., & Venkataraman. (2016). Qualitative and quantitative assessment of TanDEM-X DEM over western Himalayan glaciated terrain. Geocarto International, 1–13.

Partington, K. (1998). Discrimination of glacier facies using multi-temporal SAR data. Journal of Glaciology, 44(146), 42-53.

Paterson, W. S. B. (1976). Vertical strain-rate measurements in an Arctic ice cap and deductions from them. Journal of Glaciology, 17(75), 3-12.

Paterson, W. S. B. (1994). The Physics of Glaciers (3rd ed.). Oxford, United Kingdom: Elsevier Science Ltd. 481 pp.

Porter, et al., 2018, "ArcticDEM", Release 7, Version 3. https://doi.org/10.7910/DVN/OHHUKH, Harvard Dataverse.

Pukelsheim, F. (1994). The three sigma rule. The American Statistician, 48(2), 88-91.

Rabus B, Eineder M, Roth A, Bamler R. 2003. The shuttle radar topography mission – a new class of digital elevation models acquired by spaceborne radar ISPRS. J Photogramm Remote Sens. 57:241–262.

Rankl, M., & Braun, M. (2016). Glacier elevation and mass changes over the central Karakoram region estimated from TanDEM-X and SRTM/X-SAR digital elevation models. Annals of Glaciology, 57(71), 273-281.

Rignot, E., Echelmeyer, K., & Krabill, W. (2001). Penetration depth of interferometric synthetic- aperture radar signals in snow and ice. Geophysical Research Letters, 28(18), 3501-3504.

Rizzoli, P., Martone, M., Gonzalez, C., Wecklich, C., Tridon, D. B., Bräutigam, B., ... & Wessel, B. (2017a). Generation and performance assessment of the global TanDEM-X digital elevation model. ISPRS Journal of Photogrammetry and Remote Sensing, 132, 119-139.

Rizzoli, P., Martone, M., Rott, H., & Moreira, A. (2017b). Characterization of snow facies on the Greenland Ice Sheet observed by TanDEM-X interferometric SAR data. Remote Sensing, 9(4), 315.

Rossi, C., Gonzalez, F. R., Fritz, T., Yague-Martinez, N., & Eineder, M. (2012). TanDEM-X calibrated raw DEM generation. ISPRS Journal of Photogrammetry and Remote Sensing, 73, 12-20.

Rott, H., Floricioiu, D., Wuite, J., Scheiblauer, S., Nagler, T., & Kern, M. (2014). Mass changes of outlet glaciers along the Nordensjköld Coast, northern Antarctic Peninsula, based on TanDEM- X satellite measurements. Geophysical Research Letters, 41(22), 8123-8129.

Rutishauser, A., Blankenship, D. D., Sharp, M., Skidmore, M. L., Greenbaum, J. S., Grima, C., ... & Young, D. A. (2018). Discovery of a hypersaline subglacial lake complex beneath Devon Ice Cap, Canadian Arctic. Science advances, 4(4), eaar4353.

Schaffer, N. (2017). Dynamics and Mass Balance of Penny Ice Cap, Baffin Island, Nunavut, In a Changing Climate (Doctoral dissertation, University of Ottawa, Canada). Retrieved from: https://uottawa-primo.hosted.exlibrisgroup.com/permalink/f/ovsnv/UOTTAWA_IIIb6000687

Seehaus, T., Marinsek, S., Helm, V., Skvarca, P., & Braun, M. (2015). Changes in ice dynamics, elevation and mass discharge of Dinsmoor–Bombardier–Edgeworth glacier system, Antarctic Peninsula. Earth and Planetary Science Letters, 427, 125-135.

Sharp, M., Burgess, D. O., Cawkwell, F., Copland, L., Davis, J. A., Dowdeswell, E. K., ... & Williamson, S. N. (2014). Remote sensing of recent glacier changes in the Canadian Arctic. In Global Land Ice Measurements from Space (pp. 205-228). Springer, Berlin, Heidelberg.

Sharp, M., Burgess, D. O., Cogley, J. G., Ecclestone, M., Labine, C., & Wolken, G. J. (2011). Extreme melt on Canada's Arctic ice caps in the 21st century. Geophysical Research Letters, 38(11).

Snehmani, Singh, M. K., Gupta, R. D., Bhardwaj, A., & Joshi, P. K. (2015). Remote sensing of mountain snow using active microwave sensors: a review. Geocarto International, 30(1), 1-27.

Sommerfeld, R. A., & LaChapelle, E. (1970). The classification of snow metamorphism. Journal of Glaciology, 9(55), 3-18.

Stocker, T. F., D. Qin, G.-K. Plattner, M. Tignor, S. K. Allen, J. Boschung, A. Nauels, Y. Xia, V. Bex, and P. M. Midgley (Eds.) (2013), Climate change 2013: The physical science basis. Contribution of working group I to the fifth assessment report, Tech. Rep., Intergovernmental Panel on Climate Change, Cambridge, U. K.

Studinger, M. (2010, updated 2013). IceBridge ATM L1B Qfit Elevation and Return Strength, Version 1. Boulder, Colorado USA. NASA National Snow and Ice Data Center Distributed Active Archive Center.

Studinger, M. (2013, updated 2018). IceBridge ATM L1B Elevation and Return Strength, Version 2. Boulder, Colorado USA. NASA National Snow and Ice Data Center Distributed Active Archive Center.

Studinger, M. 2014, updated 2018. IceBridge ATM L2 Icessn Elevation, Slope, and Roughness, Version 2. Boulder, Colorado USA. NASA National Snow and Ice Data Center Distributed Active Archive Center.

Sylvestre, T., Copland, L., Demuth, M. N., & Sharp, M. (2013). Spatial patterns of snow accumulation across Belcher Glacier, Devon Ice Cap, Nunavut, Canada. Journal of Glaciology, 59(217), 874-882.

Thomson, L. I., Zemp, M., Copland, L., Cogley, J. G., & Ecclestone, M. A. (2016). Comparison of geodetic and glaciological mass budgets for White Glacier, Axel Heiberg Island, Canada. Journal of Glaciology, 63(237), 55-66.

Tsai, Y. L. S., Dietz, A., Oppelt, N., & Kuenzer, C. (2019). Remote Sensing of Snow Cover Using Spaceborne SAR: A Review. Remote Sensing, 11(12), 1456.

Van Wychen, W., Burgess, D. O., Gray, L., Copland, L., Sharp, M., Dowdeswell, J. A., & Benham, T. J. (2014). Glacier velocities and dynamic ice discharge from the Queen Elizabeth Islands, Nunavut, Canada. Geophysical Research Letters, 41(2), 484-490.

Van Wychen, W., Copland, L., Gray, L., Burgess, D., Danielson, B., & Sharp, M. (2012). Spatial and temporal variation of ice motion and ice flux from Devon Ice Cap, Nunavut, Canada. Journal of Glaciology, 58(210), 657-664.

Van Wychen, W., Davis, J., Copland, L., Burgess, D. O., Gray, L., Sharp, M., ... & Benham, T. J. (2017). Variability in ice motion and

dynamic discharge from Devon Ice Cap, Nunavut, Canada. Journal of Glaciology, 63(239), 436-449.

Wang, L., Sharp, M. J., Rivard, B., Marshall, S., & Burgess, D. (2005). Melt season duration on Canadian Arctic ice caps, 2000–2004. Geophysical Research Letters, 32(19).

Wessel, B. (2016) TanDEM-X Ground Segment DEM Products Specification Document, Earth Observation Center (EOC), TD-GS-PS-0021, Issue 3.1.

Wessel, B., Bertram, A., Gruber, A., Bemm, S., & Dech, S. (2016). A New High-Resolution Elevation Model of Greenland Derived From Tandem-X. ISPRS Annals of Photogrammetry, Remote Sensing & Spatial Information Sciences, 3(7).

Wessel, B., Huber, M., Wohlfart, C., Marschalk, U., Kosmann, D., & Roth, A. (2018). Accuracy assessment of the global TanDEM-X Digital Elevation Model with GPS data. ISPRS Journal of Photogrammetry and Remote Sensing, 139, 171-182.

White, A., & Copland, L. (2015). Decadal-scale variations in glacier area changes across the Southern Patagonian Icefield since the 1970s. Arctic, antarctic, and alpine research, 47(1), 147-167.

Wolken, G. J., Sharp, M., & Wang, L. (2009). Snow and ice facies variability and ice layer formation on Canadian Arctic ice caps, 1999–2005. Journal of Geophysical Research: Earth Surface, 114(F3).

Wouters, B., Bamber, J. Á., Van den Broeke, M. R., Lenaerts, J. T. M., & Sasgen, I. (2013). Limits in detecting acceleration of ice sheet mass loss due to climate variability. Nature Geoscience, 6(8), 613.

Young, D. A., Kempf, S. D., Blankenship, D. D., Holt, J. W., & Morse, D. L. (2008). New airborne laser altimetry over the Thwaites Glacier catchment, West Antarctica. Geochemistry, Geophysics, Geosystems, 9(6).

Zemp, M., Thibert, E., Huss, M., Stumm, D., Denby, C. R., Nuth, C., ... & Joerg, P. C. (2013). Reanalysing glacier mass balance measurement series. The Cryosphere, 7(4), p-1227.

Zhao, J., & Floricioiu, D. (2017). The penetration effects on TanDEM-X elevation using the GNSS and laser altimetry measurements in Antarctica. The International Archives of Photogrammetry, Remote Sensing and Spatial Information Sciences, 42, 1593.